An energized mass approach for drag evaluation

Development and testing of a drag evaluation method for bodies moving with constant velocity

Laura Jou Ferrer

MSc Thesis

TU Delft Delft University of Technology

Department of Aerodynamics

An energized mass approach for drag evaluation

Development and testing of a drag evaluation method for bodies moving with constant velocity

by

Laura Jou Ferrer

to obtain the degree of Master of Science
at the Delft University of Technology,
to be defended publicly on Wednesday June 22, 2022 at 10:00 AM.

Student number:	4456734	
Project duration:	November 15, 2020 – June 22, 2022	
Thesis committee:	Prof. F. Scarano,	TU Delft, Chair
	Dr. A. Sciacchitano,	TU Delft, Supervisor
	Dr. N. Timmer,	TU Delft, examiner
	Dr. W. Terra,	NOC*NSF Aerodynamics, examiner

TU Delft

Preface

This thesis is written with the aim to obtain the degree of Master of Science in the field of Aerodynamics at the TU Delft. It contains a review of all the work done during my thesis project and it represents the end of my studies in Delft.

I would like to thank my supervisor Dr. Sciacchitano for his support and guidance. This research project has given me a unique opportunity to learn and carry out an experimental campaign in a world-class skating rink. I am very grateful to Dr. Terra and the team at Thialf for letting me take part in this campaign. I would also like to thank the athletes that participated and their teams. Additionally, I would like to thank the staff at the HSL that helped prepare for the experiments. I am also grateful to Dr. Spoelstra and Dr. Rival for their guidance during the first part of the thesis.

The other data in this work comes from the work of Dr. Terra and Dr. Spoelstra, to who I am thankful for letting me use it and answering my doubts about it. Furthermore, I am grateful Dr. Galler from Queen's university for his clarifying explanation about the energized mass concept, and Dr. El Makdah for his help in the discussion of a possible experimental campaign.

Finally, I would like to thank my mother and my sister for their love and support during the duration of the thesis and of my studies in general. I am also grateful to my friends in Spain, the Netherlands, Switzerland and everywhere else, especially those that were doing the thesis at the same time as me. Lastly, I would like to thank Lorenzo for being by my side and cheering me on throughout the whole process.

Laura Jou Ferrer
May 2022

Executive Summary

In speed sports, the result of a competition might be decided by a very small time difference between two athletes. Therefore, reducing the drag coefficient is a priority. It is usually measured using simulations or wind tunnel tests, but in the case of athletes this might mean that a model has to be used and the race conditions approximated. On-site measurements are preferred because they provide flow descriptions that are representative of actual race conditions.

This work introduces a new method to calculate the drag of a transiting object that moves with a constant velocity. The method is based on the concept of the energized mass and its only input is raw images similar to those used in PIV. Since the images can be planar, only one camera is needed, and no velocity fields need to be computed.

The energized mass, introduced by Galler et al. [1], refers to a measure of the normalized kinetic energy of all the fluid that is affected by the movement of the body. The idea behind the method is that the mechanism by which kinetic energy is transferred into this fluid is the work done by the drag force, and so an energy balance can yield the drag coefficient. In this way, the development of the wake area in time can be used to estimate the drag coefficient. An important assumption here is that the body is bluff and not streamlined.

The method is tested on five different experimental cases, pertaining to three different models. Some of the data is obtained from previous experimental campaigns. This includes tomo-PIV images of a sphere, which were captured by Terra et al. [2] [3] when demonstrating the Ring of Fire concept. Spoeltra et al. [4] measured the flow around a cyclist in upright and timetrial position using stereo-PIV. The campaign was done on-site with a real cyclist, and the method is also tested on this data. Finally, an experimental campaign was carried out in the ice skating rink of Thialf (Heerenveen, the Netherlands) and part of the experiments were done for the purpose of this thesis. Using a stereo-PIV set up, measurements were done on the flow around a skater in two different positions. The first one was similar to the normal position of a skater in a competition, but in this case both arms were attached to the body with the hands held together at the back. The second one was not a position that would be seen at a speed skating race, with the knees slightly more extended and both arms stretched to the sides. In both cases, the skater glided through the measurement domain.

For all five experimental cases, the wake was first studied by examining the PIV velocity fields. The velocity fields, vorticity and time development of the wake gave information as to what the expected wake are would be and what shape it would have. The method was applied on all cases, and the obtained drag results were compared to those resulting from the Ring of Fire methodology, which is based on the momentum balance equation [5]. In the cases where literature was available, the drag was also compared to reported results.

In general, the method was found to significantly overestimate the drag of all objects. The most extreme case was the one of the sphere, where the energized mass method predicted a drag coefficient three times larger than the Ring of Fire methodology. However, the method was capable of correctly measuring which objects had higher drag coefficients than others. A possible explanation for this discrepancies the overestimation of the wake area by the method.

Table of Contents

List of Figures

List of Tables

Chapter 1

Introduction

The drag coefficient is one of the most important parameters to describe the interaction of a body with its surrounding flow. Usually it needs to be measured experimentally and tabulated. This process is not always straightforward, as measuring balances can be sources of noise and error and might affect the flow. PIV has been used as an alternative tool to calculate the drag, using momentum balance methods for steady and unsteady airfoils [6, 7], or unsteady square-cross section cylinders [8].

In speed sports the drag coefficient is of special importance. For example, in cycling the drag has been measured to be responsible for more than 90% of the total resistance [9]. In this sports, a small reduction in the drag coefficient can be a significant improvement in the performance. For example, in the Tokio 2020 Olympics several gold medals were decided by a margin of fractions of a second [10].

In speed skating the difference between the winner and the runner-up is small. Some examples of this can be found in the results of the International Skating Union (ISU) World Championships held in Thialf, Herenveeren in February 2021. In the 500 m race, the time difference that awarded Laurent Dubreuil the vitory was of only 0.15 s [11]. In the popular 10 000 m event, the Swede Nils van der Poel accumulated a time advantage of only 12.91 s over a total race time of slightly over 12.5 min [12].

With the victory margin being small in sports like cycling and skating, drag reduction can pose an advantage for the athletes. In cycling, the position of the rider has been identified as the biggest factor in aerodynamic performance. However, the UCI (Union Cycliste Internationale) has restrictions on the positioning of the cyclist [13]. This creates a motivation for the development of highly technical equipment, such as the SWIFTskin program to develop a speed skating suit [14] [15] and a cycling suit [16]. Other efforts to improve aerodynamic performance include experimental analysis of cycling helmets [17] [18] [19]. However, in order to assess the success of the drag reduction, it is important to know the drag coefficient of the original and the modified suit with accuracy. This testing is usually done in wind tunnel experiments, which means the conditions cannot be exactly the same as in the races.

Recently, the Ring of Fire method has been introduced, which uses the momentum balance equations formulated by Rival and van Oudheusden [5] and the velocity fields up and downstream of the wake to measure the drag. This method has been proven successful with a sphere and a cyclist [3] [4]. These experiments demonstrated the feasibility to measure the drag on-site (as opposed to inside a wind tunnel using models) and in large control volumes. However, this relies on velocity fields, which inevitably adds a compounding error in the obtained drag coefficient values [20]. In addition, the streamwise velocity component is required for the momentum balance. Planar PIV can only yield the in-plane velocities, so more experimental set ups with multiple cameras need to be used, such as stereo-PIV or tomo-PIV. This adds complexity to the experimental campaign itself but also to the posterior data processing.

These issues highlight the usefulness of a new method that would require a planar PIV set up and no velocity fields at all. The idea behind it stems from the energized mass, which was introduced by Galler and Rival [1]. This new concept draws inspiration from the added mass, which in potential flow refers to the added inertia that a body has to overcome to accelerate in a fluid of finite density, as compared to vacuum. The energized mass, instead, is a real flow concept, and the focus on this work is its application to objects translating at constant velocities.

When a body moves through a fluid with constant velocity, the fluid surrounding it, initially at rest, will undergo a change in velocity. The energized mass is a measure of the change in normalized kinetic energy of the fluid.

This research project aims at developing a method for measuring the drag of an object undergoing a steady, translational motion. The main requirement for this new method is that it shall not rely on velocity fields of the wake of the object. Using the energized mass concept, it is possible to reach a formulation that relies on the wake area, and not on the values of the velocities. As a consequence, the wake area has to be obtained using only the planar PIV images.

One of the key steps of this project will be necessary to identify the wake of the body. While there is some literature, as pointed out in chapter 2, that has attempted to do so in different ways, there is no clear consensus on what the optimal method would be. In addition, these documented processes usually require detailed information about the velocity and/or vorticity fields downstream of the object. Since none of these are available, this work will answer the question of whether it is possible at all to identify the wake using only raw images of the flow behind an object.

This thesis is structured as follows. The literature study is presented in chapter 2. It includes all review of all relevant literature in different topics that are related to the development of the energized mass method. The first section is about Particle Image Velocimetry, which is useful not only to understand the motivation behind this work, but also to explain how the test datasets were obtained. The second section is about the added mass concept, and is followed by a discussion of the energized mass concept. Finally, the fourth section is focused on the identification of the wake using different methods. chapter 4 is where the energized mass method is presented. It includes a detailed explanation of all the steps and their justification, in addition to a sensitivity study of the main parameters that are used throughout the processing of the images. The description of the experimental set up for each case is presented in chapter 3 together with the selected processing parameters in each case. The results are shown in chapter 5. In this chapter, one section is dedicated to each experimental case. In each of them, first the wake topology is discussed using PIV velocity fields, and then the energized mass method results are presented. The chapter concludes with a discussion of the obtained results. Finally, the conclusions which have been reached regarding the energized mass method and recommendations for future work are included in chapter 6.

Chapter 2

Literature Study

This chapter contains all the background information that is relevant to the energized mass approach developed in this thesis. Firstly, Particle Image Velocimetry (PIV) is explained in section 2.1. It is included because all the data on which the method is tested was obtained using a PIV experimental set up, and PIV velocity fields are used to compare and evaluate the results. In addition, the limitations in this technique are important to understand the motivation behind the energized mass approach.

The second section of this chapter is focused on the added mass. Its potential flow derivation and real flow applications are explained in subsection 2.2.1 and subsection 2.2.2, respectively. This is followed by a discussion on the drift volume and the force formulations for the added mass. While the added mass is a potential flow concept, it serves as inspiration for the energized mass concept, which is the backbone of this work and is explained in detail in section 2.3.

The chapter concludes with a section dedicated to wake identification methods that have been presented in literature, summarized in section 2.4. The correct measurement of the area of the wake is an essential step to the method developed in this work. Even though the approach is new, it is useful to investigate other methods based on velocity, vorticity thresholding (subsection 2.4.1 and subsection 2.4.2, respectively). The most similar type of wake identification techniques is the image based one, which is explained in subsection 2.4.3.

2.1 Particle Image Velocimetry

Particle Image Velocimetry (PIV) is a flow measurement technique that makes it possible to determine the flow velocities in a region seeded by tracer particles, based on the distance covered by these particles in the span of time between two images. Some of the main advantages that this method offers include the fact that it is not intrusive, as only tracer particles are introduced in the flow, and that it makes it possible to capture the velocity field in an entire area (or volume) of the flow.

It was developed in the last decades of the 20th century, some early research on it includes the work of Adrian [21], and Willert and Gharib [22]. Thanks to the advances in the field, and the developments in digital photography that took place in the last decades, PIV quickly gained popularity and is currently one of the most used flow measurement techniques.

The rest of this section is structured as follows. In subsection 2.1.1, the basics of PIV are explained, followed by sections centered on the equipment and data processing. Next, subsection 2.1.4 is focused on the techniques of stereoscopic PIV and tomographic PIV. The momentum balance method, which is the most commonly used way to evaluate the drag coefficient from PIV data, is explained in subsection 2.1.5. Finally, in subsection 2.1.6 the major sources of error that can affect drag measurements are discussed.

2.1.1 PIV basic principles

The basic principle behind PIV is the ability to measure the distance traveled by tracer particles in a known time interval. A typical planar, 2D PIV experimental set up is shown in Figure 2.1. The necessary equipment usually consists of at least one camera, a laser with the corresponding lenses to shape the laser sheet and tracer particles.

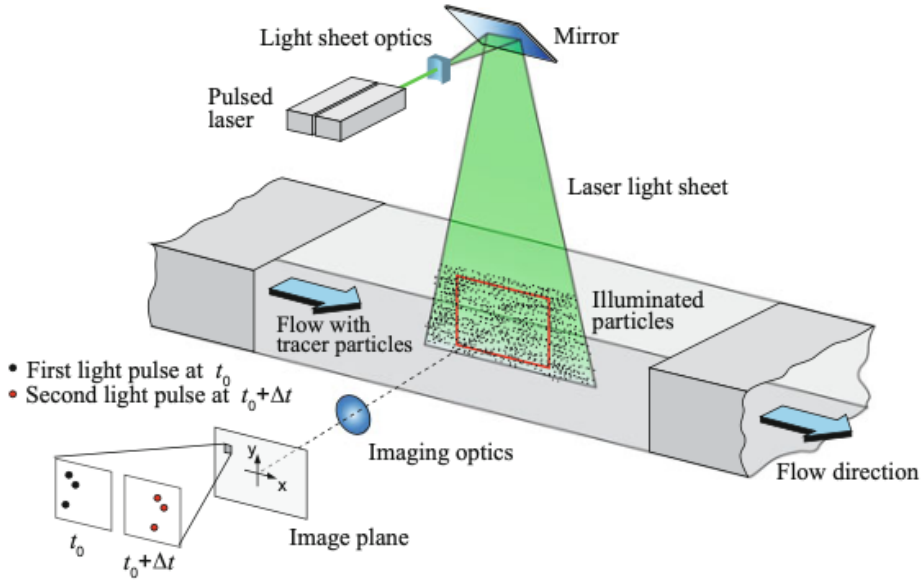

Figure 2.1: Typical experimental set up for PIV, from [23].

The flow is seeded with tracer particles, which are neutrally buoyant so that they follow the flow accurately. They are illuminated with a light source, which is usually a laser, and photographed with cameras at high frequency. For each pair of images, it is possible to identify the particle pairs using cross-correlation, and thus measure the displacement of each particle in the time elapsed between the two pictures. The velocity field for the entire region that is seeded and illuminated can then be obtained. The components mentioned here are explained in more detail in the following subsection, followed by an explanation of the data processing that leads to the final velocity vector fields.

2.1.2 Equipment

As shown in Figure 2.1, the most important components of a PIV set up are the light source, tracer particles and the cameras. The most important characteristics of each are detailed below.

Seeding

PIV is an indirect flow measurement technique, which means that it is the velocity of the seeding that is measured, and not the one of the flow. The seeding is done by introducing tracer particles into the flow field, such that it becomes visible. It is essential to choose adequate tracer particles that have the correct mechanical and optical properties. A compromise needs to be made, since for the former smaller particles are preferred, but larger particles have better light scattering properties [24].

Mehcanical properties In regards to the mechanical properties, the particles should follow the flow accurately, so that the measured particle velocity is identical to the real flow velocity. The particles should also not interact with each other, and not alter the flow [25].

For the case of small spherical particles with a small relative velocity (with respect to the flow), the most important effect is the Stokes drag [26]. Their slip velocity, which is the velocity relative to the flow velocity, is given by the following equation:

$$U_s = U_p - U_f = -\frac{d_p^2(\rho_p - \rho_f)}{18\mu}\frac{\mathrm{d}U_p}{\mathrm{d}t} \tag{2.1}$$

where ρ is the density, d_p the particle diameter U the velocity, and the subscripts p and f represent particle and fluid characteristics, respectively. A particle should have a small slip velocity in order to follow the flow well and have acceptable mechanical properties. Equation 2.1 leads to the conclusion that small diameter and a density close to the fluid density are the most important characteristics of the tracer particles. This is shown in Figure 2.2, where a difference in velocity of $1\,\mathrm{m\,s^{-1}}$ is followed significantly slower when the particle diameter is doubled.

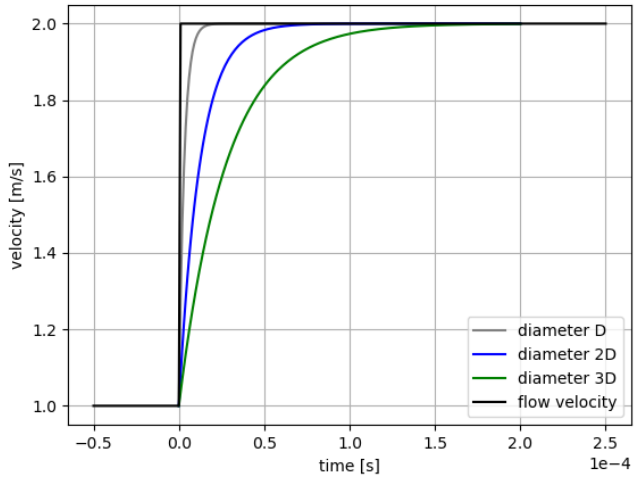

Figure 2.2: Velocity adaptation to the flow of particles of different diameters. The reference particle diameter $D = 1\,\mu\mathrm{m}$ and the particle density $\rho_p = 1 \times 10^3\,\mathrm{kg\,m^{-3}}$, are chosen to emulate the behavior of glycol-water solution particles in air [24].

The available choice of particles is limited by the fluid where the experiments are performed. In air, the density ratio can be as high as $\frac{\rho_p}{\rho_f} = \mathcal{O}(10^3)$ depending on the material used for the tracer particles [24]. In these cases, the particle diameter usually has to be near $1\,\mu\mathrm{m}$ [26].

Optical properties Given that PIV depends on the detection and matching of particles in two images, it is important that the particle images are clearly distinguishable from the background. As typically PIV is done with spherical particles of diameter slightly larger than the wavelength of the light, Mie's scattering law needs to be considered. The scattering is not uniform in all directions: it is strongest in forward direction, lower in backward direction and is lowest in direction normal to the plane of illumination, which is the direction captured by the PIV cameras. This is shown in Figure 2.3. For this reason, PIV needs strong light sources [24].

In general, light scattering is dependant on the particle diameter, the wavelength of the light and the ratio of refractive indices. The most important of these is the particle diameter, as the scattering is proportional to d_p^2 [23].

Some common substances to generate particles suitable for experiments in air are oil or DEHS (di-ethyl-hexyl-sebacate) [23]. However, helium filled soap bubbles (HSFB) have become increasingly popular in PIV experiments on air. They consist of bubbles made of bubble fluid

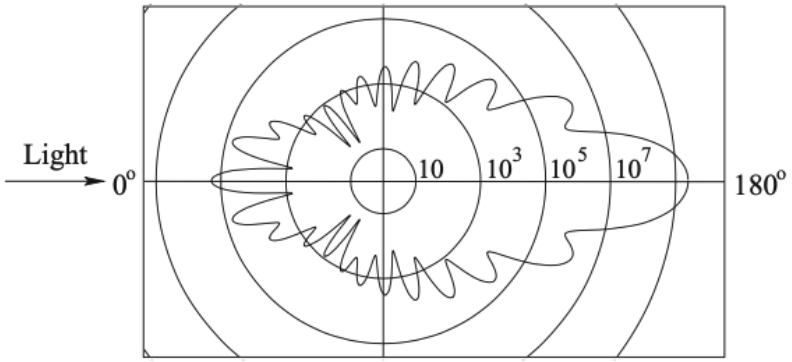

Figure 2.3: Light scattering behavior of an oil particle ($d_p = 1\,\mu m$) in air, from [23].

solution (BFS) and are filled with helium in order to remain neutrally buoyant [27]. They are obtained with bubble generators that can produce up to 50 000 bubbles per second [28], and their main advantages are that they are neutrally buoyant and they have the ability to scatter light efficiently [29]. Recent work has shown a response time of 10 µs [30], and their suitability for large scale PIV experiments [3] [2] [4] [31].

In addition to the mentioned optical and mechanical characteristics that are important in the choice of particles, there are other considerations to keep in mind, mainly related to safety. It is preferable to use particles that are not toxic, corrosive or abrasive, and it is convenient to use particles that will be easy to remove from the experimental set up.

Illumination

Illumination of the tracer particles is usually done with a laser, due to its many advantages. Firstly, the light strength they provide can be very high. In addition, the light is collimated (the light rays are parallel to each other), so it can be easily shaped into a thin sheet, which is necessary for the measurements. The fact that it is pulsed allows a laser to provide light for a short amount of time, such that the particles in the images appear as dots and not as streaks [24]. Finally, they are monochromatic light sources, so there is only one wavelength.

Some commonly used lasers for PIV applications include Nd:YAG (Neodim: yttrium aluminum garnet, $\lambda = 532\,nm$ for green light) and Nd:YLF (Neodim: yttrium lithium fluoride, $\lambda = 526\,nm$ for green light), which are both solid-state lasers. The first type is suitable to any kind of flow speed due to its short pulse duration (5 - 15 ns) [24] and versatility [21], while the second allows for a higher repetition rate, so it is more adequate for time-resolved measurements [23]. The size and thickness of the laser sheet can be adjusted using the correct configuration of lenses.

Imaging

The images of the particles are usually with CCD (charged couple device) or CMOS (complementary metal oxide semiconductor) sensors. With the development of CMOS cameras, nowadays they are preferred for high speed applications, as their read-out rates are higher and thus are capable to store image data faster than CCD sensors and with low noise levels [23].

Another important choice for the imaging is the lens selection. One of the main parameters to consider is the magnification factor M, which represents the ratio between the image distance d_i and the object distance d_o. Another way to understand it is as the ratio between the image size (pixels size times resolution) and the field of view, so that to know the real size of an object,

its image size is multiplied by M. These quantities are related to the focal length of the lens by the thin lens equation:

$$\frac{1}{f} = \frac{1}{d_i} + \frac{1}{d_o} \tag{2.2}$$

The image of the particle diameter d_τ would then be expected to have a size of Md_p, but there are some effects that modify it. Firstly, diffraction will make the particle look bigger. When capturing a small source of light at a distance, the light is spread and forms an Airy disk around the particle image. The diameter of this Airy disk is:

$$d_{diff} = 2.44\lambda(1 + M)f_\# \tag{2.3}$$

Where λ is the laser light wavelength and $f_\#$ is the aperture number or f-stop, which indicates the ratio between the focal length and aperture of the camera. In general, a higher $f_\#$ leads to a more closed aperture, lower light and a higher depth of field (more distant objects in the background appear in focus). The image particle diameter can be estimated as follows [32]:

$$d_\tau = \sqrt{d_{diff}^2 + (Md_p)^2} \tag{2.4}$$

It is possible in most cases to approximate the particle diameter as the diffraction diameter, neglecting Md_p [24]. These equations only hold if the particle image is in focus, and for that the focal depth δ_z needs to be larger than the laser sheet thickness. The laser sheet of course needs to be placed in the focus plane.

$$\delta_z = 4.88\left(1 + \frac{1}{M}\right)^2 f_\#^2\lambda \tag{2.5}$$

Ensuring that the particle image diameter is small and in focus can help reduce uncertainties in the velocity measurements, and increase the image intensity [23]. However, the d_τ should be big enough to avoid peak locking. This phenomena occurs when the particle image diameter is smaller than a pixel, so it is not possible to accurately measure its displacement [24]. The optimal d_τ depends on the PIV type, but ranges from 2 to 6 pixel [23].

2.1.3 Data processing

Once the image pairs are obtained, the velocity fields can be computed by measuring the distance traveled by the particles in the known interval of time. This process takes several steps.

Firstly, before the measurements are done, it is necessary to take reference measurements and calibrate the set up. That way, it is known how much distance a pixel corresponds to, and the velocity can be computed in meters per second. Next, it is common to do some pre-processing of the images in order to reduce background intensity and enhance the particle images. The optimal pre-processing is dependant on the set up and configuration of the experiment.

The calculation of the velocity field starts with dividing the images into interrogation windows. As a rule of thumb, the in-plane displacement on a window should not be larger than 1/4 of the window size and the out-of-plane displacement should be no more than 1/4 of the laser sheet thickness. Finally, it should be small enough that all particles move in a similar in-plane direction: the variation in displacement should be less than a particle diameter. If these three rules are observed, the error in matching particles and calculating the displacement of a window should be less than 5% [24].

The velocity vector in each window is calculated by first obtaining the cross-correlation map for the window. For images that have a good signal to noise ratio, there is a clearly distinguishable

peak. Finding this peak is the next step: its coordinates indicate the average displacement of the particles in the window. Knowing the time interval between the two images, the velocity in pixel/s can be obtained, and it can be translated into $\mathrm{m\,s^{-1}}$. Repeating this in each window yields the complete velocity field.

2.1.4 Stereo-PIV and Tomo-PIV

Thanks to the interest the PIV technique has generated, its evolution has allowed for modifications of the experimental set up presented in Figure 2.1 which make it possible to increase the dimensions of the vector fields, or to capture 3 velocity components.

Stereoscopic PIV

Using stereo-PIV it is possible to capture three velocity components of the vector field in a 2D plane. Moreover, the in-plane velocities can be corrected: when using planar PIV, the velocity fields capture the in-plane velocity projections, which are not necessarily the same as the velocities.

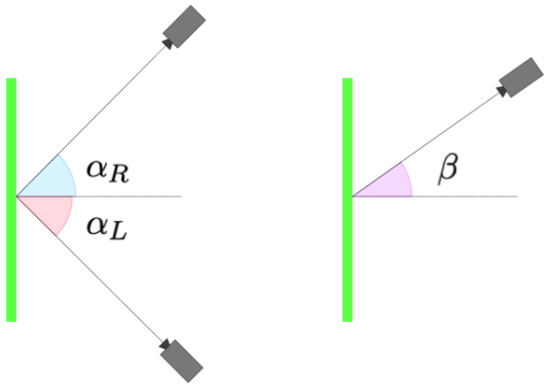

Figure 2.4: Stereo PIV set up angles, as seen from the top (left) and side (right).

The set up is very similar to the planar PIV one, the only required changes include adding an extra camera and slightly modifying the software for data processing [33]. In a stereoscopic PIV set up using the angular method, the cameras are placed at a horizontal angle α with respect to the normal to the laser sheet. A typical set up of this kind is depicted in Figure 2.4. Here, β is the vertical angle between the cameras and the floor, and α is perpendicular to it, the angle between the normal of the plane and the camera line of sight.

Using the combined information of both cameras, it is possible to obtain the out-of-plane velocity component. From each camera (left L and right R), a set of planar velocities will be obtained (U_L, V_L, U_R and V_R). They can be combined as follows to obtain the three velocity components [23]:

$$u = \frac{U_L \tan(\alpha_L) + U_R \tan(\alpha_R)}{\tan(\alpha_L) + \tan(\alpha_R)} \tag{2.6}$$

$$v = \frac{V_L \tan(\beta_L) + V_R \tan(\beta_R)}{\tan(\beta_L) + \tan(\beta_R)} \tag{2.7}$$

$$w = \frac{U_L - U_R}{\tan(\alpha_L) + \tan(\alpha_R)} = \frac{V_L - V_R}{\tan(\beta_L) + \tan(\beta_R)} \tag{2.8}$$

Tomographic PIV

Another development in this field is tomographic PIV. Introduced by Elsinga et al. [34], this method uses several cameras to obtain the the velocity vectors on a 3D domain. The size of the domain is limited by the fact that the depth of the domain has to be smaller than the width and height, typically by a factor of 4. In addition, since the domain is wider the light source needs to be stronger than for other PIV applications [23].

The number of cameras used usually ranges from 3 to 6 and there are a few possible configurations, as long as no two cameras are collinear. The most popular configuration is the pyramid one, but they can also be placed forming a cross or even in a linear configuration. The positioning of the cameras should also be such that the maximum solid angle within them is between 40° and 80°. This angle is one of the most relevant parameters regarding the imaging, together with the camera sensitivity, M and the sensor pixel size. Another important consideration when designing a tomo PIV experiment is the concentration of the tracer particles. For a set up consisting of 4 cameras, the concentration should not exceed 0.5 ppp to avoid compromising the accuracy of the results [35].

The data is processed by using a MART (Multiplicative Algebraic Reconstruction Technique) algorithm or similar algorithm for tomographic reconstruction. Instead of 2D windows, tomo-PIV divides the domain into 3 dimensional windows made up of voxels. 3D cross-correlation is then applied, yielding the velocity fields. A problem that can arise from the tomographic reconstruction is the appearance of ghost particles, which add error to the output velocity fields. This can be mitigated using MTE-MART (motion tracking enhancement MART) or SMTE-MART (sequential MTE-MART) algorithms [23] [34].

Tomo-PIV has been used to investigate vortex rings [36], the physics of drops [37], the flow around a low aspect ratio cylinder [38], turbulent boundary layers [39], or the wake of sphere [3], amongst others.

2.1.5 Drag calculation from PIV data

Developing an approach that can obtain the force using the velocity fields obtained from PIV has been a subject of interest due to the popularity of this flow measurement technique. Such a method would be non-intrusive, and would combine the knowledge of the aerodynamic forces with all the information that can be derived from the velocity fields, giving more insight on the flow.

The classical formulation for the forces in an inertial control volume is given by [40]:

$$\boldsymbol{F}(t) = -\rho \iiint_{CV} \frac{\partial \boldsymbol{u}}{\partial t} \mathrm{d}V - \rho \iint_{CS} \boldsymbol{u}(\boldsymbol{u}\cdot\boldsymbol{n})\mathrm{d}S - \iint_{CS} p\boldsymbol{n}\mathrm{d}S + \iint_{CS} (\tau\cdot\boldsymbol{n})\mathrm{d}S \tag{2.9}$$

where $\boldsymbol{u}$ is the velocity vector, $\boldsymbol{n}$ is the vector normal to the surface, p is the pressure and τ is the viscous stress. The terms on the right hand side can be interpreted as follows: the first one is the unsteady term, the second one is the momentum term, the third is the pressure term and finally the last one is the viscous term.

It is not convenient to have the unsteady term expressed over a volume integral, since PIV is usually performed on a surface. In the case that the flow is incompressible and the body is thin (if the body is bluff an additional term needs to be added), this term can be expanded [41]

$$\boldsymbol{F}(t) = -\rho \frac{\partial}{\partial t} \iint_{CS} \boldsymbol{x}(\boldsymbol{u}\cdot\boldsymbol{n})\mathrm{d}S - \rho \iint_{CS} \boldsymbol{u}(\boldsymbol{u}\cdot\boldsymbol{n})\mathrm{d}S - \iint_{CS} p\boldsymbol{n}\mathrm{d}S + \iint_{CS} (\tau\cdot\boldsymbol{n})\mathrm{d}S \tag{2.10}$$

Where $\boldsymbol{x}$ is the coordinate vector. The unsteady term is zero if the upstream flow is steady [2], and the viscous term can be neglected if the control surfaces are far away enough from the body [8]. In addition, two control surfaces have to be defined: surface S_1 upstream of the body and a surface S_2 in the wake. Conservation of mass has to be satisfied between the two control surfaces in order to apply this approach. This is reference frame is depicted in Figure 2.5. With this simplifications, the instantaneous drag can be expressed as [4]:

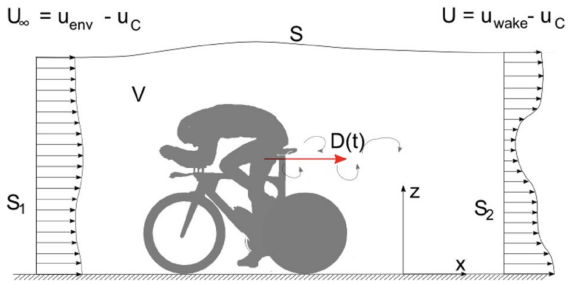

Figure 2.5: Schematic depiction of the reference frame and control surfaces for the case of a cyclist, from [4].

$$F_D(t) = \iint_{S_1} (u_{env} - U)^2 \mathrm{d}S + \iint_{S_1} (p_\infty - p_1)\mathrm{d}S - \iint_{S_2} (u_{wake} - U)^2 \mathrm{d}S - \iint_{S_2} (p_\infty - p_2)\mathrm{d}S \quad (2.11)$$

Where U is the velocity of the body, and u_{env} is the undisturbed velocity field, before the object passes through. In the ideal case u_{env} would be close to zero, but in practice depending on the measurement set up it might be affected by the wind or other environmental conditions, and needs to be taken into account. The pressure term can be challenging to obtain. In some cases, if the flow is measured downstream enough, it can be neglected [4]. Otherwise, the pressure gradient can be obtained directly from the momentum equation [8]:

$$\frac{\mathrm{D}\boldsymbol{u}}{\mathrm{D}t} = -\frac{1}{\rho}\nabla p + \nu\nabla^2\boldsymbol{u} \quad (2.12)$$

The process of integrating to obtain the pressure field can lead to compounding errors. In the case that the flow is incompressible, it can be obtained from a Poisson equation [42]:

$$\nabla^2 p = -\rho\nabla\cdot(\boldsymbol{u}\cdot\nabla)\boldsymbol{u} \quad (2.13)$$

If this approach is used, the correct Neumann boundary conditions need to be selected for the surface at the body [43], and a Dirichlet condition can be established for the outside flow [44].

2.1.6 Uncertainty in PIV-based drag measurements

Even though the Ring of Fire concept has been shown to be a useful tool to measure drag of large objects and on-site, there are some limitations in the measurements.

In general, all PIV velocity measurements are subjected to several error sources. Some of them have been mentioned in the previous sections, as they can be mitigated by a correct selection of equipment. Examples of this include errors due to misalignment of the measurement plane, delayed tracer particle response, incorrect calibration, or peak locking [45].

Several a-priori and a-posteriori techniques have been developed to quantify the uncertainty of PIV measurements. Of particular interest for this work is the uncertainty on stereo-PIV

data, as it provides the out of plane component which is used for the momentum balance drag calculation. It has been shown that this streamwise component is subject to greater uncertainty [45]. A symmetric disposition of the cameras, with an angle of $45° - 60°$ has been observed to reduce the uncertainty [46].

The processing parameters used to obtain the velocity fields from PIV data can also introduce error in the drag measurements. The interrogation window size, in particular, is usually a trade-off between increasing the resolution and reducing the noise [47]. The window size needs to be small enough to provide reasonable resolution of the velocity field, but big enough that the noise, spurious velocity vectors and uncertainty do not suppose a problem. For a cyclist, it was suggested that the size should be in the range $0.05c - 0.25c$, with c the characteristic length of the flow [20].

There is one more concern when the measured velocity data is used on a momentum balance calculation. Via linear error propagation analysis, Spoelstra et al. [20] concluded that the error in drag obtained via PIV and this method, caused by a random error in the velocity fields, is dependant on the variance of the random error and on the surface area where the integral is evaluated. The error leads to an underestimation of the drag, which was observed to have a quadratic relation with the error in the velocity fields.

For this reason, it is suggested that this area is reduced [2]: ideally, it would only include the wake. It is however essential that all the wake is included, as otherwise the total momentum difference between the flow upstream and downstream of the object cannot be properly accounted for and the drag will be underestimated [20]. This adds the complication of identifying the wake, which as explained in section 2.4, can be challenging.

In conclusion, PIV is one of the most popular flow measurement techniques at the moment because it is non-intrusive and it can provide time-resolved velocity fields on relatively large areas. Thanks to the momentum balance formulation, drag has been evaluated from PIV velocity fields successfully. However, all PIV measurements are subject to some errors and their consequent uncertainties, and in particular in the momentum balance formulation a random velocity error will cause the drag to be significantly underestimated unless the wake is contoured properly. In addition, the momentum balance method requires streamwise velocity fields, which can only be obtained with stereo-PIV, tomo-PIV or similar multi-camera experimental set ups. The complexity of the system makes it desirable to explore a method which would use raw images from a single camera.

2.2 Added Mass

This section is focused on the concepts that provide the backbone for the method used in this work: the energized mass, which is a real flow concept. It is inspired by the added mass, which is applicable to potential flow only, but that can serve as useful background to explain the energized mass concept. This section is structured as follows. An explanation of the added mass, its significance and its applicability to real flows is presented in subsection 2.2.1 and subsection 2.2.2. This is followed by a section on the drift volume in subsection 2.2.3, which provides useful insight to understand the physical meaning of the added mass and is required for some of the force formulations that stem from the added mass concept, which are presented in subsection 2.2.4.

2.2.1 Added mass in potential flow

A body accelerating through vacuum will have a lower inertia than the same exact body moving through a fluid with finite density. This increase is due to the fact that the body accelerating is

changing the kinetic energy of the fluid surrounding it. The only mechanism by which the work to change this kinetic energy can be done is with the drag of the body. This effect can be seen as if the fluid effectively moved with the body, so there is an additional inertia that is added to the body that is accelerating, as compared to when the body moves in vacuum.

Added mass originated as a potential flow concept and some of the first work on it was done by Lamb [48]. Examining the flow around a cylinder of infinite span and radius a moving with velocity U through a fluid at rest, the velocity potential in polar coordinates is given by:

$$\phi = \frac{Ua^2}{r}\cos(\theta) \tag{2.14}$$

and the stream function would be:

$$\psi = -\frac{Ua^2}{r}\sin\theta \tag{2.15}$$

The kinetic energy of the fluid surrounding the cylinder can then be computed as follows [48]:

$$2K = \rho\int \phi \mathrm{d}\psi = \rho(Ua)^2\int_0^{2\pi}\cos^2(\theta)\mathrm{d}\theta = \pi a^2\rho U^2 \tag{2.16}$$

Lamb [48] used this result to define $m_a = \pi a^2\rho$ as the mass of fluid that is displaced because of the motion of the cylinder. It was interpreted as an additional inertia to the body of the cylinder, which needs to be included in the calculation of the forces acting on it:

$$(m + m_a)\frac{\mathrm{d}U}{\mathrm{d}t} = F \tag{2.17}$$

From this result it becomes apparent that the inertia or added mass term m_a does not play a role on the forces when the velocity is constant in time. This derivation is for the simplified case of an infinite cylinder in potential flow, but this method to calculate the added mass can be used on any body for which the velocity potential is known. In addition, the added mass force is applicable to any body going moving with a non-constant velocity through a fluid at rest.

The same result can be obtained starting from the pressure distribution around the cylinder. In potential flow, the general pressure distribution at the surface ($r = a$) can be written as follows [49]:

$$p - p_\infty = \rho a\frac{\partial U}{\partial t}\cos(\theta) + \frac{\rho U^2}{2} - \rho U^2\cos(2\theta) \tag{2.18}$$

with U being the velocity of the cylinder, p the pressure and ρ the density. For the case of a steady velocity, the first term on the right hand side disappears, and the equation can be simplified as:

$$p = p_\infty + \frac{\rho U^2}{2}(1 - 4\sin^2(\theta)) \tag{2.19}$$

and the corresponding pressure distribution is shown in Figure 2.6 (a). This pressure distribution is constant and symmetrical, so there is no resulting drag. This phenomena is known as D'Alembert paradox. However, when the cylinder accelerates, the pressure field is no longer symmetrical, and so there is a resultant drag force. The unsteady term on Equation 2.18 generates a pressure distribution, so the total pressure field would be:

$$p = \rho a\frac{dU}{dt}\cos(\theta) + p_0 + \frac{\rho U^2}{2}(1 - 4\sin^2(\theta)) \tag{2.20}$$

The pressure field corresponding to the unsteady term only is shown in Figure 2.6 (b), where the cylinder would be moving towards the right. Clearly, the asymmetry of the pressure lines

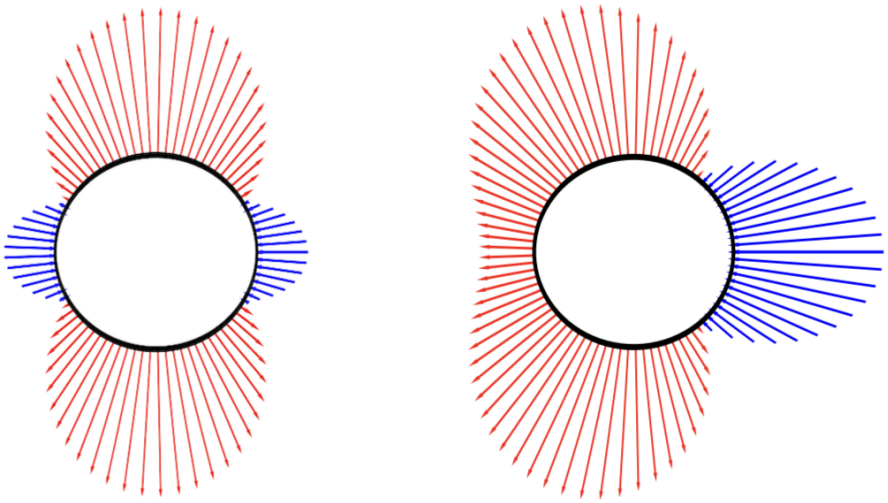

(a) Constant velocity cylinder **(b)** Accelerating cylinder

Figure 2.6: Pressure fields for a cylinder moving at constant and unsteady velocity, adapted from [49].

results in a force in opposite direction to the motion. The force resulting from this pressure difference can be found by integrating the pressure field over the cylinder:

$$F_{AM} = \int_0^{2\pi} \rho a \frac{\mathrm{d}U}{\mathrm{d}t} \cos(\theta) a \cos(\theta) \mathrm{d}\theta = \pi \rho a^2 \frac{\mathrm{d}U}{\mathrm{d}t} \tag{2.21}$$

Which leads to the same exact result as obtained by Lamb [48]: the added mass would be $m_a = \pi \rho a^2$, and the total drag force would be computed as $F = (m + m_a)\frac{dU}{dt}$.

Another way to understand the added mass concept is from an energy balance point of view, following Brennen [50]. The fluid around a body that accelerates (or decelerates) undergoes a change in kinetic energy. The work necessary to provide the fluid with this additional kinetic energy must be done by an additional drag force on the body, such that the energy balance can be written as follows:

$$F_{AM} = -\frac{1}{U}\frac{\mathrm{d}K}{\mathrm{d}t} \tag{2.22}$$

with F_{AM} being the additional drag and U the body velocity. Expanding the kinetic energy K with its definition $K = \frac{\rho}{2} I U^2$ (where $I = \frac{1}{U^2}\int (u^2 + v^2 + w^2)\mathrm{d}V$), the force can be expressed as:

$$F_{AM} = \rho I \frac{\mathrm{d}U}{\mathrm{d}t} \tag{2.23}$$

Examining Equation 2.23, it is clear that it has a similar form to the equation of the force required to accelerate a body $m\frac{\mathrm{d}U}{\mathrm{d}t}$. In this sense, the term ρI can be seen as a mass of fluid that is accelerated with the body, which is what causes the additional drag. Some works were undertaken later to tabulate the potential flow added mass of different shapes using similar methods [51] [52].

2.2.2 Added mass on real flows

The added mass force is derived from potential flow theory, which assumes inviscid and irrotational flow. Even though potential flow results are useful, there are certain cases in which they are not applicable. When the flow behaves very differently than potential flow or there are important viscous effects, it is necessary to apply other models to capture the unsteady drag. Some examples of these cases would be separated flows or vortex shedding [50] [53] [54].

Some of the first attempts to experimentally measure the added mass were done on disks and cylinders [55] and rectangles and parallelepipeds [56]. The results agreed well with the theoretical values, and any constant factor of error was attributed to the assumptions used by Lamb (like an infinite control volume). This work showed that the added mass is big enough in magnitude to not be neglected, and confirmed the results of Lamb. Furthermore, these studies led to the conclusion that the added mass of an object depends on its geometry (size and shape) and the fluid where it travels.

More recent studies have attempted to model the unsteady drag of an accelerating object using the potential flow of added mass, with not much success. Grift et al. [57] calculated the added mass in a submerged plate in a similar motion to a rowing blade, while Fernando et al. [58] did added mass measurement on a flat plate normal to the freestream. In both cases, a discrepancy of around 20% was found between the modelled drag and the measurements. Both modeled the drag force as the steady component plus the added mass contribution, and concluded that the entrainment was mainly responsible for the discrepancies. The entrainment is the mechanism by which irrotational fluid outside a wake (or any other turbulent flow) gains vorticity and becomes part of the nearby turbulent flow.

2.2.3 Drift Volume

Before looking at the different formulations that have been derived to calculate the drag coefficient from added mass perspective, it is important to introduce the drift volume concept, as it will be necessary to use it in some of them.

The concept of drift volume is strongly linked with the added mass, and it was first introduced by Darwin [59]. When a body moves through a fluid, the fluid particles surrounding the body move with it. The drift volume is then the volume the particles are displaced, from their position at rest, because of the body motion. Suppose there was a plane of particles at rest in an infinite fluid, and the object moved across this plane and into infinity. The drift volume would be the integral between the final position of these particles and their initial location in the starting plane. Such a scenario is depicted in Figure 2.7.

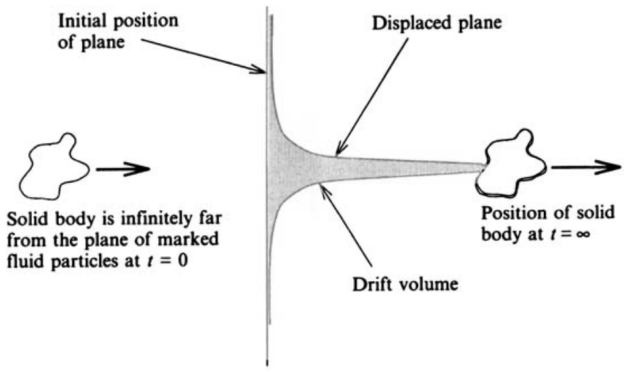

Figure 2.7: Depiction of the drift volume proposed by [59], from [60].

The drift volume corresponds to the hydrodynamic mass, or added mass. Therefore, it can be expressed as follows:

$$V_D = \frac{m_a}{\rho} \tag{2.24}$$

This proposition generated interest and discussion [61] [62] [63]. Eames [60] revised the work of Darwin [59] and pointed out that his proposition could only work for the case where the marked plane had an infinitely large radius, and was placed at an infinite distance from the sphere initially. He defined the partial drift volume as the volume enclosed between the initial and final position of the particles in the marked plane, when both the radius of the plane and the initial distance from the body to it were finite.

Bush and Eames [64] measured the drift volume on a bubble with high Reynolds number experimentally. They were able to capture with PIV measurements and particle tracking the elliptical trajectories of the fluid particles that are part of the drift volume, which are shown in Figure 2.8. It is also possible to observe that far from the centreline, the displacement is negative with respect to the starting plane, which shows the reflux.

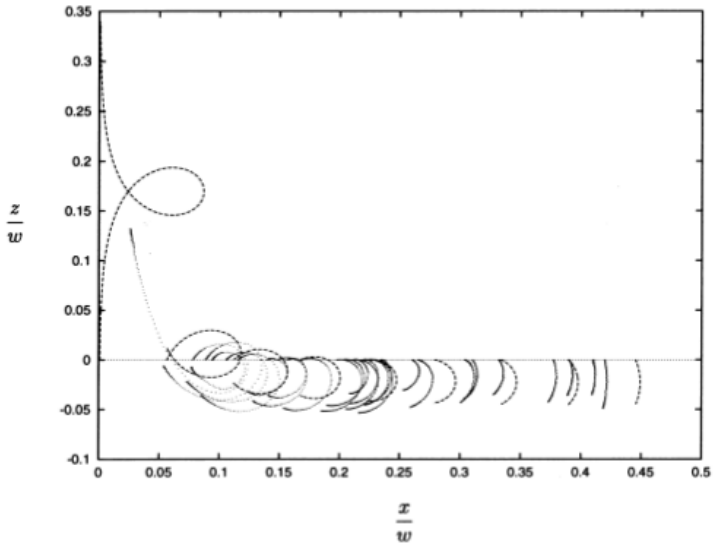

Figure 2.8: Trajectories of particles affected by the motion of a sphere, from [64].

2.2.4 Force formulations for added mass

In literature there have been several attempts to calculate the unsteady drag of an object using the added mass force. What follows is a summary of some of them.

Dabiri [65] developed a method to calculate fluid forces using a combination of the vorticity field of the fluid and the added mass. Starting from the following equation, derived by Saffman [66]:

$$\boldsymbol{F} = \rho \frac{\mathrm{d}}{\mathrm{d}t} \int \boldsymbol{x} \times \boldsymbol{\omega} \mathrm{d}V_V + \rho \frac{\partial}{\partial t} \int \phi \boldsymbol{n} \mathrm{d}S_V \tag{2.25}$$

where $\boldsymbol{\omega}$ represents the vorticity (which is integrated in the areas where it is present). Dabiri [65] rewrote this equation in terms of the added mass:

$$\boldsymbol{F} = V_B(\rho_B + \rho_F \boldsymbol{C}_{AM}) \frac{\partial \boldsymbol{U}}{\partial t} \tag{2.26}$$

where the subscript B indicates a quantity pertaining to the body and F the fluid in which it moves, and $\boldsymbol{C}_{AM}$ is the added mass tensor, which contains added mass coefficients for each

direction of acceleration in relation to the forces in all directions that result from them. The force then depends only on the added mass coefficients, the motion of the body and the densities of the body and fluid. Based on the definition of the drift volume, the added mass coefficients can be quantified as follows:

$$c_{ii} = \frac{V_{Di}}{V_B} \tag{2.27}$$

The added mass coefficient for each direction of motion can then be found dividing the drift volume V_{Di} in this direction by the volume of the body V_B. The way to measure the drift volume in each direction would be applying a Lagrangian approach, which would track the trajectories of the particles to determine the volume between a plane of particles at the start and the plane of the same particles after the body has passed.

In general, there has been success when considering the added-mass to be a contribution to the non-circulatory forces [67] [68]. For example, Corkery, Babinsky and Graham [69] proposed a method based on PIV data to measure the added mass vorticity. Taking as experimental cases the flow around translating and rotating plates, the added mass vorticity was compared to the vortex sheet model from potential theory. Following Leonard and Roshko [70], Eldredge [71] and Wu [72], they identified the added mass vorticity using the vorticity in the boundary layer of the plates. In potential flow theory the vorticity in the vortex sheet is non-circulatory, meaning that it is caused by the motion of the body itself and not the external flow, so they related it to the non-circulatory added mass. Even though the analysis was applied to highly separated flows, good agreement was found between the experimental results and potential flow predictions.

McPhaden and Rival [73] also calculated the drag using the added mass concept but with a different approach. In this case, the force formulation presented by Rival and van Oudheusden [5] was the starting point:

$$\boldsymbol{F}(t) = -\rho \iiint \frac{\partial \boldsymbol{U}}{\partial t} \mathrm{d}V - \rho \iint \boldsymbol{U}(\boldsymbol{U} \cdot \boldsymbol{n}) \mathrm{d}S + \iint \boldsymbol{n} \cdot (-p\boldsymbol{I} + \boldsymbol{T}) \mathrm{d}S \tag{2.28}$$

The first term (the unsteady term) can be seen as the added mass, as it is some mass of fluid that is affected by the body velocity. In order to measure it, they use a drift volume approach. Since the drift-volume from a single plane is not enough to understand the time development of the added mass, they developed a multi-plane drift volume approach, which they tested on circular flat plates accelerated from rest. Using this method they were able to measure the force during the acceleration phase with only 3% error, and show that the potential flow added mass was unable to properly predict the force. This shows the importance of considering the time evolution of the added mass.

2.3 Energized Mass

While the concept of the added mass can help understand the energized mass idea, it is important to separate the two. The added mass concept comes from potential flow, and as explained in the previous section will only come into play for accelerating flows. The energized mass, on the other hand, can be used to compute the drag of bodies undergoing steady, translational motion.

When a body moves through a fluid with constant velocity, the fluid surrounding it, initially at rest, will undergo a change in velocity. The energized mass can be understood as a measure of the change in normalized kinetic energy of the fluid. It includes all the fluid that experiences a change in velocity [74]:

$$m_e = \rho \int_{\infty} \frac{u^2 + v^2 + w^2}{U^2} \mathrm{d}V \tag{2.29}$$

Where the control volume would have to be large enough to encompass all the fluid affected by the motion of the body. The energized mass has units of mass, but also includes a measure of the normalized kinetic energy of the fluid. This is a useful definition because the reference system can be changed to express the force equation in terms of this displaced fluid. The system then consists of the body that is moving in addition to the energized mass that changes in time.

The drag can be expressed as follows:

$$F_D = \frac{\mathrm{d}}{\mathrm{d}t}(m_e \cdot U) \tag{2.30}$$

In a similar way that the added mass is an additional inertia to the body, in this case all the fluid that gains kinetic energy is added to the energized mass, which changes in time. The equation is able to capture the force required to provide the fluid with this change in kinetic energy, which is performed by the drag of the body. The acceleration term of Equation 2.30 is similar to added mass term that needs to added in accelerating flows. In fact, for potential flow the energized mass in this term m_e would be the same as the added mass [74]. In the case of a steady, rectilinear motion, this term would drop out as U would be constant in time, and the drag could be expressed as follows:

$$F_D = \frac{\mathrm{d}m_e}{\mathrm{d}t} U \tag{2.31}$$

Another way to understand the energized mass concept is to balance the work done on the fluid. As explained earlier, in the case of a body moving with constant velocity through some fluid initially at rest, the only mechanism by which the kinetic energy of the fluid K can change is by the work performed by the drag of the body. This can be expressed as:

$$F_D \cdot U = \frac{\mathrm{d}K}{\mathrm{d}t} \tag{2.32}$$

The definition for the kinetic energy of a control volume of fluid would be:

$$K = \int_{CV} \rho(u^2 + v^2 + w^2) \mathrm{d}V \tag{2.33}$$

Inserting this definition into Equation 2.32 (and dividing and multiplying by the constant U):

$$F_D = U \frac{\mathrm{d}}{\mathrm{d}t} \int_{CV} \rho \frac{u^2 + v^2 + w^2}{U^2} \mathrm{d}V \tag{2.34}$$

which is exactly Equation 2.31 when using the definition for the added mass m_e given in Equation 3.1.

The energized mass method has already been used to calculate the drag on moving spheres by Galler, Weymouth and Rival [74]. In this case, the motion consisted of an acceleration from rest to a terminal velocity, which remained constant afterwards. Figure 2.9 shows the forces obtained with direct measurements and using the energized mass method. The drag during acceleration and relaxation phase of the motion could be captured well, but the research was not focused on the steady part of the motion.

Using a similar experimental set up consisting of a sphere accelerating from rest until it reached a certain velocity, Galler and Rival [1] used the energized mass approach to study the behavior

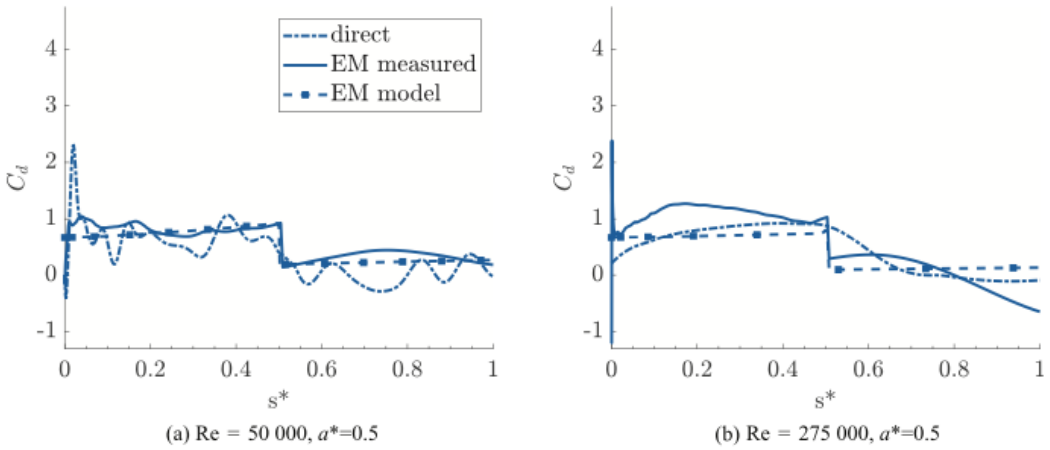

Figure 2.9: Drag coefficient history for a sphere at Re=50 000 and acceleration $a = 0.16m/s^2$, obtained with direct measurements, the energized mass method and a model for the energized mass, from [74].

of non-Stokesian tracker particles. In this case the energized mass was also found to be a good method to calculate the drag during the acceleration and relaxation phases of the sphere motion, as compared to direct force measurements. Figure 2.10 shows the particles that have undergone a change in kinetic energy (which constitute the energized mass) at two different moments of the motion.

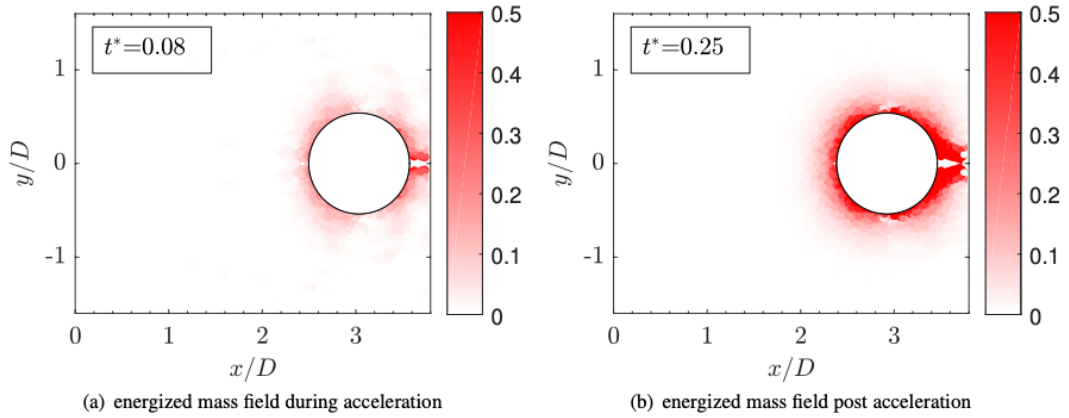

Figure 2.10: Development of the energized mass around the sphere, shown at different times. The color indicates instantaneous kinetic energy normalized by the kinetic energy of the sphere, from [1].

It is clear from Figure 2.10 that the energized mass expands as the sphere moves and the wake develops. It was possible to capture the increased drag force during the acceleration period and the following decrease when the acceleration stopped and the sphere had a constant velocity.

Galler, Rival and Weymouth [75] performed simulations of a sphere undergoing a similar motion (acceleration from rest followed by a period of constant velocity) for different accelerations and final Reynolds numbers. It was found that the development of the energized mass was dependant on both Reynolds number and acceleration. Studying the effect of the entrainment on the energized mass, it was measured that after the sphere had moved a distance of 3 diameters, 15% of the energized mass was due to the mass entrained into the wake when Re = 50 000.

In conclusion, the added mass and energized mass are similar in the sense that they derive information about the forces acting on the body by evaluating the effect the body has on its surrounding fluid. It is important to understand that they are not the same concept, as the added mass only refers to bodies that have an acceleration, and it is potential flow concept.

Even though it is a relatively new approach, the literature indicates that the energized mass is a promising and reliable method to calculate the drag force on a body undergoing acceleration. There is no literature yet that focuses on the application of this method to bodies moving with a constant velocity, this will be the focus of the this work. Using the energized mass would make it possible to derive information about the drag of an object based on its wake development only, without requiring detailed velocity fields upstream and downstream of the body.

2.4 Wake Identification Methods

The wake of an object can be defined as "the defect in stream velocity behind an immersed body in a flow" [76]. In general, it is the region of flow that is affected by this object, downstream of it. Even though it is a well known and common concept, there is no quantitative, measurable definition for it. This means its identification is not straightforward. This section is focused on the different methods that have been applied to detect it.

2.4.1 Velocity based methods

Based on the definition for the wake given above, it seems intuitive to define the wake as the fluid that has a lower velocity than the undisturbed freestream. When using this approach, the most important step is the selection of the threshold that will be used to separate wake fluid from outside flow.

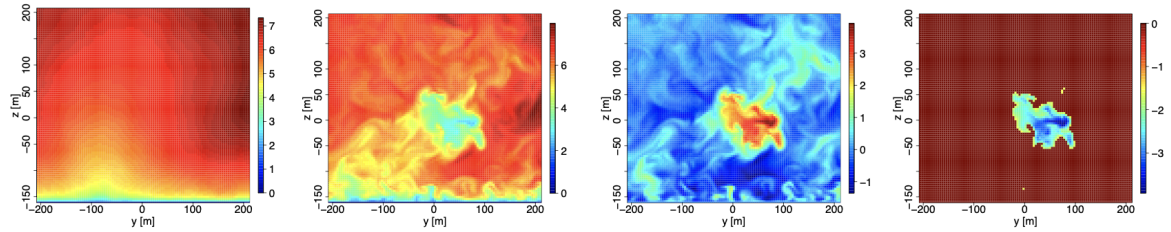

Figure 2.11: The (a) time-averaged undisturbed flow is subtracted from (b) the wake flow, and the result is presented in (c). The (d) identified wake is defined with a treshold of 40% of the maximum velocity deficit. From [77].

One option is to choose it as a percentage of the freestream velocity. A common method is to select a value of 95% of the freestream velocity to identify the wake [78] [79] [4]. Another possible way is to select the threshold as a function of the wake velocity. In this case, the maximum velocity deficit would be identified first, and then the wake would be defined as all flow that has a similar velocity, up to some percentage. For example, it could be all points where values are within 40% of the maximum deficit, as shown in Figure 2.11 [77]. After applying this threshold, it is also possible to use some additional processing to ensure that the borders of the wake are well defined [79].

The main advantage of this method is that it is simple to implement. However, selecting an appropiate threshold, and finding a good justification for it can be challenging. It is not clear from literature how sensitive the identified wake areas are to slight changes in the reported threshold values.

2.4.2 Vorticity based methods

The fluid inside the wake is rotational and therefore has non-zero vorticity, while the undisturbed flow is usually similar to potential flow. It should then be possible to identify the wake as a region

downstream of the body where there is vorticity. Once again, a threshold has to be established. When using the vorticity, it is not possible to set the threshold to zero, as PIV velocity fields will include some noise that will generate artificial vorticity outside the wake [80]. In addition, vortices will appear with opposite sings, and might have small regions of low vorticity magnitude in between.

An optimal value of $\omega = 0.7U_0/b$ was found, with U_0 the mean velocity deficit at the centre of the wake, and b the width at which the wake velocity achieved half of the mean velocity value [81] [82]. This value was found by comparing the results obtained with different thresholds and selecting the one that yielded the best output.

2.4.3 Image based methods

The wake and a turbulent jet are similar in that they are turbulent fluid surrounded by irrotational fluid, usually at a slightly different speed. For this reason, it is possible to draw inspiration for methods designed to identify the turbulent non-turbulent interface (TNTI). The TNTI was first identified Basset, Hunt and Rogers [81], and it refers to the thin region of fluid which separates turbulent and non-turbulent flow.

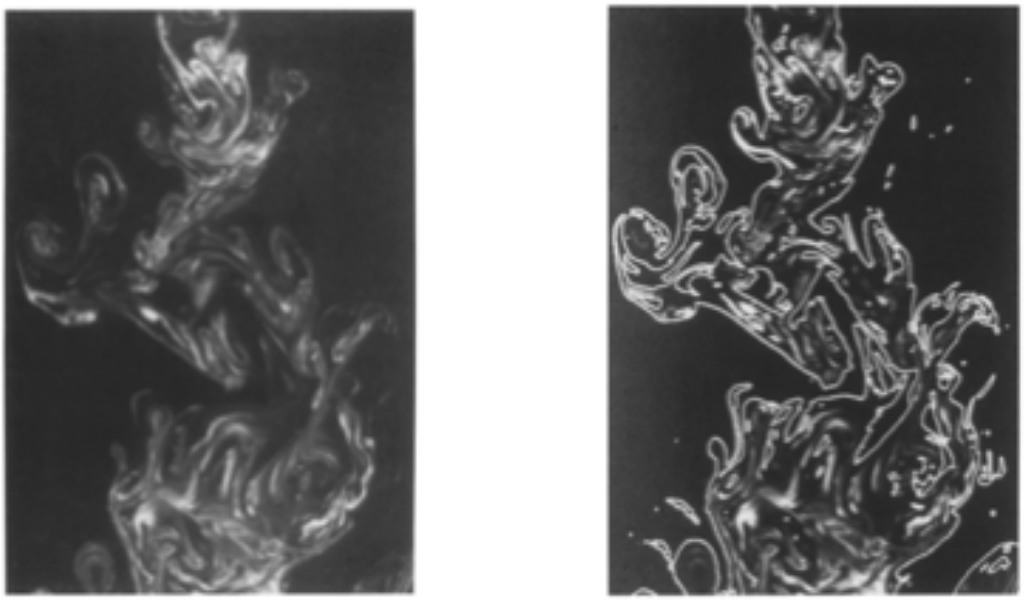

(a) Jet with LIF. **(b)** Jet with identified edges.

Figure 2.12: Jet (a) flow visualization and (b) identified edges, from [83].

Identifying the interface based on images can be done by first adding dye on the turbulent fluid, such that it is possible to distinguish it from the outside flow. An example of this is shown in Figure 2.12 (a). Then, a threshold for the intensity in the images can be set, so the died fluid will be marked as turbulent.

A possible approach to determine this threshold in an objective way is to examine the intensity distribution of the pixels for a given frame. If the distribution is binomial, then the threshold should be the local minimum between the two maxima. If it is not, then the average intensity calculated using only the pixels that are above the intensity threshold can be plotted as a function of the threshold. The intensity where the slope changes can be selected as the threshold [83]. The result of this threshold selection is shown in Figure 2.12 (b).

The method explained above yields a threshold that can be used to identify each pixel as wake or not wake, making them binary. The obtained images require some post-processing, including eliminating entrained (small areas with low dye intensity inside the main turbulent region) and

Figure 2.13: In white, the identified turbulent flow for (a) the initial threshold value, (b) double this value and (c) triple this value. From [84].

detrained (pockets of turbulent fluid outside the main turbulent region) fluid, and simplifying the boundaries so that a single vertical line only intersected the boundary once [85].

The sensitivity of the threshold selection method is shown in Figure 2.13. Even though the method was considered to be robust enough for the purpose of the work, it can be seen that the detected jet fluid does change depending on the value of the threshold.

This approach works well on jets because the turbulent fluid can be easily dyed, but on the wake of an object this would not be straightforward. Still, other characteristics of the wake, such as its velocity deficit, could be used to generate a difference in the intensity between the wake area and the irrotational fluid. This method also relies on setting a threshold, but in this case it is placed on the intensity value.

In conclusion, wake identification is complicated by the lack of a quantitative definition, but some success has been achieved with methods based on velocity, vorticity, and intensity thresholds. It still remains a challenge to find a strong justification for a particular value of a threshold.

2.4.4 Clustering algorithms

Even though so far clustering algorithms have not been used yet in wake identification methods, it will be an important step in the method presented here. Therefore, a short review of clustering methods is presented here with special emphasis on the DBSCAN algorithm, as it is the one used in the wake identification method.

Review of clustering algorithms

In general, clustering is simply a form of unsupervised classification. The objective of clustering algorithms is to assign to each point of the dataset a subset where it belongs based on some measure of similarity. They have been proven to be useful for a variety of applications, ranging from engineering and computer science (such as image segmentation, pattern recognition and machine learning) [86] to medical science (the most common application being diagnosis) [87] [88] [89].

The most commonly used categorization of this type of algorithms is hierarchical and partitional. The former construct the clusters by using a bottom-up or top-down approach and require a termination condition which determines whether the clustering process has ended. In a bottom-up or aglomerative algorithm, the data points are firstly regarded as individual groups and progressively merged into larger clusters until the termination condition is satisfied. Divisive or top-down algorithms work in the opposite way, by considering all data points as belonging to a single cluster at the start and dividing it into smaller ones.

The termination condition depends on the specific algorithm. A common similarity measure can be the distance between two data points, but it needs to be selected depending on the data type [90]. If this is the case, the termination condition would be reached when the distance between two clusters was smaller than the user-specified minimum distance. For single-link clustering algorithms would be the shortest distance between any two members of two clusters. In contrast, for a complete-link algorithm the termination condition would be the longest distance between any two members of two clusters [89].

The main advantages of hierarchical clustering are that they are versatile and relatively straightforward. They also output a dendogram, which is a data structure that shows all the partitions that are reached at each step of the algorithm. They can be useful because they allow the user to select the partition and they provide a sense of hierarchy in the data. However, their time complexity is at least $O(n^2)$, which makes them undesirable for large data sets. In addition, the termination condition has to be specified [90]. Examples of hierarchical clustering algorithms include CHAMELEON [91], CURE [92] or BIRCH [93].

Partitional algorithms work in a different way. The user needs to specify a-priory how many clusters the data will be divided into. The algorithm starts with an initial division and iteratively modifies it in order to minimize an objective function. The most well-known algorithm of this type (and one of the most popular clustering algorithms in general) is k-means. In this algorithm, the objective function is the distance between the points of a cluster and its centroid, summed over all clusters. As shown in Figure 2.14, the optimization is done by assigning each point to the nearest cluster centroid and recomputing the centroid at each step until convergence is reached [94].

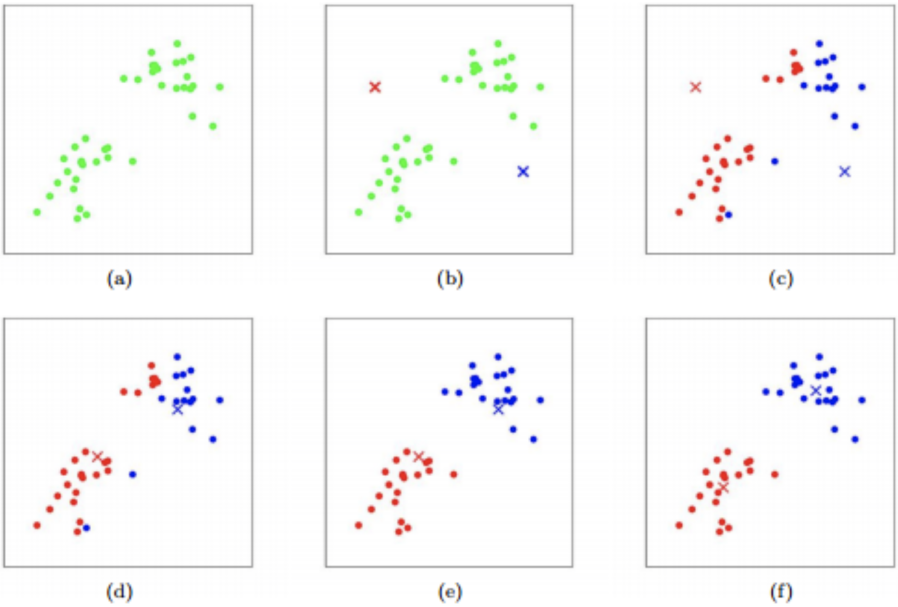

Figure 2.14: k-means example. Given an input number of clusters of 2 and (a) the initial dataset, (b) the centroids are calculated, and (c) each point is assigned to the closest centroid. This is repeated for several iterations (d, e) until (f) convergence is reached. From [95].

An advantage of partitional algorithms is that they are very fast. The time complexity for k-means is $O(k \cdot n \cdot t)$ in the worst case, where k is the number of clusters, n is the number of data points and t the iterations. Its simplicity also makes it a popular choice for clustering. However, it requires the user to specify the number of clusters at the start. In addition, the initial guess for the clustering distribution can have an effect on the outcome. It is also sensitive to noise and not suitable for clusters that are not isotropic [90].

For the type of clustering that will be needed in this project, it is essential that the algorithm does not require the user to specify the number of clusters at the start. Therefore, partitional

algorithms are discarded completely. Hierarchical algorithms provide a good alternative to this, but their runtime complexity is less than idea. A third category is considered: density based algorithms, of which the most famous example is DBSCAN.

DBSCAN

The DBSCAN (Density-Based Spatail Clustering of Applications with Noise) algorithm is density based clustering algorithm. This algorithm was developed in the 1990s by researchers at the Technological University of Munich. The motivation behind their work was to develop an algorithm that required minimal input information from the user, could detect clusters of arbitrary shape and was more efficient than the existing algorithms at the time [96].

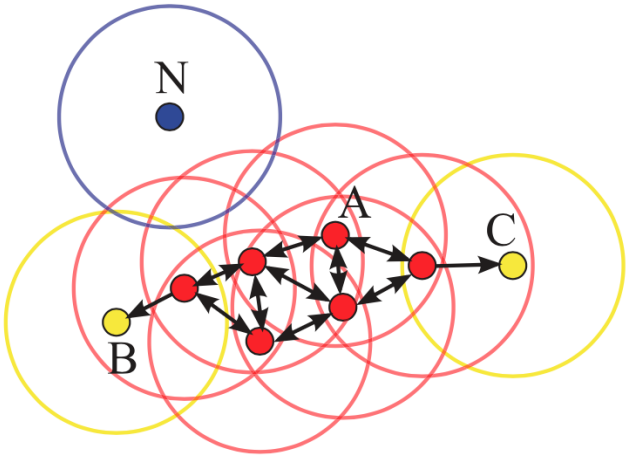

Figure 2.15: Illustration of the classification of points done by the DBSCAN clustering algortihm [97].

The novelty introduced with the DBSCAN algorithm was that it relies on the density of points for its classification. The idea behind it is that a point can be one of four types, as illustrated in Figure 2.15:

- **Core:** A point that is within distance eps from at least n points. In Figure 2.15, this would be represented by point A and all other points marked in red.
- **Directly reachable:** A point which is within distance eps from a core point. The yellow points B and C in Figure 2.15 belong to this category.
- **Reachable:** A point from which there is a series of consecutive points, each within distance eps from the next, in which the last of this series is a directly reachable point. In other words, there is a path of reachable points up to a core point.
- **Noise:** A point that is not any of the above types. This is exemplified by the blue point N in Figure 2.15, which is too far from any other point to be considered part of the cluster.

Starting with any point in the domain that is being analyzed, the algorithm determines which type of point it is. By doing the same in each point it is able to identify all clusters with a runtime of $O(n \log n)$ [96]. There are only two parameters that need to be specified by the user: the minimum amount of points n that need to be reachable for a point to be a core, and the minimum distance between two points to be considered reachable for each other, eps.

An important advantage of this algorithm is that there is no need to provide a number of clusters. Since the noise is completely dependant on the experimental conditions and especially

the seeding, it would not be possible to predict beforehand what number of clusters would be appropriate for all the runs. In addition, the fact that the DBSCAN is density based works well with this type of data, where the noise is expected to be much more sparse than the actual wake.

Chapter 3

Methodology

The objective of this work is to develop and test a method to obtain the drag coefficient of transiting objects without using the velocity fields, and relying only on images similar to those used for PIV. This chapter is centered on this method: its derivation and assumptions are first explained in section 3.1. Next, the processing steps that have been devised to implement it are detailed. The chapter concludes with a sensitivity analysis applied on the most relevant steps of the method.

3.1 Expression for the drag coefficient

The energized mass concept, first introduced by Galler et al. [1] is explained in detail in chapter 2. The main idea is that the energized mass is a measure of the kinetic energy of all the fluid that is affected by the movement of an object in it. If the fluid is initially at rest and the body transits through it, the energized mass is given by Equation 3.1 [74]

$$m_e = \rho \int_{\infty} \frac{u^2 + v^2 + w^2}{U^2} dV \tag{3.1}$$

With u, v, w the wake velocity components, U the body velocity and ρ the fluid density. The control volume needs to be large enough to include all the wake and any additional fluid affected by the passage of the body.

Galler et al. [74] have shown that the drag on a transiting body can be found by using the energized mass as follows:

$$F(t) = \frac{\partial}{\partial t}\left(m_e U\right) \tag{3.2}$$

Using this formulation, the energized mass can be calculated exactly if the velocities in the wake are known, assuming that the velocity of the object is known.

For the present work, the energized mass cannot be calculated directly, as the velocity fields will not be used. Instead, the drag is calculated starting from an energy conservation standpoint. The basis of the model is that the flow surrounding the body gains kinetic energy when the body moves through it. The mechanism responsible for this is the work done by the drag force. The energy balance is then:

$$F_D U = \frac{dK}{dt} \tag{3.3}$$

where F_D is the drag force, U is the steady velocity of the body and K is the kinetic energy of the fluid. In fact, if U is constant Equation 3.3 contains the same information as Equation 3.2, considering the definition of the kinetic energy:

$$K = \frac{\rho}{2} \int_{\infty} (u^2 + v^2 + w^2) dV \tag{3.4}$$

When the wake is fully developed, it is reasonable to assume that the only fluid that gains kinetic energy is the one in the vicinity of the body, that enters the wake. At a short distance from

the body, it is reasonable to assume that the wake velocity will be close to the body velocity in streamwise direction: $u \approx U$. In addition, the other two components v and w will be neglectable with respect to U. Thus, the kinetic energy of this fluid in the very near wake can be expressed as:

$$K = \frac{1}{2}\rho \int U^2 dV = \frac{\rho}{2} \int U^2 A_w dx \tag{3.5}$$

Here, A_w is used to denote the wake area at the body, when it has not been yet affected by entrainment. The volume of the fluid affected by the motion of the body has been expressed as the product of the this wake area and the distance from the body at which it is measured. It is assumed that the distance to the body is so small that entrainment does not have a strong effect on the wake area.

The wake area at the body A_w cannot be measured directly. Using the experimental set up described in chapter 3, information can only be extracted from images taken after the body is not directly illuminated by the laser sheet. A quantity that can be measured is A_m, which will be used to denote the measured wake area. This is the area of the wake that is detected with the processing steps explained in section 3.2. It will be measured at each position in the near wake. Clearly, A_m is a quantity that increases with time/position in the wake, while A_w is constant. The trend of growth of A_m will be extrapolated linearly to the position of the body, which yields A_w.

Once A_w is known, Equation 3.3 and Equation 3.5 can be combined in order to obtain the following expression for the drag force:

$$F_D = \frac{U^2 \rho}{2} A_w \tag{3.6}$$

Finally, the drag coefficient can be calculating by dividing this expression by the dynamic pressure and the reference area:

$$C_D = \frac{A_w}{A} \tag{3.7}$$

Throughout this work, A is used to refer to the frontal area which is used to normalize the drag force. In some cases, it will be more convenient to express the aerodynamic performance of an object in terms of the drag area $C_D A$ instead of the drag coefficient C_D. The reasons for this are explained in chapter 4.

In summary, the method presented in this work is based on the concept of the energized mass applied to an energy balance. There are several underlying assumptions which should be examined.

An important assumption is that close to the body, the wake velocity in streamwise direction is close to the body velocity ($u \approx U$), and the other two velocity components v, w are negligible in comparison. This is not a reasonable assumption in streamlined bodies. Therefore, the first limitation that can be underlined of the method is that it is restricted to bluff bodies.

It is also assumed that the wake area at the body, A_w, can be found by extrapolating the trend of the measured wake area A_m to the location of the body. It is assumed that the trend with which the wake area increases is linear. In addition, this implies that the distance from the first location where A_m is measured to the body will have to be determined for each case.

Finally, Equation 3.7 can only be obtained if the velocity of the body U is constant. The energized mass has been shown to be applicable to bodies undergoing acceleration [1] [75] [74]. For this reason, the main reasoning of the method would still work on accelerating bodies, but the expression for the drag coefficient would not be expressed in such a compact form.

3.2 Processing steps

As explained in section 3.1, the most important quantity that needs to be obtained is the wake area at the body A_w. Since it is not possible to measure it directly, it is extrapolated using the value of A_m in the near wake. This section explains in detail how A_m is calculated at each available frame.

One of the objectives of this work is to obtain the drag coefficient without using any velocity fields. The input is images of the flow with seeding particles, similar to those used to perform PIV. In this case they do not need to be from a stero-PIV set up, so a single camera plane perpendicular to the motion of the body would be sufficient. The steps that need to be applied to this raw images are depicted in Figure 3.1 and explained in the following paragraphs.

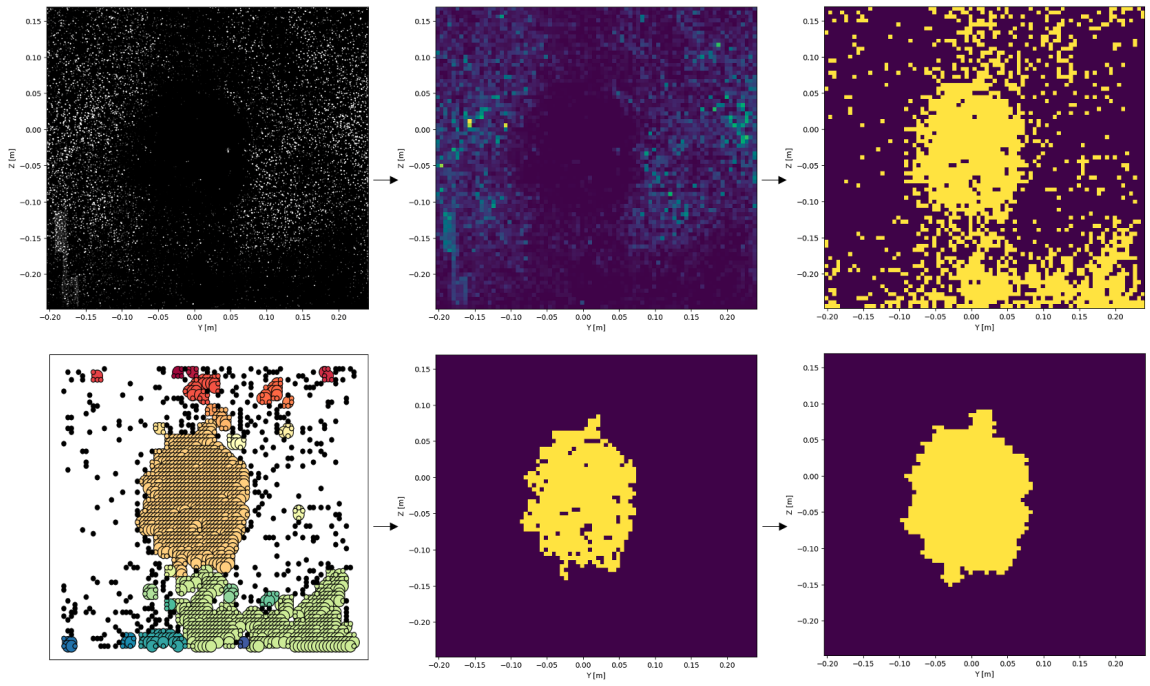

Figure 3.1: Steps followed to identify the wake from raw PIV images. The pre-processed image with sliding minimum filter (top left) is divided into windows where the intensity of the pixels is averaged (top middle). An intensity threshold is applied, and the windows with lower intensity are tagged as wake (top right). All the wake points are fed to a clustering algorithm (bottom left) and the largest cluster is selected (bottom middle). Any holes in the wake are filled in (bottom right).

Sliding minimum filter Starting with the raw images, some preprocessing is applied in order to reduce background intensity and prepare the images for the rest of the processing steps. The most important preprocessing step is applying the sliding minimum filter. This filter assigns to each pixel the lowest intensity value it has had in a series of N consecutive images. In this way, particles that have moved fast enough are eliminated from the result. When a particle moves, it appears in different pixels in different images, so the minimum value of intensity in any of these pixels will be the one corresponding to the particle not being there. As the object is the one that is moving, the wake has a higher speed than the environment fluid. The wake then appears as a darker area in the resulting image. The result is depicted by the first picture in Figure 3.1.

Window and intensity threshold The result from the sliding minimum consists of a 2D array of pixel intensity values for any single frame. On Figure 3.1 it might seem easy to distinguish with the naked eye the regions where there are particles, but it is not possible to assign a single

pixel a wake or non-wake tag unless its surroundings are examined. For example, a pixel with a low intensity value could be part of the wake or it could just be in between to particle images. For this reason, the image is divided into windows, where the average intensity is calculated in order to determine whether the intensity is low enough to be considered part of the wake. The result of dividing the preprocessed image into windows is shown on the second image of Figure 3.1, while the third image in Figure 3.1 depicts the windows that are below the intensity threshold.

Clustering These two first steps already provide an image of the wake, but it is very susceptible to noise. For this reason, the clustering algorithm DBSCAN is employed to determine which windows are truly part of the wake and which ones are noise. As shown in Figure 3.1 (fourth picture, bottom left), the clustering algorithm is capable of grouping points that are near each other. The largest cluster is identified as the real wake, and the rest of the points are discarded as noise.

Eliminating holes in the detected wake The final steps are done to produce a representation of the wake which is consistent with the flow physics. Just as there are some outer windows that are incorrectly tagged as wake, there are some wake windows that are tagged as outer fluid. In order to correct this, the edges of the largest cluster are found and everything inside them is considered to be part of the wake.

The outcome of these steps is shown in the bottom right picture in Figure 3.1. At each frame, a similar image will be obtained, which corresponds to the measured wake area A_m. From this, the wake area at the body is obtained by passing a linear fit and extrapolating the value of the wake area at the location of the body, which will be a certain distance before the first available frame. Some of these steps need additional explanation, which is provided in the next sections.

3.2.1 Sliding minimum filter

The sliding minimum filter is the principal mechanism in which this method relies to identify the wake area at each location of the near wake A_m. This filter effectively acts as a velocity threshold: only the particles that have a velocity high enough to cross the laser sheet in the time between the first and the last frame disappear. Even though the wake is one of the most fundamental concepts of aerodynamics, there is no clear measurable definition for it. It is usually described simply as a region of velocity deficit behind a body immersed in fluid [76] [40].

Some attempts have been made at identifying the wake of different objects. They are explained in detail in chapter 2, and they mostly consist on setting a threshold of some kind on the velocity field. This is a straightforward method, since the wake then consists of all regions with velocity lower than the threshold. The same principle is applied with the sliding minimum filter, but without the need for the velocity fields. Selecting a threshold is the most important part, as it will have a direct impact on the wake area.

In this work, a new way to select a threshold is used. It starts with the assumption that the wake has a Gaussian velocity distribution u_G, which in 2D is given by the following equation:

$$u_G(x,y) = A_G e^{-\left(\frac{(x-x_0)^2}{2\sigma_x^2}+\frac{(y-y_0)^2}{2\sigma_y^2}\right)} \tag{3.8}$$

Here, A_G represents the amplitude, which would be the highest value achieved by the distribution. In this case, it would be the body velocity U. Figure 3.2 shows the instantaneous streamwise velocity behind a sphere. In this case, the sphere had a diameter of $D = 0.1\,\mathrm{m}$ and was moving at a constant speed of $U = 1.33\,\mathrm{m\,s^{-1}}$. More details about the experimental

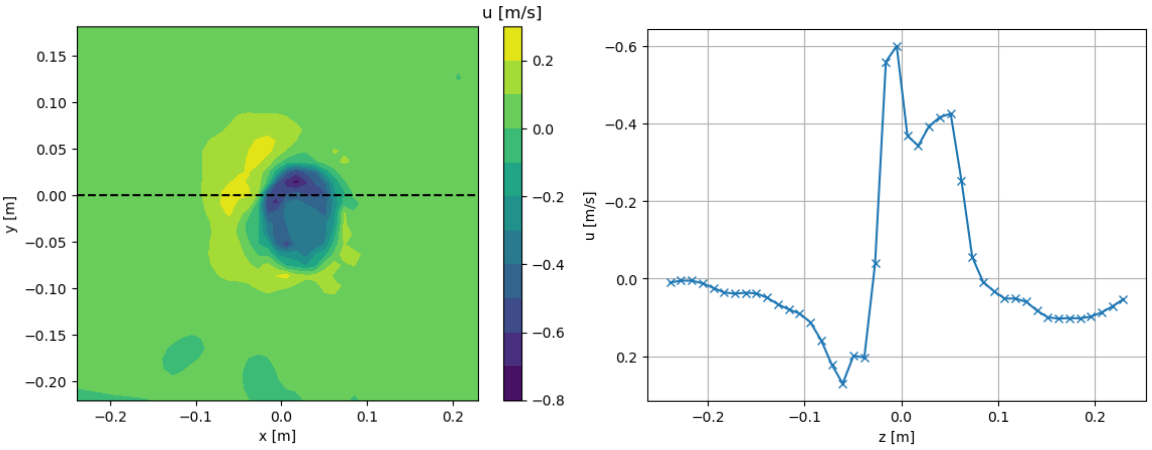

(a) Instantaneous streamwise velocity. The horizontal dashed line indicates the centreline ($y = 0$).

(b) Instantaneous streamwise velocity at the centreline ($y = 0$).

Figure 3.2: Velocity field in the near wake of a sphere.

campaign can be found in the work of Terra et al. [2] and in chapter 4. Figure 3.2 (a) shows the streamwise velocities as a 3D surface where the height is the value of u, while Figure 3.2 (b) shows the value of the velocity at the centreline of the sphere. The velocity u is the result from subtracting the environment velocity u_{env} (taken right before the passage of the sphere) to the wake velocity u_{wake}. Both show that even though the velocity profile is not a perfect Gaussian function, it is a reasonable approximation.

If the Gaussian distribution is symmetric ($\sigma_x = \sigma_y = \sigma$), and centred at the origin ($x_0 = 0$ and $y_0 = 0$) its volume can be found as follows:

$$V_G(R) = \int_{-\infty}^{\infty}\int_{-\infty}^{\infty} U e^{-\frac{(x+y)^2}{2\sigma^2}} dxdy = 2\pi U\sigma^2 \tag{3.9}$$

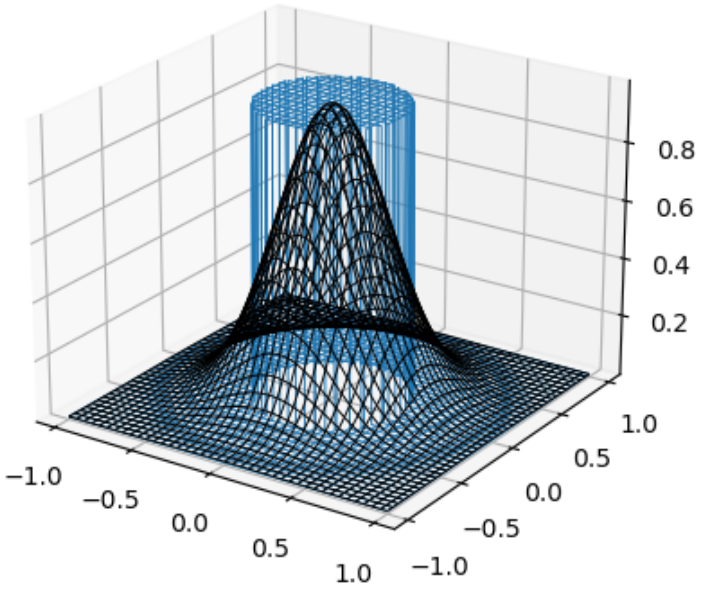

Figure 3.3: Illustration of a 2D Gaussian (black) and top-hat (light blue) distribution of same volume.

Such a Gaussian function is plotted in Figure 3.3 in black. On the same plot, the circular top hat distribution that would have an equivalent volume is superimposed. This top-hat distribution

of radius R and velocity U would have the volume:

$$V_{TH} = \pi R^2 U \tag{3.10}$$

If we set the volumes of both distributions to be equal, the radius of the top hat function would be $R^2 = 2\sigma^2$. The threshold velocity would be the value of the Gaussian distribution at this radius. Expressing Equation 3.8 in polar coordinates, this velocity:

$$u_G(r = R, \theta) = Ue^{-\frac{r^2}{2\sigma^2}} = Ue^{\frac{2\sigma^2}{2\sigma^2}} = \frac{U}{e} \approx 0.37U \tag{3.11}$$

Therefore the threshold that will be used to identify the wake will be $0.37U$. The idea is that the entire wake velocity is approximated as a top-hat distribution with velocity U and radius R. This can only hold for locations really close to the body (less than a characteristic length) where the wake velocity is u is close to U. The threshold is found by calculating the value of u_G at the intersection between the Gaussian and the top-hat profile. In this way, the wake is modelled as a top-hat profile, where the area of this profile is the same as the area of fluid with velocity higher than $0.37U$. The volume of the approximated top-hat wake is then the same as the volume of the original Gaussian wake.

In order to test this approach, it was applied first to the velocity fields that were available for some of the datasets. Even though the velocity fields will not be used to calculate the drag, they were helpful in order to understand if the idea for the method could work.

The curves shown in Figure 3.4 represent the obtained drag area using Equation 3.7 for different values of a threshold applied on the wake velocities. The velocity fields were obtained with PIV. The experimental methodology and processing parameters can be found in chapter 4, while more detailed explanations of the wake topology of a skater can be found in chapter 5. The reference value was obtained using the Ring Of Fire methodology [2] [4], which is based on momentum balance between the wake flow and the freestream flow.

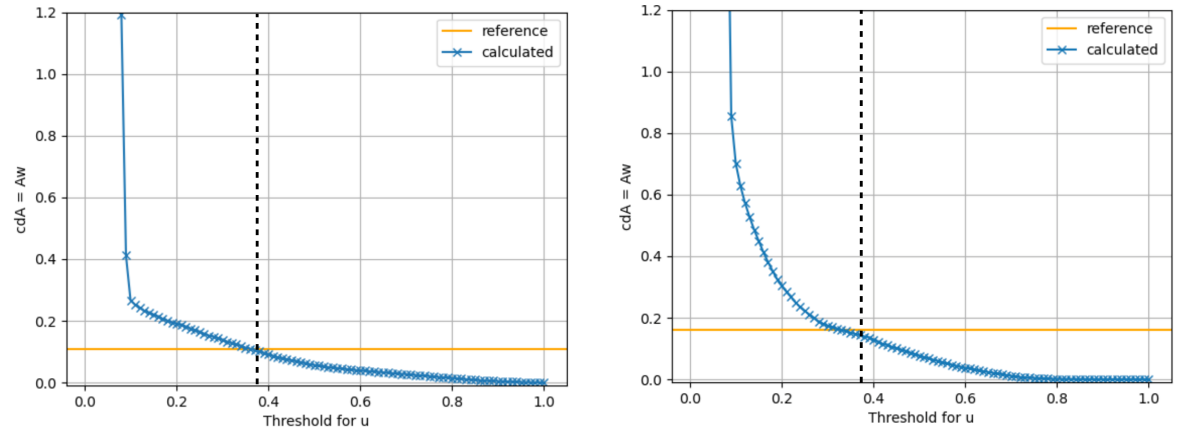

(a) Low drag. **(b)** High drag.

Figure 3.4: Wake area A_w obtained from Equation 3.7 using the PIV velocity fields with different thresholds for a skater in (a) low drag position and (b) high drag position. The vertical dotted line indicates a threshold of 0.37.

Figure 3.4 shows that in both cases, the optimal threshold value is close to $0.37U$. In particular, the optimal threshold for the low drag position skater, shown in the left, is 0.34, while for the high drag position skater it is 0.34. This confirms that the assumptions made in this section are reasonable: 0.37 is a good threshold for the velocity to obtain A_w, and Equation 3.7 is a suitable expression for the drag coefficient.

The shape of the curve shown in Figure 3.4 can also be explained. It is important to keep in mind that the wake velocity in this particular plot is normalized as follows:

$$u = \frac{u_w - u_{env}}{U} \tag{3.12}$$

Where u is the normalized wake velocity, u_w is the velocity measured at the wake, u_{env} is the freestream velocity and U is the body velocity. Therefore, fluid that moves at the same velocity as the body will have $u = 1$ and fluid that is not part of the wake will have $u = 0$. If the threshold approaches 0, fluid with very low velocity deficit that has been less affected by the body will be identified as wake, and as a consequence A_w is high. When the threshold approaches 1, only the fluid that is moving at the same velocity as the object is counted as wake, and so the A_w decreases. In later chapters, a different normalized wake velocity u^* is used, but in this case u is more convenient to showcase the effect of the threshold value.

This discussion leads to the conclusion that a threshold of $0.37U$ is optimal to identify the wake of an object. However, we want to propose a wake identification method that does not rely on the velocity fields, so this threshold value needs to be translated into a filter length for the sliding minimum filter. For this purpose, the filter length N will be calculated as the amount of images that are captured in the time interval that it would take a particle traveling at a velocity of $0.37U$ to cross the laser sheet, so it would not be illuminated anymore. This can be expressed as follows:

$$N = \frac{f\Delta z}{0.37U} \tag{3.13}$$

For each dataset, the acquisition frequency used for the PIV images f, the laser sheet thickness Δz and the body velocity U are known. Using Equation 3.13, the particles that have a streamwise velocity larger than $0.37U$ will be deleted from the resulting image and will appear as a darker area, similar to the one shown in the second image of Figure 3.1. However, the filter is not able to distinguish streamwise velocity from in-plane velocity. Any particles with high enough in-plane velocity to have a displacement larger than a full particle diameter in the time interval contained between the first and last frame will also be deleted. If the assumption that v, w are small is valid, this should not have a major impact on the results.

3.2.2 Window and intensity threshold

The result from applying the sliding minimum filter is shown in Figure 3.5 (a). This image, which consists of particle images and a darker wake area, is stored as a 2D array which contains values of intensities, one for each pixel. The values of intensity alone are not enough to determine whether a pixel is a particle. Firstly, the background, which appears black between the particles, does not always have a value of zero. In addition, different particles have different values of intensities, and some particles remain in what appears to be the wake area. It is therefore not possible to deduce whether a pixel is part of the wake or not based only on its intensity value and without considering its neighboring pixels.

In order to gain information about the surroundings of each pixel, the image is divided into windows that group a certain number of pixels, where the intensity is averaged. An example of this is shown in Figure 3.5.

The windowing technique is helpful to decide which points in the image are part of the wake and which ones are not. The window size needs to be chosen such that it is possible to make a distinction based on the average intensity values, and small enough that the shape of the wake is not affected. A more detailed explanation of the selection of the window size is presented in section 3.3. If the window size is chosen big enough, the low intensity pixels that are part of

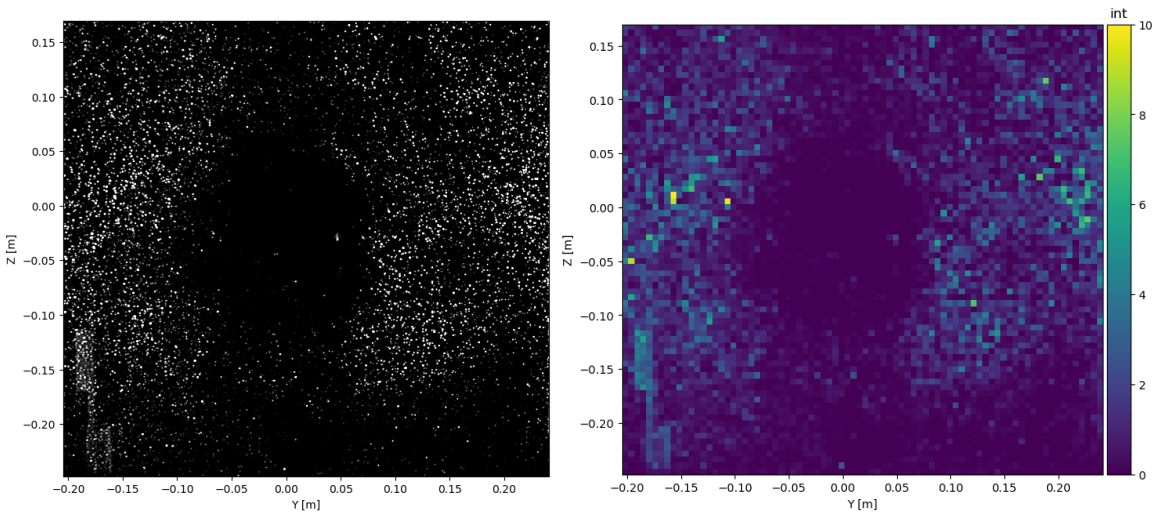

(a) Raw image with sliding minimum.

(b) Image divided into average intensity windows.

Figure 3.5: Result of sliding minimum filter and corresponding image after windowing and averaging the intensities at each window.

the freestream will be grouped into the same windows as the high intensity pixels nearby which correspond to particle images. The only intensity windows that will remain will low intensity values will be the ones in larger areas of low intensity, mainly the wake.

The next step is to set a threshold for the average intensity value. In this way, only windows with an intensity lower than the selected threshold will be tagged as wake. Again, this must be subject to a sensitivity analysis. The result of this step for the same image is presented in Figure 3.6

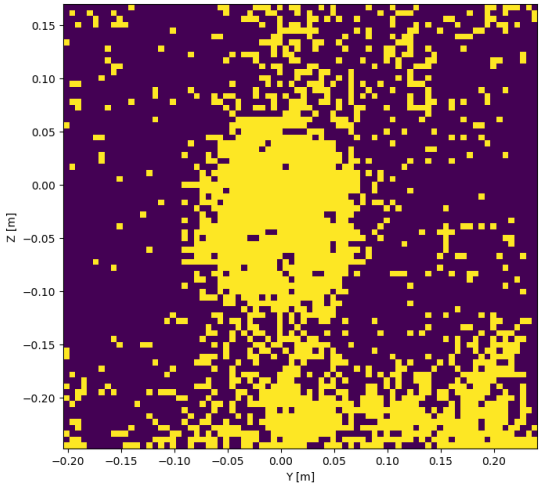

Figure 3.6: Points identified as being part of the wake (yellow).

The areas where there is noise are also identifiable at the top right corner, and at the bottom of the image. They are clearly distinguishable in Figure 3.5 as well, and they are a consequence of uneven seeding in the PIV set up. The wake of the skater itself is also not smooth, showing some holes and not smooth edges. Since the method relies on the wake area to calculate the drag, it is essential to reduce this noise as much as possible. It would lead to an incorrect overestimation of the drag of the body. In order to correct this, a clustering approach is chosen, which is explained in the next subsection.

3.2.3 Clustering

The previous subsection highlights the need for a method to reduce the noise. The chosen option is clustering. The assumption here is that the wake is composed of a single, compact area. If the wake is the largest area of low intensity in the windowed images, then the largest group of wake-tagged points is the wake. If there are other areas of low density in different parts of the image, they will not be grouped into the same cluster and will be discarded as noise.

The clustering algorithm used in this step is DBSCAN, which is explained in detail in chapter 2. In summary, it is a density based algorithm which only requires as input the minimum distance between two points such that they will be grouped into the same cluster, eps. The main advantage of this algorithm is that it does not require the number of clusters as a user input. The algorithm will automatically determine the number of clusters based on the density of the points. DBSCAN is also able to deal with noise, which is the main reason why it is used in this step [96].

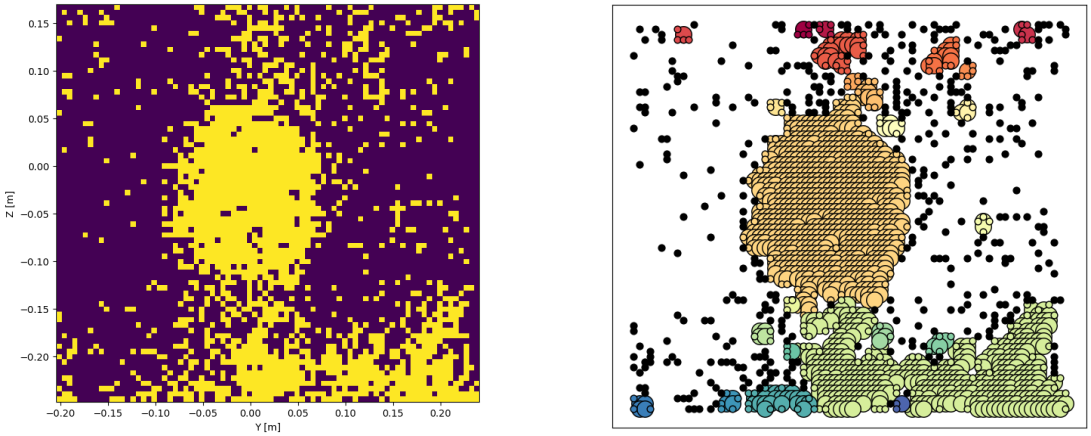

(a) Identified wake. **(b)** Clustering result.

Figure 3.7: Points that are given as input to the clustering algorithm (left) and its output (right).

Each different cluster, which is composed of a core point, and all directly reachable and reachable points, is presented with a different color in Figure 3.7. The black points indicate noise. The darker areas that are seen at the top right and the bottom are not identified as noise, but as separate clusters. In order to ensure they do not remain tagged as wake, only the largest cluster is maintained. In this case, it would be the red cluster at the centre of the image (in red), which clearly coincides with the expected skater wake.

During the development of this process, it was observed that the method leads to some variation from one frame to the next. This was caused by some intensity windows having slightly changes in the intensity values in two consecutive frames, with a large enough difference that they would not be tagged the same (wake or freestream) in both. This is not a common issue, so it usually does not cause a significant error, except in the case that these windows are located in a position where they determine whether a larger amount of windows are considered part of a larger cluster. For example, these windows which change tag might be located directly between two dense groups. If they are considered wake, all windows (both groups) will be considered part of the same cluster, but they might be divided into two clusters if the windows in between are not tagged as wake. This can lead to relatively large changes in the final measured wake between two frames. In order to correct this, the time history was considered: first it is checked whether the wake in the previous frame was larger than the wake in the current frame. If so, the two clustering solutions are compared to see which points were part of the largest cluster in the previous frame which in the current frame are not. This incorrectly labeled cluster is then changed to be considered part of the current largest cluster. This is not a common problem and

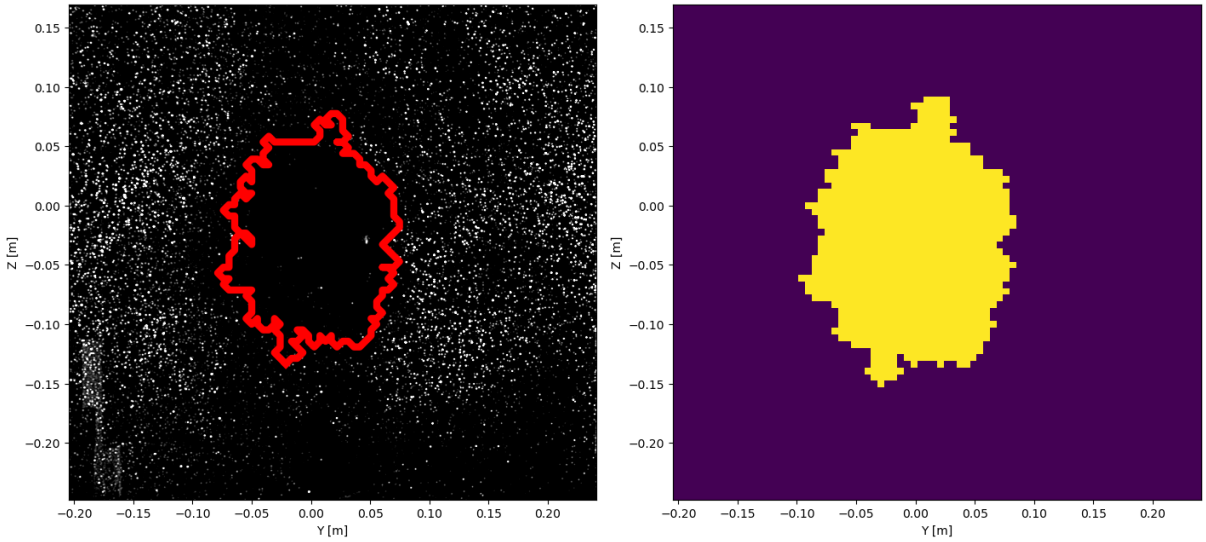

(a) Wake superimposed to preprocessed image. **(b)** Identified wake.

Figure 3.8: Final identified wake superimposed to the raw image with sliding minimum (left) and in yellow (right).

this solution cannot correct points that were not tagged as wake in the first place, but it is a first step towards implementing validation checks that consider the time history of the wake.

The remaining processing steps are straightforward. After isolating the biggest cluster, its edges are identified and filled in, so that the wake will be a solid area. The end result is shown in Figure 3.8. The comparison in Figure 3.8 (a) makes it clear that the wake has been detected properly.

3.3 Sensitivity Analysis

The methodology used to measure and calculate the drag of a transiting object has been explained in the previous sections of this chapter. The necessary parameters have been introduced without going into detail about the values used or justification for them. The exact values used for the test cases will be explained in chapter 4. In this section, a sensitivity analysis on each parameter will be performed. This is necessary in order to ensure the method is robust.

The parameters that will be explored are the sliding minimum filter length in subsection 3.3.1, the window size in subsection 3.3.2, the intensity threshold in subsection 3.3.3 and the clustering input parameters in subsection 3.3.4. In each subsection, all the parameters are kept constant with except the one that is being studied. The reference parameters are detailed in Table 3.1.

3.3.1 Sliding minimum filter length

In section 3.2 it was explained that the sliding minimum filter acts in a similar way as a velocity threshold but without the need for the velocity fields. In addition, the expression that is used to calculate the optimal value for the filter length was also introduced. Even though the previous subsection provides justification for the selected threshold value, it is important to examine how sensitive the filtered images and the obtained wake areas are to this parameter. The following sensitivity analysis is done on the skater data.

Table 3.1: Reference parameters in the sensitivity analysis.

parameter	value	units	description
body type	skater high drag position		model used in the experiments
N	5		sliding minimum filter length (number of consecutive images)
window size	10 x 10	px x px	size of the windows into which the preprocessed image is divided, the intensity of all pixels in a window is then averaged
threshold	0.05	counts	intensity threshold which determines whether a window is tagged as wake or outer flow
eps	1.5	windows	minimum distance between two points such that the clustering algorithm groups them into the same cluster

There are some documented attempts to identify the wakes of different objects. In some cases the threshold was placed on the free-stream velocity ([4], [78], [79], [98]), or the wake velocity deficit ([20], [77]). In other examples, a threshold on the vorticity was used ([81], [80], [82]). Finally, [85] introduced a new approach based on an intensity threshold to identify the interface between a turbulent jet and the surrounding fluid, which was used with successful results by others ([99], [100]). In these cases, the threshold used was found by trial and error. The results were examined for several different values and the one that yielded the best outcome was selected. In this section it will be examined how much of an impact the threshold selection has in the result.

The images that result from applying the sliding minimum filter with different filter length are presented in Figure 3.9. The data used is from a speed skater on a high drag position, with both arms extended to the side. As expected, when the filter length N is increased, the darker area, which corresponds to the wake, increases as well. As more time is encompassed between the first and last image, the particles that have lower velocities are able to cross the laser sheet, and therefore disappear from the resulting image.

This highlights the importance of selecting the sliding minimum carefully, and to perform a sensitivity analysis. The curves shown in Figure 3.10 present the area of the detected wake area as a function of the position behind the skater for different filter lengths. As is usually done in a sensitivity analysis, all other parameters are kept constant and the filter length is the only thing that is modified between the curves. There is a significant change in detected wake area when the filter length changes by only two images, meaning that it is not very robust and it is necessary to properly justify the selected value of N. In Figure 3.10, the data presented is from a single run. Using multiple runs would not bring additional information and would increase the computational cost.

As shown in Figure 3.10, for the particular case of the skater in a high drag position, changing the filter length results in a large change of the measured wake area A_m at all positions in the wake. For example, the average difference in area between $N = 3$ and $N = 5$ is of $0.43\,\mathrm{m}^2$, while the average difference in area between $N = 5$ and $N = 7$ is of $0.25\,\mathrm{m}^2$. The measured wake area doubles when using $N = 5$ compared to $N = 3$. These are significant differences, considering that the reference drag area $c_D A$ value obtained via momentum balance of of $C_D A = 0.16$. However, the trend of the curves is similar for the three filter lengths presented, and correspond to what was expected for the wake growth.

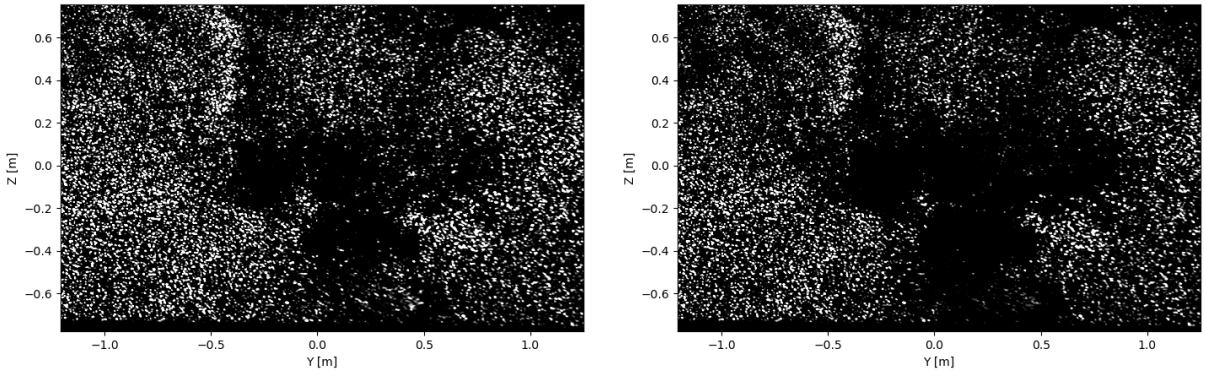

(a) $N = 3$.

(b) $N = 5$.

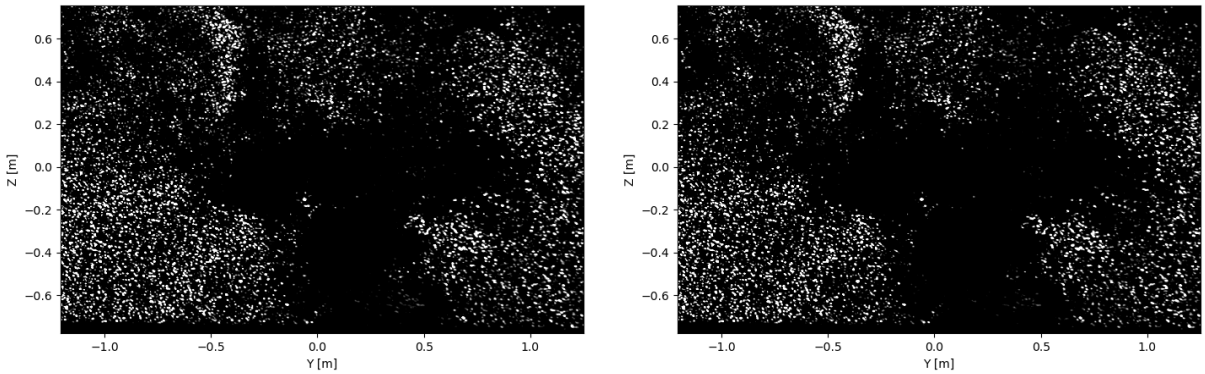

(c) $N = 7$.

(d) $N = 9$.

Figure 3.9: Images resulting from applying the sliding minimum filter with different filter lengths.

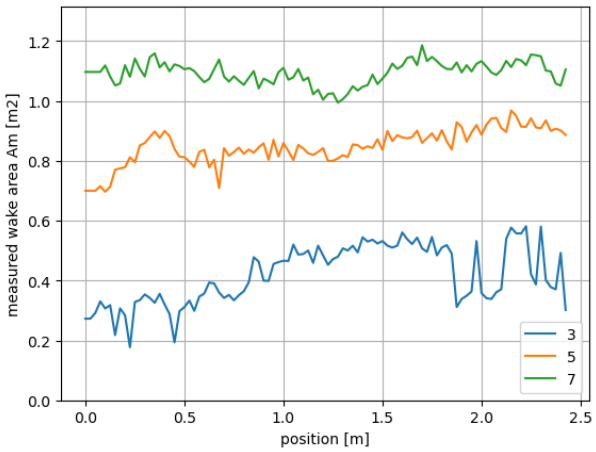

Figure 3.10: Images resulting from applying the sliding minimum filter with different filter lengths.

3.3.2 Window size

After applying the sliding minimum filter, the next step is to divide the resulting image into several windows, where the intensity will be averaged. Here it will be examined whether small changes in the size of these windows have a significant effect on the resulting detected wake area. This analysis will also be performed on the data of the skater in high position.

Figure 3.11 shows what happens to the image itself when the window size is increased or decreased. Clearly, the most evident effect is that the shape of the detected wake will loose resolution when increasing the window size. For window sizes of 50 and 100, the arms extended at the side are barely recognizable. The windows at the edge of the wake might

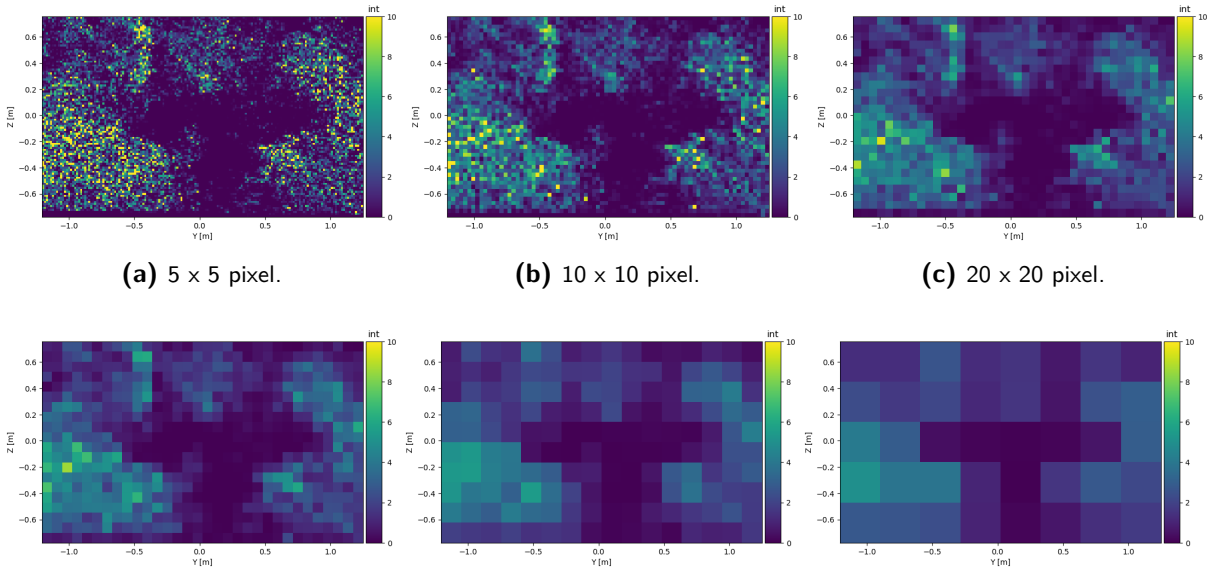

(a) 5 x 5 pixel. **(b)** 10 x 10 pixel. **(c)** 20 x 20 pixel.

(d) 25 x 25 pixel. **(e)** 50 x 50 pixel. **(f)** 100 x 100 pixel.

Figure 3.11: Images windowed with average intensity values for different window size, all for the case of the high drag position skater.

contain wake and non-wake area. If the windows are small, this is not a big issue as the error caused by this would be small as well. However, for large window sizes only the windows that are at the centre of the wake will be identified correctly, and the wake area will likely be underestimated. Another consequence of the window size is the value of the average intensity. If the window size is increased, the average intensity values overall are increased as well. This means that the intensity threshold has to be found in relation with the selected window size. Finally, a smaller window size leads to more operations, so is more computationally expensive. For example, reducing the size of the windows by half with respect to the reference value of 10 x 10 pixel makes the execution time of the script triple, while doubling the size of the windows can reduce it by a third.

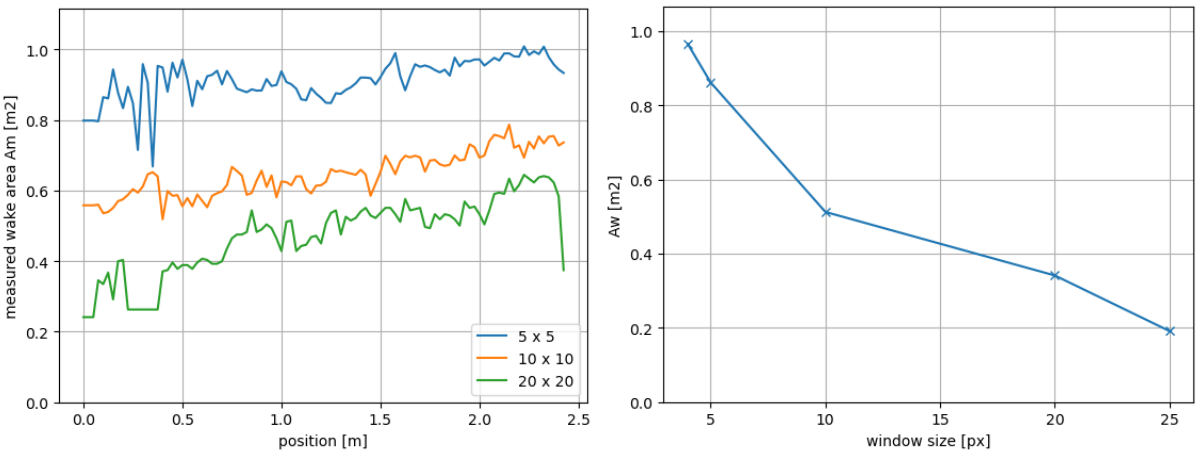

(a) A_m development for different window sizes. **(b)** A_w for different window sizes.

Figure 3.12: Effect of changing the intensity window sizes on the wake that is detected.

This effect is presented in a more quantitative way in Figure 3.12. Here, similarly to the plot shown in Figure 3.10, the same measured wake area A_m is plotted against the distance from the skater. The trend is that the smaller the window size, the bigger the area that is detected as wake. In Figure 3.12, the intensity threshold to tag a window as wake or outside flow is constant for all window sizes, which is not optimal as evidenced by Figure 3.11. Figure 3.12 (b) shows

that the effect of changing the window size also depends on the window size itself. The decrease in A_w for a small increase of the window size is larger for smaller window sizes. For example, changing from 5 x 5 pixel to 10 x 10 pixel almost halves the wake area. Instead, going from 10 x 10 pixel to 15 x 15 pixel is estimated to cause a reduction of 20% (interpolating Figure 3.12 (b)).

3.3.3 Intensity threshold value

In the section 3.2 it was discussed that the window size and intensity threshold should be chosen together, as the average intensity in a window will depend of its window size. In this way, if the window size is larger the threshold value shall be increased. After analyzing the effect of a change in window size in subsection 3.3.2 for a constant value of the threshold, here the window size will be kept the same and the threshold value will be changed.

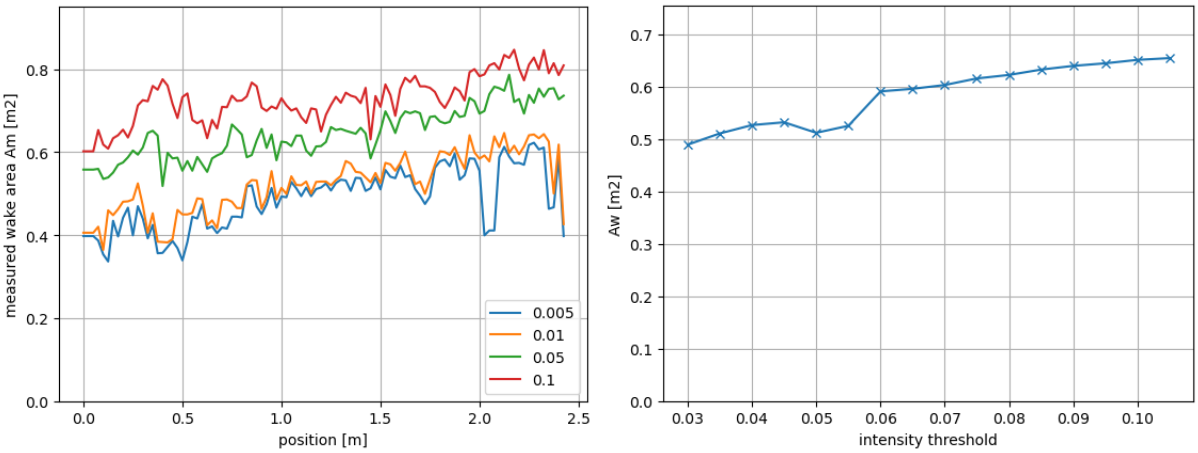

(a) A_m development for different window sizes.

(b) A_w for different window sizes.

Figure 3.13: Effect of changing the intensity threshold on the detected wake area.

Figure 3.13 shows the effect of the threshold value on the output result of the wake detection method. Figure 3.13 (a) shows the measured wake area A_m change with position for three different values of the intensity threshold on the left image. Figure 3.13 (a) shows the wake area A_w that is obtained for a range of thresholds, from 0.03 to 0.1.

As is logical, Figure 3.13 shows that increasing the threshold value will suppose an increase in the detected wake area. If the threshold had a value of zero, only windows where all the pixels had absolutely no intensity would be identified as part of the wake, and they would be scarce or non-existent. If the threshold was as high as the the intensity of a bright particle image, all the windows would be tagged as wake.

Figure 3.13 (a) indicates that the slope of the A_m curve is not strongly affected by this. A lower threshold value seems to lead to a slightly steeper curve, but the main effect is the shifting of the curve. Regarding A_w, Figure 3.13 (b) shows that the effect of the threshold depends on the value of it. If the threshold is initially small, a change in it will have a higher impact on the resulting A_w.

3.3.4 Clustering parameters

The last step for which a parameter is required from the user is the clustering. As explained in section 3.2, the most important parameter that is defined by the user in the DBSCAN clustering algorithm is the minimum distance between two points to consider them reachable from each other, eps. Here the effect of changing it will be examined.

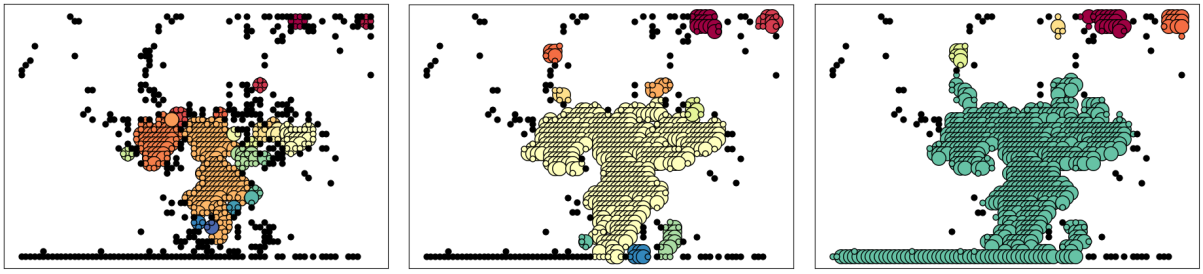

(a) 1 window. **(b)** 1.5 windows. **(c)** 2 windows.

Figure 3.14: Effect of changing eps on the clustering algorithm.

The effect of the minimum distance eps is shown in Figure 3.14. If the minimum distance is increased, points that are further away will be considered part of the same cluster, and therefore there will be less, bigger clusters. If it becomes too big, areas with low seeding on the background will be incorrectly identified as wake, as shown on the bottom right image in Figure 3.14. If, on the other hand, eps is too small, most of the points, including the ones that are in the wake, will be discarded as noise. Additionally, Figure 3.14 shows that in the case of the high drag position skater, a low value of eps makes the wake of the stretched arm be identified as noise and not part of the wake. This is expected to be less problematic for wakes which have a simpler shape.

The optimal value of eps depends slightly on the window size and intensity threshold. If these parameters are chosen such that points identified as wake before clustering are scarce, a larger eps will be necessary. Since the points are mapped into a grid where the distance between two neighboring points is of 1 window, in general eps = 1.5 will work best because it will include only adjacent points (on the sides and diagonals) in the same cluster.

In summary, this section has discussed a sensitivity analysis of the parameters that need to be specified in each processing step. It has been found that the sliding minimum filter length has a strong impact on the detected wake. Since there is no measurable definition for the wake, the latter is chosen based on assumptions on the velocity profile of the wake. In addition, the window size and intensity threshold have an influence on the wake area. They should be selected to work properly together and on a case by case basis. Finally, the parameter eps for the clustering should have a value of 1.5 if the window size and intensity threshold are chosen properly.

Chapter 4

Data Acquisition and Processing

This chapter is focused on the methodology that was followed to obtain and process the data that is used to test the method presented in chapter 3. For each case, first the experimental set up is described in section 4.1. In section 4.2 all the processing parameters that were used in the energized mass method are presented. In addition, since PIV velocity fields were used in all cases to better understand the wake topology, the PIV processing parameters are also explained.

In order to ensure the method to calculate the drag is robust, data from three different experimental campaigns is used: the flow around a skater, a cyclist and a sphere. The skater data was obtained for the purpose of this thesis in particular, in the context of a larger collaboration between the TU Delft and the Dutch speed skating team. For the other two campaigns, the experiments were conducted with the objective to demonstrate the Ring of Fire concept. The data was obtained, processed and presented by Spoelstra et al. [4] in the case of the cycist and Terra et al. [3] [2] in the case of the sphere. These two cases were included in this study because the data was readily available in the correct format, and it is very useful in determining limitations of the method presented in this work.

4.1 Experimental method

In this section, the experimental details of each of the campaigns are described. In the case of the cyclist and sphere experiments, only the most important parameters are included, since more detailed explanations are included in their dedicated publications [3] [2] [4] [20].

4.1.1 Skater

This subsection is focused on the experimental campaign conducted to obtain the skater data, which was carried out during February 2021. Details about the location, experimental methodology and equipment are included here.

Measurement location The experiments on a speed skater were performed on the ice skating ring of Thialf, in the village of Heerenveen, in the Netherlands. This facility is where the ISU World Competition is held. A full loop around the ice rink has a length of 400 m. It has three lanes, each with a width of 4 m. A sketch of the rink is presented in Figure 4.1. The recreational ice and the competition ice rink are separated by a padded fence.

The measurements were taken on one of the straight sections of the rink. A tent of dimensions 8 m x 12 m x 3 m was set up in the straight section, as indicated in Figure 4.1. This was done to ensure the seeding particles remained in the measurement volume, and for safety issues regarding the laser sheet. The tent consisted of truss structures with plastic on each side and on the top, and dark curtains that could be opened and closed at the front and back. It is shown in Figure 4.2.

The recreational ice was not being used, so the laser power supply and head were located there, and a small slit was cut into the side of the tent to avoid obstructing the laser. In addition, the Fluid Supply Unit (FSU) and the computers to operate the system were also located in the recreational ice. The seeding rake was located inside the tent, on the innermost skating lane,

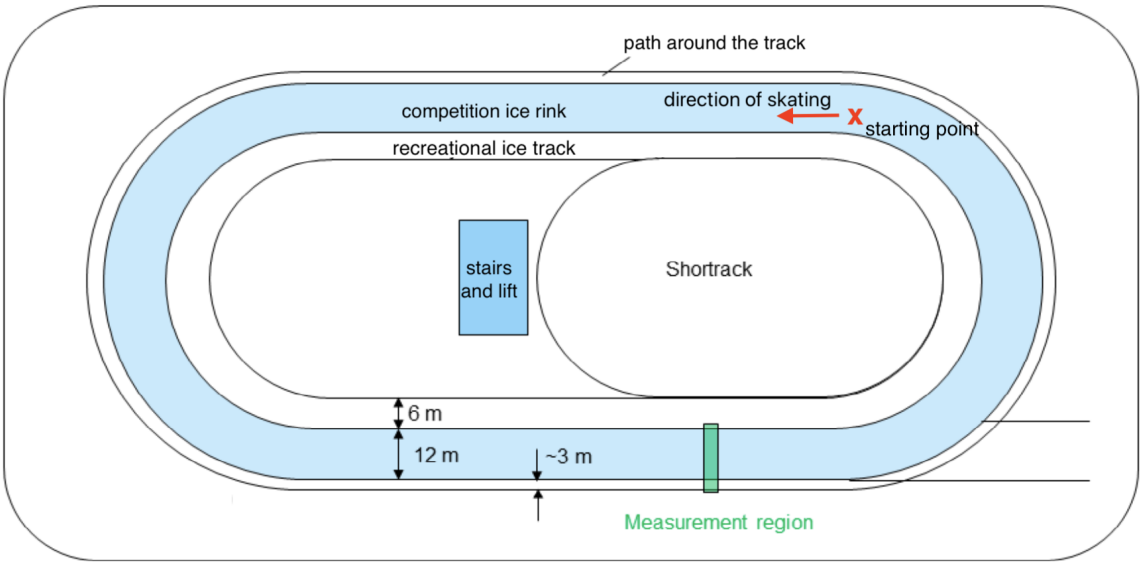

Figure 4.1: Thialf ice speed skating rink, adapted from [101].

while the skater used the centre lane. The skater that performed the runs was a professional speed skater wearing technical skates, skinsuit and glasses to protect his vision from the laser sheet.

Flow seeding The seeding particles used for this experimental campaign were Helium Filled Soap Bubbles (HFSB). They were selected due to their properties, most importantly their neutral buoyancy and ability to reflect light [27] and their adequacy to large measurement volumes [29]. In order to generate the bubbles, helium, and a soap solution were fed into the Fluid Supply Unit (FSU). The helium was kept in a tank, the air was compressed using a generator and the soap solution used was LaVision Bubble Fluid Solution, which consists of water, soap and glycerine. The pressure for the soap, helium and air was controlled via the FSU and it was set to approximately 3.8 bar, 3.8 bar and 3.7 bar, respectively. The values changed for each run, and they were adjusted based on the observed behavior of the bubbles. The exact values are tabulated in Appendix A.

(a) Tent.

(b) Equipment inside of tent.

Figure 4.2: Set up in the ice skating rink of Thialf.

The experiments started at the end of the day, when the ice rink was not being used for any events or trainings. The ventilation system in the rink was turned off, so the temperature decreased with time. In this case, since only 20 runs were performed, the temperature remained close to 10 °C throughout with a humidity of 55%. Because of the low temperature, the HFSB behaved slightly different than expected, and the proportions of helium, soap and air were adjusted to correct this. In addition, the soap was kept at room temperature whenever possible. The main

observation was that the particles tended to accumulate at the bottom of the measurement domain due to the lower temperatures.

The FSU was connected to a seeding rake developed by TU Delft Aerospace Engineering, which created the bubbles using nozzles. The rake consists of 12 wings, each of them with 17 generators, and is shown in Figure 4.3. In total, the seeding rake can generate $2 \cdot 10^6$ particles per second, with a diameter of 400 µm on average. The seeding rake was located on top of a table to ensure there were enough particles in the upper half of the measurement domain. A tray was put under the seeding rake in order to capture any leaking soap.

The potential effect of the soap on the ice was a concern for the campaign. In order to ensure the ice would not be damaged, tests were performed before the start of the campaign. HFSB were generated on a particular location on the ice, which was later examined. It was concluded that if the soap was cleaned using a Zamboni after the experiments, no damage was inflicted on the ice. For precaution, paper towels were laid on the ice directly in front of the seeding rake where most soap precipitates, as shown in Figure 4.2 (b). The towels covered only the innermost skating lane, so the skater was not affected by their presence.

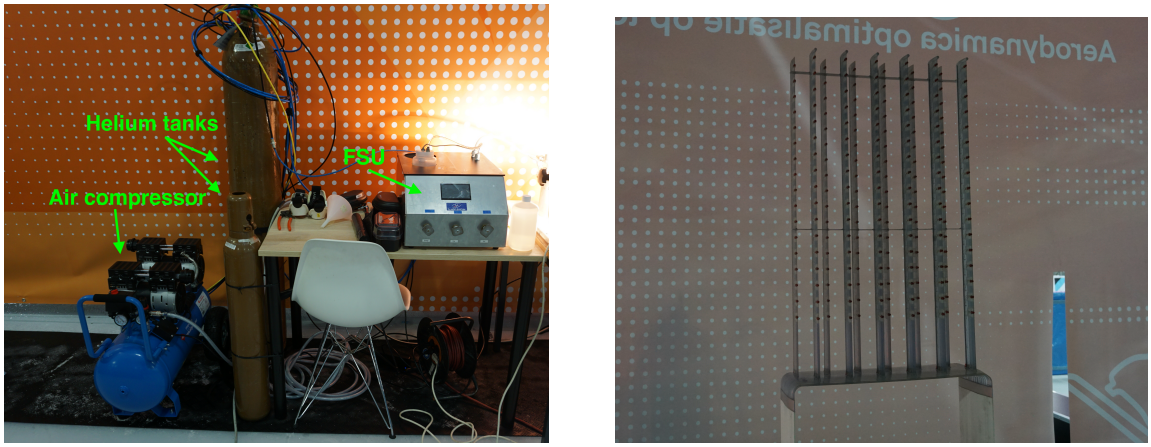

(a) LaVision Fluid Supply Unit (FSU). **(b)** TU Delft seeding rake.

Figure 4.3: Components of the flow seeding system.

Illumination system The particles were illuminated with a laser sheet. It was generated with a Quantronix Darwin Duo Nd:YLF laser, and had a wavelength of 527 nm and a pulse energy of 25 mJ at 1000 Hz. Together with the laser head, it was located in the recreational ice in Figure 4.1. Using cylindrical and spherical lenses, the laser beam was shaped into a sheet, which passed through a rectangular cut-out on the side of the tent. At the location where the skater passed, which was about 8 m from the laser head, the sheet had a height of approximately 2 m and a thickness of 5 cm. Black screens were placed around the laser head for safety.

Imaging system The images were taken using two LaVision HighSpeedStar 6 cameras with CMOS sensors with Nikon 50 mm lenses. The resolution of these cameras is of 1024 x 1024 pixels, but it was cropped to 1024 x 752 pixels, with the pixel size being 20 µm. They were set to a frequency of 500 Hz, while the f-number was 1.8 on the left side camera, and 4 on the right side camera. As shown in Figure 4.4, the left camera was more aligned with the direction of the laser light. Particles scatter more light in the direction opposite to the incoming light [23]. The consequence in this case is that more light was scattered in the direction of the left camera, so a lower f-number was needed for it.

The columns of the tent were used as attachment points for the PIV cameras. The seeding particle generator was located inside the tent. A schematic of how the items inside the tent

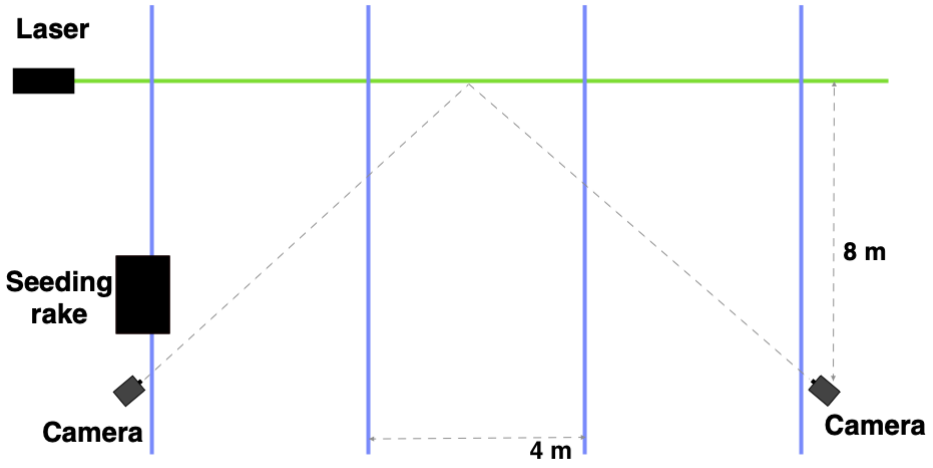

Figure 4.4: Schematic representation of the stereo-PIV set up, adapted from [101].

were located is shown in Figure 4.4. The cameras were at a distance of 8 m from the laser sheet, 12 m from each other and at a height of 3 m. The angle, as seen from the top view, was 45° with respect to the centreline. The vertical angle with respect to a horizontal line was of 15°.

Measurement conditions At each run, the following steps were repeated. First, the seeding particles generator was turned on, to allow enough time for the particles to be generated and to fill up the volume. The appropriate pressure values for the soap, helium and air were inputted to the FSU. This was done with the entrance and exit curtains of the tents closed. The amount of seeding inside the tent was inspected visually using the cameras. When it was enough, the name of the new run was inserted in Davis, and the skater was alerted with a visual signal that he could start the lap. He always started from the point marked in Figure 4.1 and advanced in counter-clockwise direction. As he moved through the rink, the curtains of the tent were opened. When he approached the start of the straight where the tent was located, the laser was triggered after giving an oral warning to all the people present for safety. At this point, the skater got into position and started gliding through the straight.

When the skater approached the tent, the cameras were triggered. After the skater exited the tent and the measurements were concluded, both curtains were closed again and the seeding particle generator was turned off. Of the recorded images, only 1000 were saved. The first image where the body of the skater was not directly illuminated by the laser sheet was identified, and the 500 images before were stored, together with the 500 images after that. A short break was done between each run in order to allow the skater to rest and receive any necessary feedback, and to store the data on the computer. This also ensured that the air in the measurement volume was not affected by the previous passage of the skater.

Twenty runs were performed in total, 10 for each position, in order to achieve statistical significance. The runs were performed alternating high and low drag positions, as shown in the processing matrix in Appendix A.

Skater positions In the high drag position, the skater had both arms extended horizontally to the sides of the body, and while the knees were flexed and the trunk inclined, he was more upright than is common in speed skating. The skater gained speed while approaching the laser sheet, and passed gliding through the laser sheet. This was done to avoid the need to consider the position of the legs and the difference in phase at each run. The position is shown in Figure 4.5 (a).

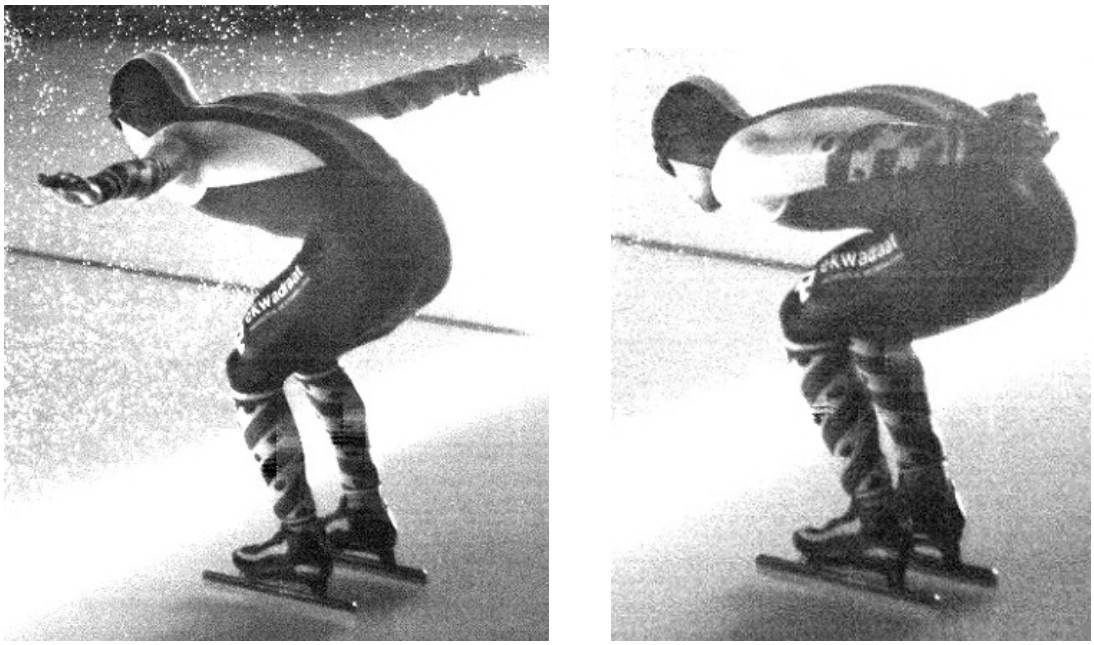

(a) High drag position. **(b)** Low drag position.

Figure 4.5: Speed skater positions tested.

There were 10 runs recorded on this position. Of these, there are three where the seeding is not good, so they were discarded and not used for processing. The seeding was not uniform, and some of the areas in the image that are clearly not part of the wake have a very low seeding, which inevitably leads to errors. Seeding issues and other sources or error are explained in Chapter 3. In addition, the laser sheet did not cover the lower part of the calves and feet for 5 runs (counting high and low drag position runs). This was corrected during the experiments. Of the remaining runs, two of them have a significantly higher seeding density than the rest, and therefore the threshold needs to be adjusted. In conclusion, 6 runs were processed.

The low drag position is more similar to the normal speed skating position: holding hands behind the body, and lowered torso. In this case, unlike in competitions, the skater glided while passing through the laser sheet, so the arms and legs do not move. The position is shown in Figure 4.5 (b).

A total of 10 runs were recorded in this position. Of these, 2 were discarded because of bad seeding conditions, that made it not possible to identify the wake. The reasons for this are explained in Chapter 3. Therefore, the results presented in the following chapter are obtained with the remaining 5 runs.

4.1.2 Cyclist

The images of a cyclist were taken during an experimental campaign to demonstrate the Ring of Fire concept, with which the drag of a transiting object is calculated via momentum balance. A more detailed description of the experimental conditions can be found in the work of Spoelstra et al. [4]. The set up consisted of a stereo-PIV set up. The experiments were performed on a tent of dimensions 3 m x 2 m through which the cyclist passed, in order to contain the seeding particles. The cyclist was riding a Ridley Cheetah TT bike and wearing a long sleeved suit, as well as a helmet and laser googles for safety, as he rode through the laser sheet. The set up is shown in Figure 4.6.

Flow seeding For this experimental campaign, Helium Filled Soap Bubbles (HFSB) were used as tracers. The pressure of the air, helium and soap solution was controlled by a LaVision Fluid

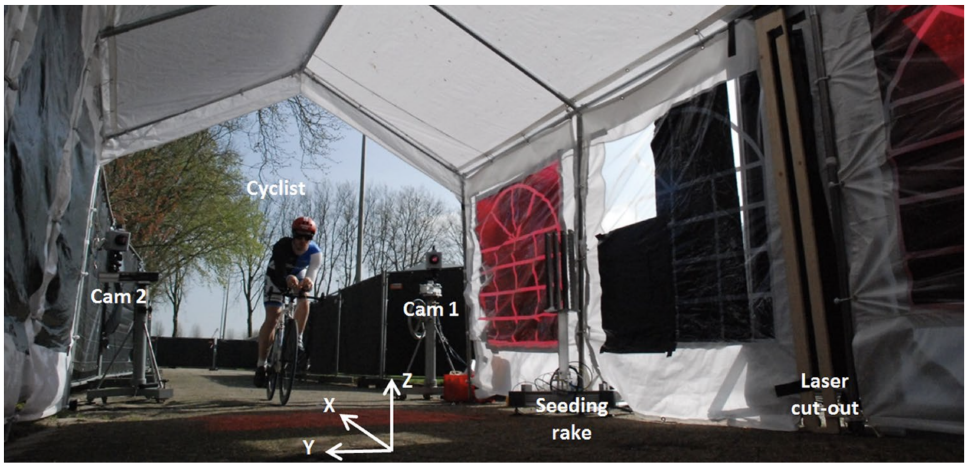

Figure 4.6: Experimental set up for the cyclist, from Spoelstra et al. [4].

Supply Unit (FSU), which was connected to a seeding rake with 80 nozzles and provided a concentration of 3 bubbles/cm.

Illumination system The laser sheet was generated using a Quantronix Darwin Duo Nd:YLF laser, the same as in the case of the skater described in subsection 4.1.1. Spherical and cylindrical lenses were used to create a sheet of height 1.8 m and 4 cm width at the point where the cyclist passed through it.

Imaging system The images were recorded using two Photron FasCAM SA 1 cameras, the same model as in the skater campaign (LaVision HighSpeedStar 6). They are CMOS cameras with a resolution of 1024 x 1024 pixels. The objectives used were Nikon with 50 mm focal length, and 532 nm bandpass filters were placed on them. The f-number was set to 5.6. The cameras were placed on tripods at the entrance of the tent, at a distance of 4 m to the laser sheet, and a stereoscopic angle of 31°.

Cyclist positions During the experimental campaign conducted by Spoelstra et al. [4], two different positions were studied. In cycling, there are four main positions: time-trial, hoods posture, drops posture and upright posture [102]. In this campaign, the upright and time trial position were studied.

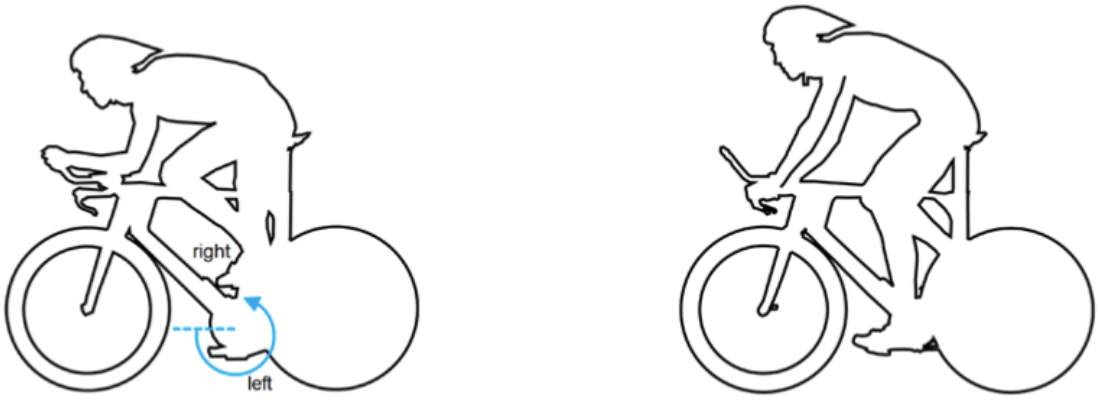

Figure 4.7: Depiction of cyclist in time trial position (left) and upright position (right) from Spoelstra et al. [4].

A schematic representation of both positions is shown in Figure 4.7 [4]. The left image shows the time trial position, where the cyclist rests his forearms in tri-bars, which allows him to maintain a lower position and reduce his frontal area. The time trial position has been reported to have a lower drag area than the upright position [103] [104] [105] [102] [106] [107], which is shown on the right in Figure 4.7. In the upright position, the hands of the cyclist are on the break hood, causing the torso to be at a higher angle with respect to the floor.

Another important consideration regarding the position of the cyclist is the crank angle. The crank angle indicates the position of the feet of the cyclist, which was not constant throughout the experiments because the cyclist was pedalling as he moved through the measurement domain. The position of the feet is of great importance in the aerodynamic of the cyclist, as is explained in chapter 5. The reference frame used in this work is the same was used by Spoelstra et al. [4], and is shown in Figure 4.7. The crank angle ϕ is measured with the position of the left foot of the cyclist. The reference axis is the horizontal line where the foot would be located if both feet were at the same height, and the left foot would be placed forward. In this way, a crank angle of $\phi = 0°$ or $\phi = 180°$ would represent a symmetric positioning of the legs, with the left foot and the right foot forward, respectively. The most asymmetrical crank angles would be around $\phi = 90°$ and $\phi = 270°$, where the left foot and the right foot would be extended, respectively.

4.1.3 Sphere

The sphere images are taken from an experimental campaign which used tomo-PIV to study the flow in the wake of sphere. The aim of the study was to assess the feasibility and accuracy of the Ring of Fire concept, as is explained in the work of Terra et al. [3] [2]. The sphere, which had a diameter of 10 cm, was supported by a strut of 20 cm length shaped as an airfoil of 20 mm chord and 3 mm thickness. It moved through a rectangular duct of dimensions 50 cm x 50 cm and a length of 170 cm. A picture of the set up is shown in Figure 4.8.

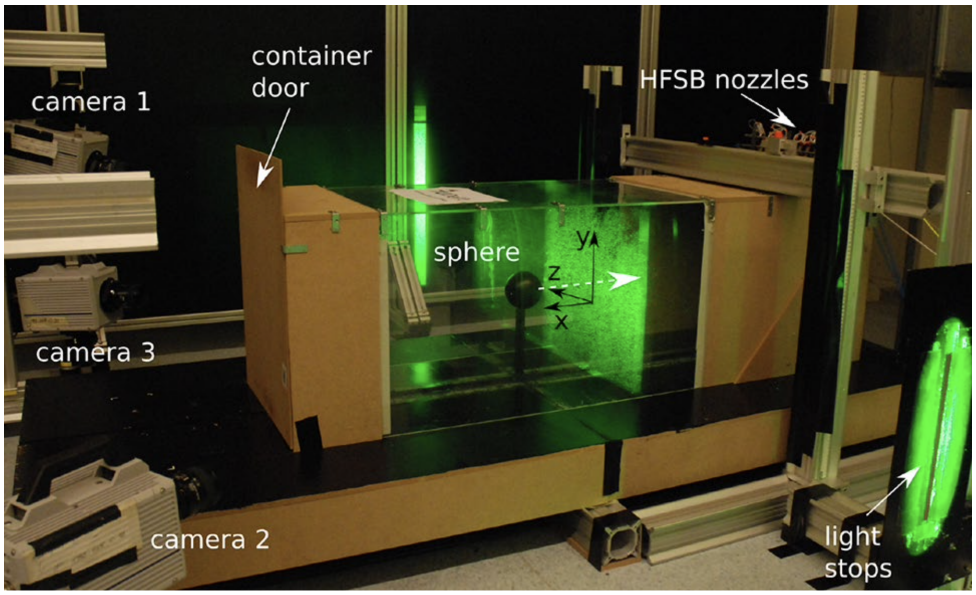

Figure 4.8: Experimental set up for the sphere, from Terra et al. [3].

Flow seeding Similarly to the other two experimental campaigns, HFSB were used as tracer particles. In this case, the seeding rake contained 10 generators, which produced 300 000 particles per second. The seeding density was of approximately 3 bubbles/cm^3.

Illumination system The same type of laser as for the skater and cyclist campaigns was used: a Quantronix Darwin Duo Nd:YLF laser. In this case, since tomo-PIV measurements were performed, the laser sheet was thicker relative to the size of the object. The measurement volume had dimensions of 3 cm x 40 cm x 40 cm.

Imaging system The three cameras used for the measurements were the same as for the other two campaigns. They were set up with Nikon 60 mm objectives, and the f-number was 8. The cameras captured the images at a frequency of 500 Hz.

The main experimental parameters for each of the three cases are summarized in Table 4.1. The experimental apparatus used for the three campaigns was mostly the same, including cameras, laser and type of seeding particles. The scale of the sphere is significantly smaller than the other two experiments, so the field of view was also more limited. Another important difference was the environmental conditions for each case. The sphere campaign was done indoors, so all measurements were performed at room temperature and the freestream is not expected to have high values of velocity. The cyclist experiments were carried out outdoors on April 2017 in the Netherlands. That week the temperature was relatively close to room temperature, and the processing needs to consider the presence of wind. The skater campaign was done on an ice skating ring, where the temperature was close to 10 °C and the ventilation system was turned off. In order to adapt to the different light conditions and measurement set ups, the f-number was different in each case. This might lead to difference in the intensity of the particle images detected. Finally, while all experiments were done using helium filles soap bubbles, the generator had a different number of nozzles for each experiments. This in combination with the dimensions of the measurement domain leads to slight differences in the density of the seeding.

Table 4.1: Summary of experimental parameters used in the three experimental campaigns.

Experiment	Skater	Cyclist	Sphere
Velocity ($m\,s^{-1}$)	12.5	8.3	1.33
Reynolds number	$5.3 \cdot 10^5$	$3.2 \cdot 10^5$	10^4
Cameras	Photron FastCAM SA1	Photron FastCAM SA1	Photron FastCAM SA1
Lenses	Nikkon 50 mm	Nikkon 50 mm	Nikkon 60 mm
Acquisition frequency (Hz)	500	2000	500
f-number	f/1.8 and f/4	f/5.6	f/8
Magnification	0.006	0.011	0.07
Digital image resolution (mm/px)	3.1	1.8	0.47
Tracer particles	HFSB	HFSB	HFSB
Number of nozzles	204	200	10
Particle imaging density (ppp)	0.005	0.09	0.04
Laser	Quantronix Darwin Duo Nd:YLF	Quantronix Darwin Duo Nd:YLF	Quantronix Darwin Duo Nd:YLF
Field of view (m)	4.4 x 2.6 x 0.05	1.8 x 1.8 x 0.03	0.4 x 0.4 x 0.03

4.2 Data Processing

As explained in chapter 3, there are several parameters that need to be selected when using the energized mass method. They will be presented in this section, together with the processing parameters chosen to obtain the PIV velocity fields that will be used to gain insight on the flow topology in chapter 5.

4.2.1 Energized mass method

The application of the energized mass method to the acquired data can be divided into preprocessing and processing. The first is done in Davis, and prepares the images so the wake can be identified. The parameters involved in it are explained in this section, followed by the processing parameters. Processing was done fully using a python script developed for this purpose, and its output is the drag area of the object.

Preprocessing

The first processing steps were the same for all three experimental cases presented above. All these steps were performed on Davis 8.4. They are listed below in the same order in which they were applied. The reasoning behind including each of them is explained in the following paragraphs.

1. Subtract average
2. Apply sliding minimum filter
3. Apply Gaussian blur
4. Correct image for the stereoscopic angle
5. Mask the image

Subtract average It is crucial to the method that the background noise is minimized, so the only sources of intensity in the images are the seeding particles. For this reason, the first step of the pre-processing was to subtract the average of all the pictures. The average was obtained from all the available frames to ensure only the fixed background noise remained. This step is also common as preprocessing in order to apply a PIV algorithm [108], and in the energized mass method it is of special importance because the results are more sensitive to background intensity than in the case of PIV.

Apply sliding minimum filter After this, the sliding minimum filter in time was applied. The sliding minimum is the method used in the energized mass method to detect the wake area. Since the main objective of the method is to obtain the drag without relying on the PIV velocity fields, the area of the wake has to be detected in an alternative way. The sliding minimum selects for each pixel the minimum value of intensity the pixel has had over a range of images. In this way, in regions where the particles move faster, the particles will be deleted from the resulting image. In all cases, the freestream was close to zero and the object was the one moving, meaning that the region of higher fluid velocity will be the wake. The filter length is essential in this step, as it is directly related to the speed of the particles that will be deleted. If the filter length is smaller, only particles with higher velocities will be removed from the result. On the other hand, if the filter length is too high, the small fluctuations in the freestream will cause enough movements in all particles, and no particles will remain on the result.

For each case, the filter length has to be determined. Following the reasoning presented in chapter 3, the filter length can be calculated as follows:

$$N = \frac{\Delta z f}{0.37U} \tag{4.1}$$

where Δz indicates the laser sheet length, f is the acquisition frequency, and U the velocity of the body. As explained in chapter 3, this equation will filter out all particles that move faster than 37% of the body velocity U in streamwise direction, so it acts as a velocity threshold. The reasoning for the 37% threshold is explained in detail in chapter 3. The sliding minimum filter length for each case was calculated using the value of the parameters listed in Table 4.1, and the results are listed in Table 4.2. Even though the equation is set up with the idea of filtering the particles based only on their streamwise velocity, the sliding minimum is not capable of distinguishing the direction of the particle movement. This means that particles that have a sufficiently large in-plane velocity will also be deleted when applying it.

Table 4.2: Summary of processing parameters used in the three experimental campaigns.

Experiment	Skater	Cyclist	Sphere
Filter length N	5	9	7
Images for average subtraction	1000	2300	300
Masked image size (px x px)	600 x 800 and 570 x 720 *	910 x 750	910 x 960
Window size (px x px)	20 x 20 and 24 x 19 *	25 x 26	30 x 30
Intensity threshold	0.005	0.01	0.08
Rolling average length	4	8	4
Distance to object (m)	0.5	0.5	0.05
* For high drag and low drag position, respectively			

Apply Gaussian blur, image correction and masking After applying the sliding minimum filter, a Gaussian blurr is applied to increase the image size of the particles and make the wake area more easily identifiable. Since the images were taken with a stereo-PIV (skater, cyclist) and tomo-PIV (sphere) set up, they need to be corrected for the angles of the camera with respect to the laser sheet. Finally, the images are masked in order to discard irrelevant parts, which helps reduce the computational cost of the image processing. In addition, the images which result from the angle correction have an irregular shape, and masking them ensures a rectangular shape. The size of the mask was determined by trial and error: observing the entire range of images, it was possible to understand how large the selected area had to be in order to ensure the wake would always be contained inside of it. Since the shape and size of the wake varied depending on the object, so did the mask size. However, for any single test case the mask always remained constant for all the runs.

Figure 4.9 shows a side by side comparison of the images before and after the pre-processing for the three experimental cases. The skater images are in the top row, cyclist images in the middle and sphere images in the bottom row. In each row, the left image is shown without any processing, directly as captured by the camera. The right image is the result of all the pre-processing steps listed and explained above.

The presence of background intensity is something that generally is avoided and minimized in PIV processing, but for the case of the energized mass the impact is higher. If any light was left on the image which was not from a tracer particle, it would directly affect the detected wake, so it has to be avoided completely. In addition, it is important for the energized mass method that the particles have a high intensity, and are distributed uniformly. For example, comparing the

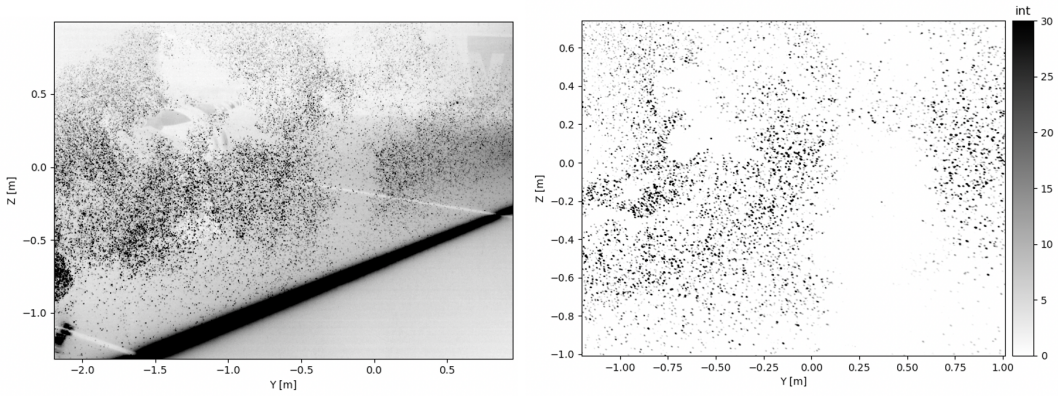

(a) Skater raw image (left) and preprocessed image (right).

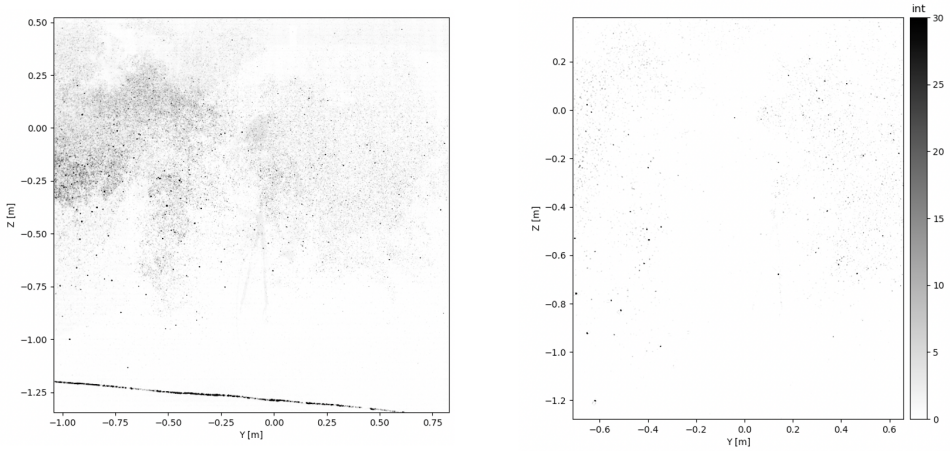

(b) Cyclist raw image (left) and preprocessed image (right).

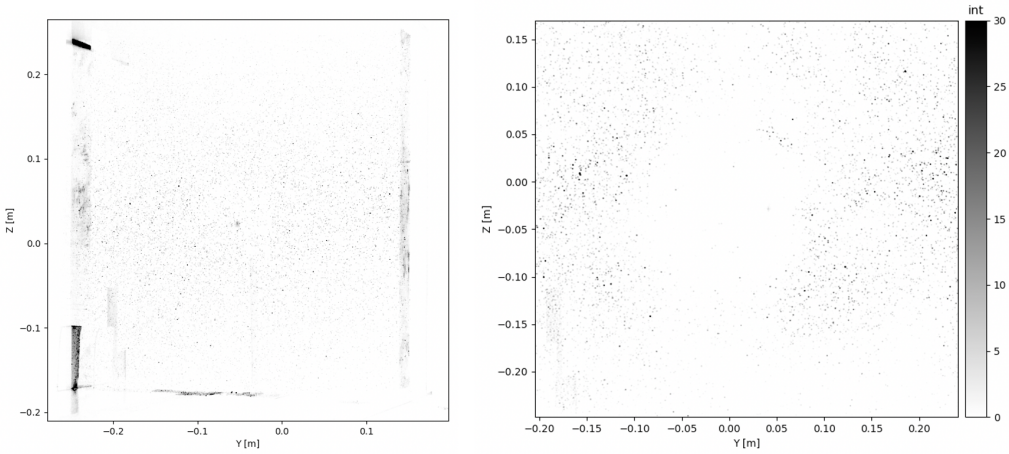

(c) Sphere raw image (left) and preprocessed image (right).

Figure 4.9: Raw images without any modification (left) and images after preprocessing with Davis 8.4 (right), of (a) skater, (b) cyclist and (c) sphere.

top and middle row in Figure 4.9, the wake of the skater (top) is much more easy to distinguish with the naked eye than the wake of the cyclist (middle).

In the case of the skater and cyclist comparison, the difference can already be clearly seen in the raw images. The skater raw image shows many more particles which also have higher

values of intensity. On the other hand, the background intensity is also higher. The reason for this difference might be related to the number particles, since more nozzles were used in the experimental campaign. In addition, the f-number was higher for the cyclist experiments, which means the cameras captured less light. The impact of this on the results is discussed in chapter 5. The preprocessed images of the sphere show an intermediate situation in terms of the clarity of the wake.

In the case of the cyclist, the high frequency meant that a larger amount of images had to be exported and used for the energized mass processing. This carries a large computational cost, so in order to mitigate it the images were sampled. Only one out of every two images was exported, effectively halving the frequency. The same thing was done for the sphere, where the frequency was reduced by 5.

Processing

After the images are pre-processed, they are exported from Davis and a Python 3.7 script is used to do the remaining steps, which are listed below. As discussed in chapter 3, there are several parameters that need to be selected during these steps. They are summarized in Table 4.2. All these steps are explained in more detail in chapter 3, and are only reviewed here briefly.

1. Divide image into windows
2. Average the intensity value of all the pixels in each window
3. Set an intensity threshold below which the windows are tagged as being part of the wake
4. Cluster the points tagged as wake and select only the largest cluster
5. Fill in any remaining points in the wake to ensure it is a solid surface

Divide image into windows Firstly, the pixels in the masked image need to be divided into windows where the intensity will be averaged. Without this step, it would not be possible to distinguish between pixels that have low intensity values because they are in the wake area and pixels that have low values because they are in between particles in the freestream area. In this way, the difference is more clear. However, this step is not enough to guarantee that the areas of low intensity are part of the wake, and are not related to uneven seeding. The effects of this are dealt with in later steps.

In general, it was found that a window size of close to 20 x 20 pixels was optimal for both the skater and the cyclist. This size represented a good compromise between the computational time and the resolution required for the wake shape. In addition, smaller window sizes can cause more irregular edges in the detected wake, as shown in the sensitivity analysis in chapter 3. The window size in each case was also limited by the size of the masked image, as it was always selected to be a number by which the total amount of pixels in the masked image was divisible.

Intensity threshold The window image and intensity threshold need to be selected together. Their value depends on the seeding density: if there are more particles, the intensity threshold can be set to a higher value, even if the intensity values are normalized when they are loaded into the python script. The intensity of the particle images is also an important factor, and it can vary for each experiment depending on the amount of background light that was caught by the cameras. For these reasons, the threshold varied between experimental cases, and even between runs of the same experimental case. In all cases, the value for the threshold had to be chosen by trial and error. The final drag value was not checked, but the final detected wake was

compared with the pre-processed image, and the threshold that achieved a better match was selected.

In the case of the skater in the high drag position, the window size was exactly 20 x 20 pixels. In the case of the low drag skater, the intensity window size was 24 x 19 pixels. The masked images were of different sizes because the shapes of the wakes were different, as will be explained in chapter 5. The window sizes were always chosen to be such that the total amount of pixels in the masked image was divisible by the window size. This way, different masked image dimensions led to different intensity window sizes. The value of the threshold varied: for the first runs that were performed in the campaign, the optimal value was found to be close to 0.005 counts. The value of the threshold was selected arbitrarily based on visual inspection. As shown in Figure 4.10, in the last two runs the seeding was increased significantly, so the threshold had to be raised to 0.9 counts. The increase in seeding was caused by the fact that the feeding system had never been operated at the low temperatures of the skating ring, so its realiability to provide constant, uniform seeding was not as high as usual.

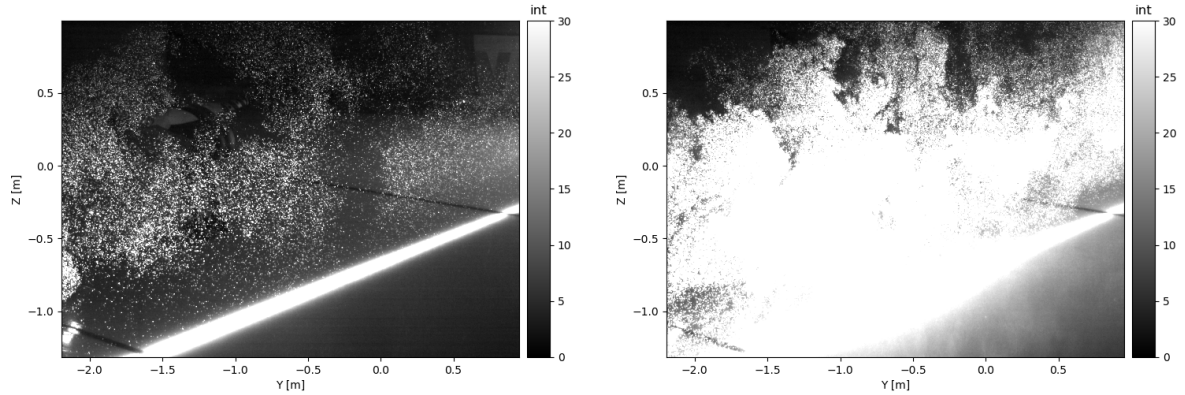

(a) Raw image from run 86.

(b) Raw image from run 94.

Figure 4.10: Comparison between a run with average amount of HFSB (left) and higher than average amount of HFSB (right).

In the case of the cyclist, the window size was chosen to be 25 x 26 pixels. Since the wake of the cyclist in time trial position and upright position is similar, the same mask was used for images of both positions, and thus the window size was also kept constant. The value for the threshold in for cases was selected to be close 0.01 in all runs. Finally, since the sphere is expected to have a wake with a simpler shape, the window size could be slightly larger, with dimensions 30 x 30 pixels. The optimal threshold was found to be 0.08 counts for all runs.

Clustering The next step is crucial in order to avoid all the possible errors that can be caused by irregular flow seeding in the experimental set up. As explained in section 4.1, some time was waited between runs in order to ensure that the previous run would not affect the flow, and that there were enough tracer particles in the measurement domain. However, it was not possible to ensure the flow would be perfectly uniform. This causes areas where the amount of seeding particles is lower already in the raw image. Since the region is in the freestream, the distribution of the particles is conserved through the application of the sliding minimum filter. This causes a region of low particle density in the pre-processed image that is not related to the wake.

A clear example of such an issue can be seen in Figure 4.9 (a). The raw skater image shows a region on the top left corner where the seeding is uneven. Even though it is clearly unrelated to the wake of the skater, it is still visible in the pre-processed image shown in the right. This exact same region is detected in Figure 4.11, where it appears first as lower average intensity windows, and as detected wake on the image on the right.

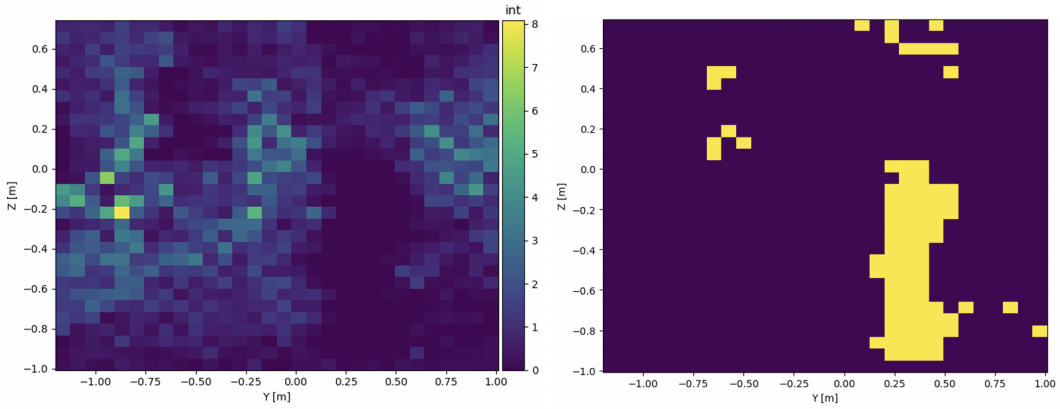

(a) Skater intensity windows (left) and detected wake before clustering (right).

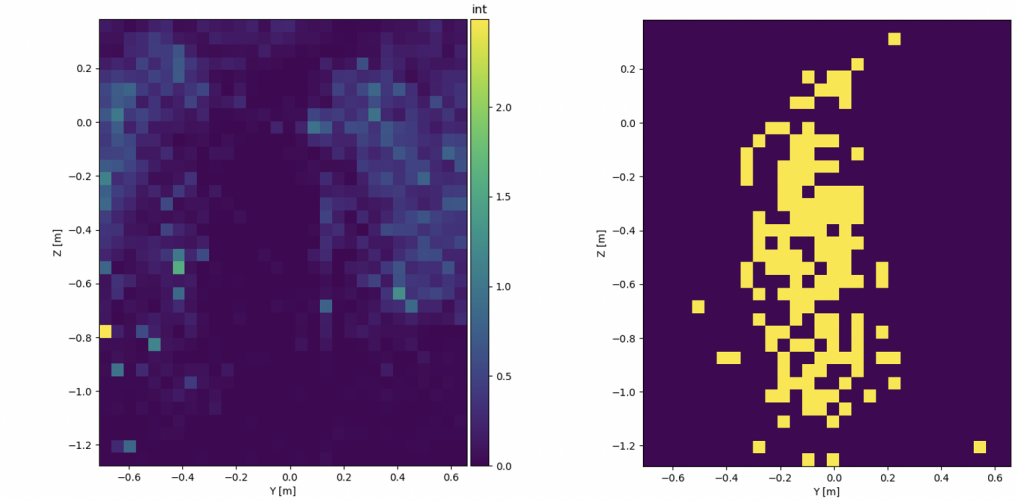

(b) Cyclist intensity windows (left) and detected wake before clustering (right).

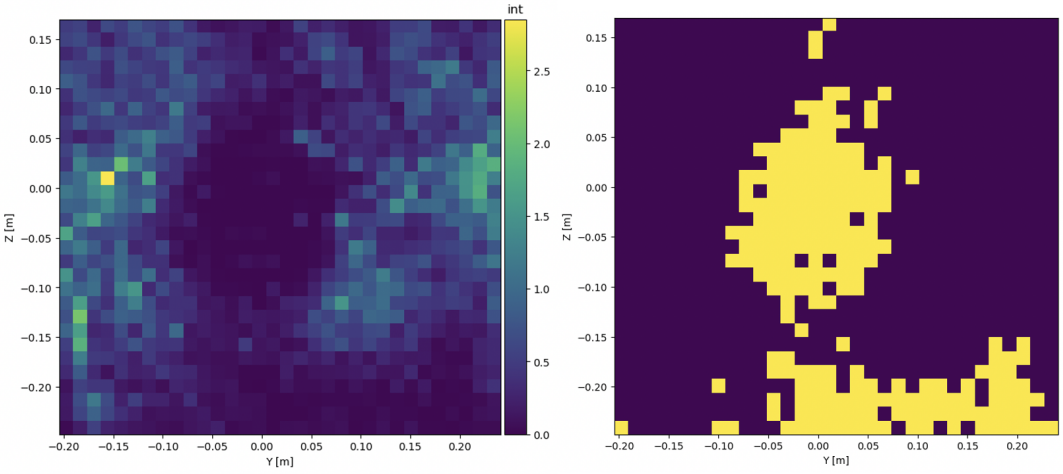

(c) Sphere intensity windows (left) and detected wake before clustering (right).

Figure 4.11: Images divided into windows with average intensity (left) and wake detected by applying a threshold with no clustering (right), of (a) skater, (b) cyclist and (c) sphere.

Any such regions where the seeding is less dense compared to the rest of the field of view are likely to have a lower average intensity than the threshold when the image is divided into intensity

windows, so they will be identified as wake. In order to avoid this, the DBSCAN clustering algorithm is used, and only the largest cluster is kept as wake. The exact way in which the algorithm works is explained in detail in chapter 3. The only two parameters that need to be specified for this algorithm are the maximum distance (eps) and the minimum number of samples. The eps refers to the maximum distance between two points that are considered to belong to the same cluster, while the minimum number of samples indicates how many other points need to be close enough to a point, in order for the point to be considered a core point. The minimum number of samples was kept at the default value of 5, while the eps was set to 1.5 windows. When the points were passed to the algorithm, their coordinates were transformed so that the distance between one point and its neighbour would be of 1. In this way, an eps of 1.5 would mean that points that are directly next to each other or diagonally adjacent would be considered part of the same cluster.

Fill in remaning points Finally, the last part of the image processing consisted of filling in any points inside the wake that were not already tagged as wake. Very small regions of high intensity inside the wake area were observed to be caused mainly by reflections or by single particles that were not removed with the sliding minimum. Clear examples of this issue are shown in Figure 4.11 (top and middle rows). The contours of the cluster were identified, and all points contained inside of it were tagged as wake. For this step, there were no parameters to select and in all experimental cases the procedure was the same.

Once all images were processed, the area in each of them was measured and plotted against the distance from the object. A rolling average was applied in order to reduce the sensibility of the method to small differences from frame to frame. The value of the kernel for the rolling average in each experimental case is shown in Table 4.2.

In the last step, the drag is calculated by applying a linear fit through the measured area vs. distance from the object plot, and backpropagating it to the position of the object. The exact point to which it was extrapolated had to be decided for each case, and is presented in Table 4.2. In all cases, the first frame can only be taken once the entire body has passed through the laser sheet. Any earlier frames include reflections, and the helium filled soap bubbles in the area are not detectable. Therefore, the distance between the first used frame and the point where the drag area needs to be determined. It was taken to be 0.5 m for the skater because of its body position, which is leaning forward. In the case of the cyclist, the distance was taken to be 0.5 m, based on the estimated diameter of the wheels and the cyclist position. For the case of the sphere, the distance was taken to be the radius length, since the centre of the sphere is the cross-section of highest area.

4.2.2 PIV velocity fields

For each experimental case, the wake topology is discussed in chapter 5. This is done to gain some insight on the wake and be able to understand better if the wake detected with the energized mass method is accurate and realistic. The velocity fields were obtained with PIV, and in this section the parameters used to obtain them will be explained. The skater velocity fields were obtained for the purpose of this thesis, however the cyclist and sphere velocity fields were already available from the work of Spoelstra et al. [4] and Terra et al. [3], respectively.

The PIV fields were obtained with stereo-PIV in the case of the skater and cyclist, and tomo-PIV in the case of the sphere. In each case, a short explanation of the PIV processing is presented below. A summary of the main parameters is provided in Table 4.3.

Skater For the skater, the only pre-processing required was the reduction of background intensity. For this, the average intensity over the entire time series of images was subtracted

from each frame. The algorithm used was stereo correlation. Three iterations were done with window sized of 64 x 64 pixels, and two iterations for window sizes of 32 x 32 pixels. For all iterations, the windows were round and an overlap factor of 75% was used. Post-processing included Whittaker image interpolation for the final passes and linear vector interpolation of any remaining empty spaces.

Cyclist For the case of the cyclist, pre-processing included removing background intensity by subtracting the minimum value of intensity of each pixel over the entire range of images. The PIV fields were obtained using a sliding sum-of-correlation algorithm in time, over a kernel of seven pairs of frames. Spoesltra et al. [20] used 64 x 64 pixel windows, again with an overlap factor of 75% and a round shape. Regarding interrogation window sizes, Spoelstra et al. [20] concluded that the dimensions should be between $0.05c$ and $0.25c$. Larger intensity windows might be subject to modulation errors and loss of information about the small scale structures, while smaller windows might suffer from random errors. The post-processing was the same as in the case of the skater, with the added feature of applying the universal outlier detection filter [109].

Sphere The sphere data was processed in a different way, as tomo-PIV was used. In this case, the pre-processing included background intensity reduction as well as Gaussian smoothing. The algorithm used was the sequential MTE-MART (SMTE) [3] [110]. Because of the tomographic algorithm, the windows were three dimensional, with a size of 32 x 32 x 32 voxels. The selected overlap factor was once again 75%.

4.2.3 Output flow and force parameters

The results are presented in chapter 5 and include a discussion on the velocity fields obtained with PIV. In these explanations, some quantities are presented as non-dimensional in order to aid the interpretation of the results. This section is focused on the definition of these non-dimensional quantities.

In this work, the drag results will be presented in terms of the drag area, which is defined as follows:

$$c_D A = \frac{D}{\frac{1}{2}\rho U^2} \tag{4.2}$$

where D is the drag force, ρ the fluid density and U the object velocity. The drag area is a commonly used quantity in cycling, because the area of a cyclist can be complicated to obtain and inaccurate [103] [111]. Since obtaining the area of the skater would present the same difficulties, it will also be used in the discussions about it. The frontal area of a sphere is much easier to calculate, but for consistency those results will also be presented in terms of $c_D A$.

For the analysis of the velocity fields in the wake of the different experimental cases, the wake velocities will be normalized in the following way:

$$u^* = \frac{u_w - u_{env} + U}{U} \tag{4.3}$$

Where u_w is the velocity field in the wake, u_{env} is the environment velocity prior to the passage of the model, and U is the velocity of the object. In this way, the freestream flow which is unaffected by the wake will have a velocity of $u^* = 1$, and the wake will have velocities lower than that. This is done following Terra et al. [2] and Spoelstra et al. [4].

Table 4.3: Summary of PIV processing parameters used in the three experimental campaigns.

Experiment	Skater	Cyclist	Sphere
Correlation algorithm	Stereo correlation	Stereo sliding sum-of-correlation	MTE-MART
Interrogation window	32 x 32 px (100 x 100 mm^2)	64 x 64 px (116 x 116 mm^2)	32 x 32 x 32 vx (10 x 10 x 10 mm^3)
Overlap factor	75 %	75 %	75 %

Finally, the vorticity is also presented in non-dimensional form, using the following equation:

$$\omega^* = \frac{\omega c}{U} \tag{4.4}$$

where ω is the vorticity, and c is the model's characteristic length. In the case of the sphere, c is taken to be equal to the diameter of 10 cm, while in the case of the skater and the cyclist the torso length is used, which is estimated to be 60 cm [4]. In general, presenting the results in non-dimensional form makes it easy to compare the results with literature.

Chapter 5

Results

This chapter is focused on the results obtained for the drag of the bodies described in chapter 4, using the method presented in chapter 3. The bodies consist of a skater, a cyclist and a sphere. The skater was analysed in two different positions, for which a dedicated experimental campaign was performed. Two positions, upright and time-trial, were also examined in the case of the cyclist. For this case and for the sphere the data was already available [4] [2]. For each of them, firstly the wake topology is described using velocity and vorticity fields obtained with PIV. This is followed by an explanation of the results obtained with the energized mass method, including the calculation of the drag.

5.1 Skater

This section is focused on the results obtained for the skater experimental campaign. Two skater positions were tested: high drag and low drag. The low drag position is closer to the conventional speed skating position, with both arms behind the back and the torso lowered, while the arms were stretched to the side in the high drag position. Both of them are included in the discussions in this section. In subsection 5.1.1 the wake topology is studied using PIV velocity fields, while the energized mass results are discussed in subsection 5.1.2.

5.1.1 Wake topology

The aerodynamics of speed skaters have been the subject of some studies. Most of them were focused on specific aspects, like the separation point in specific parts of the body or the effect of the skater position on the drag area [112] [113] [114]. There are no available velocity or vorticity contours of the wake of a skater in literature. For this reason, they have been processed using stereo-PIV and they will be included in this section. In addition, examining the topology of the wake using PIV velocity fields might give some insight on the performance of the energized mass method in identifying the wake area. It is important to keep in mind that the high drag position is not a realistic representation of a high speed skater in a competition.

Velocity fields

The ensemble averaged streamwise velocity fields, together with vectors indicating the in-plane velocity field, are shown in Figure 5.1. The low drag position is shown on the left, and the high drag position is on the right. The velocity fields are ensemble averaged over several runs, 5 for the low drag and 6 for the high drag. Some runs had to be eliminated because of bad seeding. Since PIV is a more robust method than the energized mass, it was possible to use more runs when analyzing the wake topology.

At a distance of half a meter from the skater, the maximum velocity deficit in the wake is around 45% of the freestream velocity. In both cases, this is found in the wake region created by the lower body of the skater. For the two positions, the legs were positioned in a similar way: the knees were flexed, and the feet were roughly in line with the hips of the skater. The skater glided through the measurement domain, so the legs did not move. The upper half of the body is in

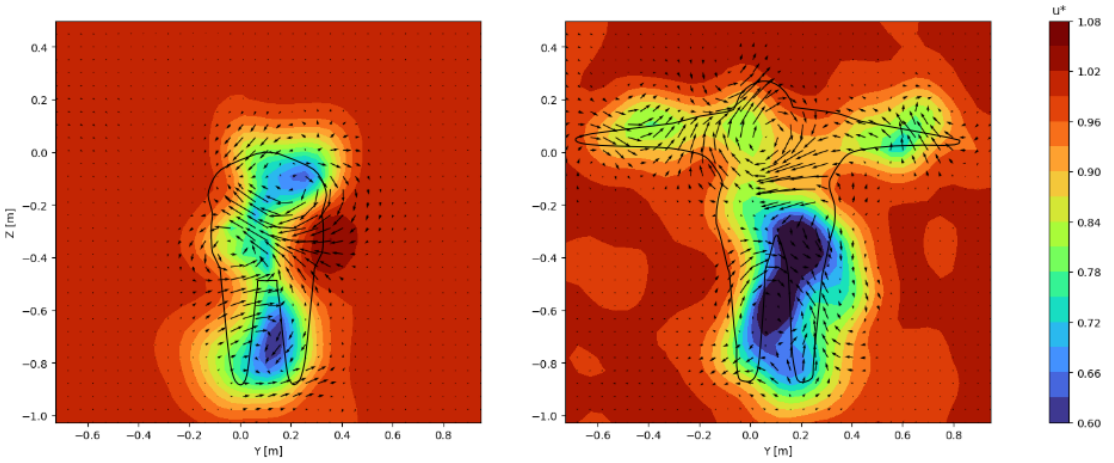

Figure 5.1: Ensemble averaged velocity fields of the wake of a skater in low drag position (left) and high drag position (right) at $x = 0.5\,\mathrm{m}$. The silhouette of the skater (black solid line) is superimposed for clarity.

different positions, which is reflected on the velocity contours. The low velocity regions created by the extended arms can be clearly seen in the picture on the right. For the case of the low drag configuration, both arms are held close to the back of the cyclist. Even though the torso angle is smaller for the low drag skater, the velocity deficit region caused by it is distinguishable from the one caused by the legs and lower body. The difference in torso angle, combined with the effect of the extended arms in the high drag position, cause the drag of the low drag position skater to be shorter in height. In addition, the region of maximum velocity deficit is larger for the high drag position skater, and located in a higher position in the wake.

Vorticity

The vorticity contours for the same location are shown in Figure 5.2 for both positions, with the low drag shown on the left and the high drag on the right. The ensemble averaged in-plane velocity fields are shown as grey vector fields. In addition, the main vortices are labeled in the images. These vorticity fields are ensemble averaged over the same runs as in Figure 5.1.

In both cases shown in Figure 5.2, the main vortices seem to be shed by the hips and thighs, based on their location. Since both positions are symmetrical, the wake is also expected to be symmetrical on a vertical axis. In addition, since the skaters were not moving their legs from a few meters before passing through the laser sheet and until several meters after the laser sheet, unsteady flow in the legs region should not have a major effect on the wake.

In the low drag position, the arms of the skater are attached to the body, with the hands held together at the lower back. The air that flows through the back cannot remain attached all the way to the hips, and likely separates at the location of the hands, shedding the vortices found in Figure 5.2. This might explain why the location of these vortices is slightly higher than the location of the hip vortices in the high drag position, even though the knee angle is the same for both. For the low drag position, these vortices are the most intense ones, and are expected to dominate the behavior of the far wake. Even though the vortices shed from the thighs were expected to be symmetrical, it seems that the vortices shed from the right leg are more intense than those shed from the left leg. The opposite happens with vortices originating in the lower half of the legs, calves and ankles.

In the high drag position, the hands are extended horizontally to the sides of the body of the skater. For this reason, the flow is able to remain attached through the back until it reaches

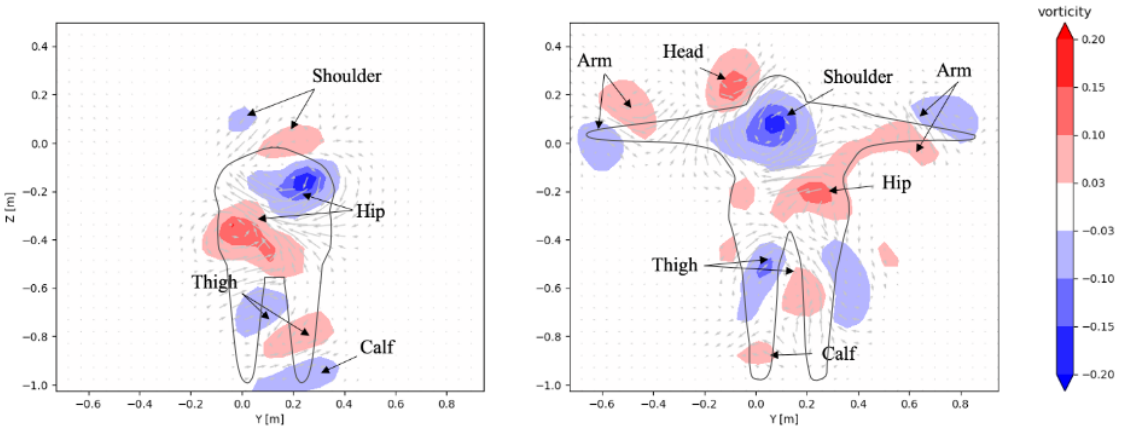

Figure 5.2: Ensemble averaged non-dimensional vorticity of the wake of a skater in low drag position (left) and high drag position (right) at $x = 0.5\,\mathrm{m}$. The silhouette of the skater (black solid line) is superimposed for clarity.

the hips, from where vortices are shed. Similarly to the case of cyclists, the hip vortices are the strongest ones. There are additional vortices shed by the arms and the shoulders, which create flow towards the body, and might contribute to a higher rate of entrainment. In the upper region of the wake, some vorticity might also be attributed to the head of the skater, which in the higher drag position is positioned higher than in the low drag position. In the lower half of the wake, there are vortices shed by the thighs, ankles and calves of the skater.

Figure 5.2 and Figure 5.1 also show that the vorticity shed by the lower body has opposite signs of rotation for the two positions. At a height of $z = -0.2\,\mathrm{m}$, the low drag skater experiences some upwash, while in the same location behind the high drag skater there is downwash. For other similar bodies, like the one of a cyclist (explained in section 5.2), downwash has been observed behind the back of the person. The reason for the upwash present in the low drag position might be the hands held together at the lower back, which interact with the flow coming from the back.

Wake development

The time evolution of the wake velocities is depicted in Figure 5.3, which shows the wake of the skater in both positions at distances of 1 m, 3.25 m and 5.5 m from his back. All images show the ensemble averaged velocity fields using the same runs as in Figure 5.1 and Figure 5.2. The in-plane velocity fields are once again shown as black vector fields in each image. The field of view in the images has been cropped so that the wake could be more clearly seen.

For both cases, the velocity deficit is still significant after a distance of 5 m, with some small areas of low velocity fluid having a deficit of 25% with respect to the freestream. The wake of the low drag position expands more in vertical than in horizontal direction. In the near wake, two low velocity regions are observed, corresponding to the feet and the upper body of the skater. They were also captured in Figure 5.1. As the distance to the skater increases, the top one moves upwards while the velocity recovers. At a distance of 5.5 m, the wake reaches a total height of 1.4 m, which is 20 cm larger than at a location of $x = 1\,\mathrm{m}$. This might be explained by the upwash in this area, which is visible through the vector field showing the in-plane velocity field. This upwash is caused by the hip vortices detected in Figure 5.2. The lower region of the wake remains in place and expands horizontally, limited by the presence of the floor.

In the high drag position, the hip vortices rotate in the opposite direction, so the upper region of the wake experiences downwash. As a consequence, the main region of velocity deficit moves

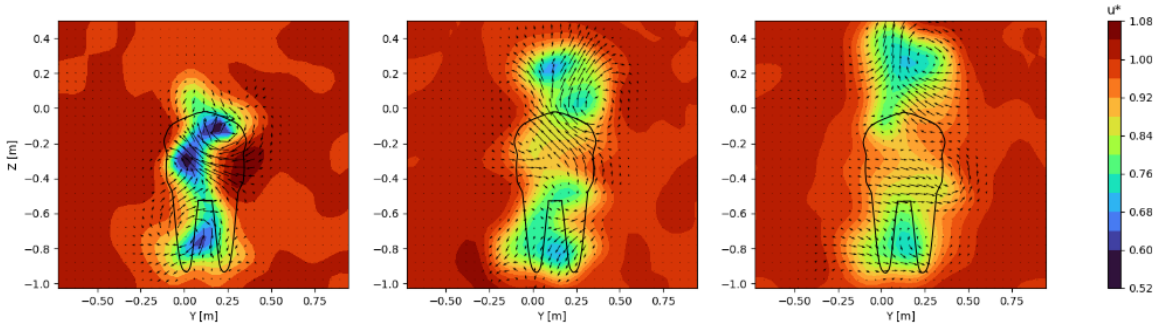

(a) Low drag position.

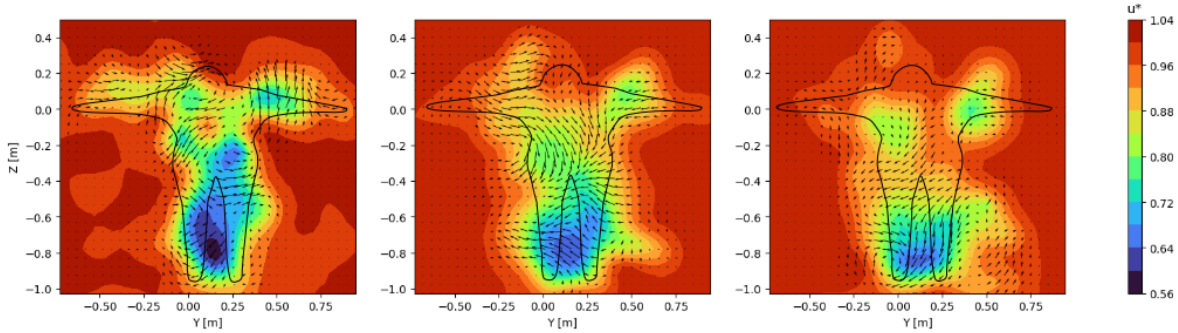

(b) High drag position.

Figure 5.3: Ensemble averaged velocity fields of the wake of a skater in (a) low drag position and (b) high drag position. The velocity fields are at a distance of 1 m (left), 3.25 m (middle) and 5.5 m (right) from the skater. The silhouette of the skater (black solid line) is superimposed for clarity.

down, and because it is limited by the floor, it also widens at the bottom. At a distance of 5.5 m, it reaches a width of 1 m. The wake of the two extended arms is clearly distinguishable in the near wake. This part of the wake experiences some upwash and inwash due to the vortices generated by the arms and the shoulders. As a consequence, the wake of the arms narrows and moves closer to the one of the main body. However, the upwash causes these two regions to extend vertically and remain roughly in the same position.

5.1.2 Energized mass method

This section is dedicated to the results obtained with the energized mass method. It is divided into two subsections, one for each skater position. First, intermediate results are presented which support some discussion about the method, followed by the drag obtained in each case.

Low drag position

Images of several processing steps of one of the the low drag position runs are presented in Figure 5.4, at a distance of $x = 0.75\,\mathrm{m}$ and $x = 1.7\,\mathrm{m}$ from the back of the skater.

The middle image shows the raw images as they were input into the python script. Preprocessing has been applied to these images, including the sliding minimum filter, background intensity subtraction and correction for the stereoscopic angle. A more detailed explanation of the preprocessing steps is provided in chapter 4. For both locations, the wake appears as a darker area in the image on the right half. Figure 5.4 shows that the seeding was

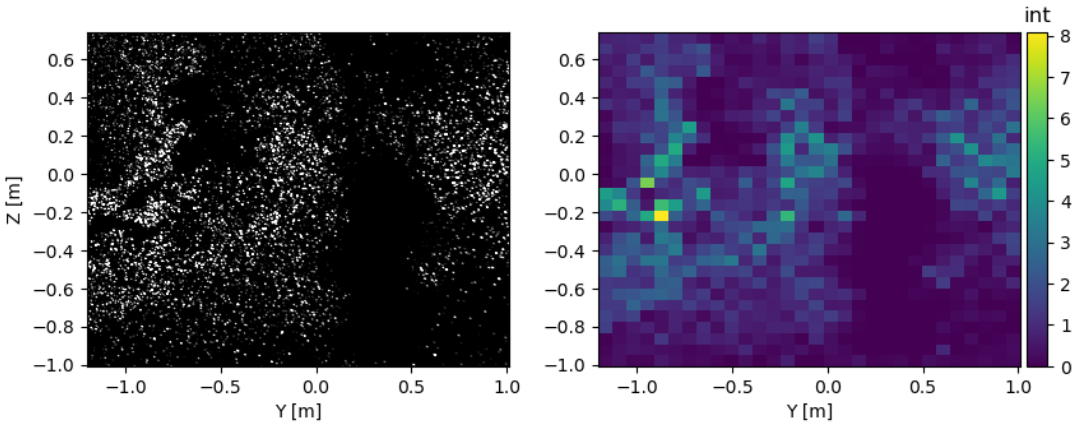

(a) Location $x = 0.75\,\mathrm{m}$.

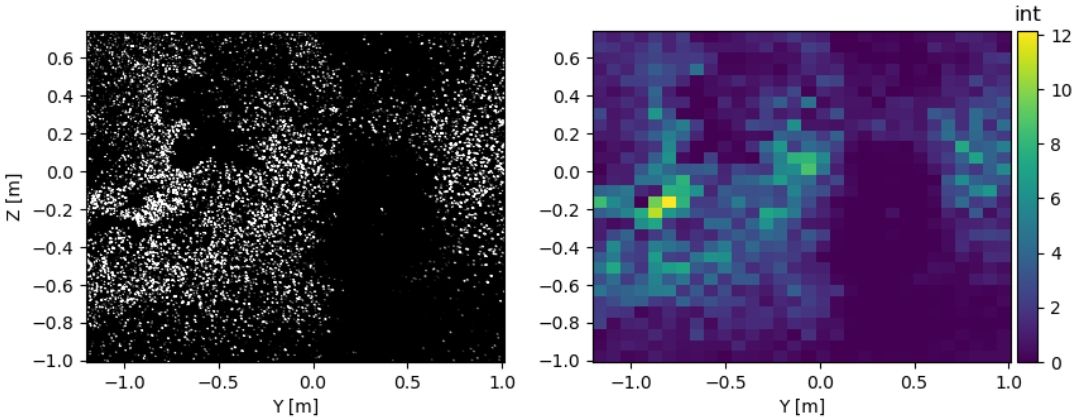

(b) Location $x = 1.7\,\mathrm{m}$.

Figure 5.4: Preprocessed image (left) and image after dividing it into intensity average windows, at a distance of (a) $x = 0.75\,\mathrm{m}$ and (b) $x = 1.7\,\mathrm{m}$ from the back of the low drag position skater.

not perfectly uniform, which leads to some other darker regions unrelated to the wake. A clear example is seen directly above the wake, and on the top left quadrant in both images.

The images on the right in Figure 5.4 show the intensity windows. They are the result of dividing the preprocessed images into windows where the intensity is averaged. As explained in chapter 4, the size of the windows used for the skater in low drag position is of 24 x 19 pixels. The size is not perfectly square because the window size for each dimension was chosen to be divisible by the total amount of pixels in that dimension. For both distances, the wake is already distinguishable as a lower intensity area at the right half of the image. The intensity everywhere else is roughly uniform, with the exception of some small areas on the left half of the image. This corresponds to an area of denser seeding which can be seen in the raw images.

Some of the remaining processing steps are pictured in Figure 5.5, for the same locations as Figure 5.4. After applying the threshold explained in chapter 4, the points tagged as wake are all the ones present in the left images, which show the results of the clustering algorithm. The small black points are tagged as noise and discarded, while all the red dots are considered to be part of the wake. The dots with a bigger size are considered to be core points by the DBSCAN algorithm.

The difference in size between the two wakes is noticeable in the cluster images in Figure 5.5, with the wake at $x = 1.7\,\mathrm{m}$ being wider both behind the feet and calf area, and the upper body one. In this image, it is also clear that there is a hole inside the wake at $x = 1.7\,\mathrm{m}$. Because this would be unphysical, this area is filled in.

The final wake is depicted by a red contour on the images on the right in Figure 5.5, superimposed

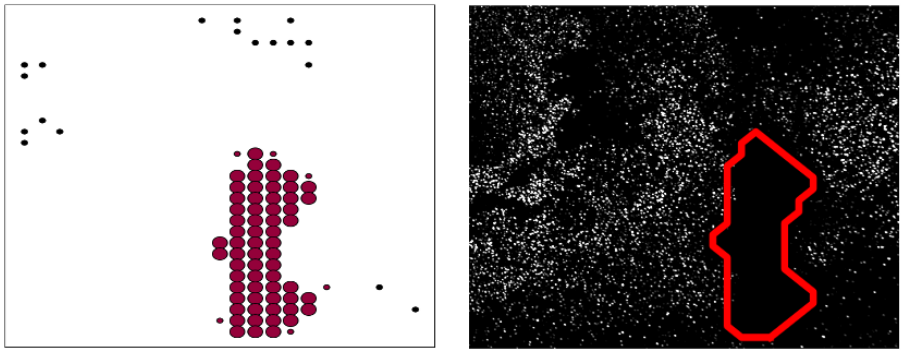

(a) Location $x = 0.75\,\mathrm{m}$.

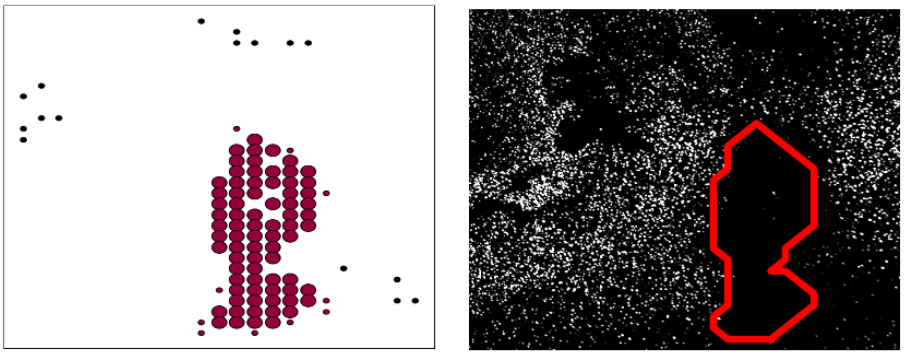

(b) Location $x = 1.7\,\mathrm{m}$.

Figure 5.5: Clustering results (left), and energized mass wake (right) for locations of $x = 0.75\,\mathrm{m}$ and $x = 1.7\,\mathrm{m}$ behind the low drag position skater. All dots that have the same color belong to the same cluster, while smaller black dots represent noise.

to the preprocessed images. This format of the plot is useful to understand if the processing steps are able to identify the region with no particles as the wake. In both locations, the results are good. The presence of a few outlier particles inside the wake is overcome and ignored. In addition, the low seeding areas outside of the wake are successfully identified as noise. In both cases, some particles are included in the wake on the left side, which is a result of dividing the image into intensity windows.

Figure 5.6 is another useful plot to examine the ability of the energized mass method to properly detect the wake. Here, the contour of the energized mass wake is superimposed to the instantaneous streamwise velocity fields at $x = 0.75\,\mathrm{m}$ and $x = 1.7\,\mathrm{m}$. This makes it possible to validate the energized mass results against the PIV velocity fields, which are more reliable. The height of the wake is well captured in both cases. The width appears to raise more issues. For the left image, the width of the two low velocity regions matches the width of the energized mass wake well. However, the in-between middle region is thinner in the velocity fields. The wake farther away from the skater is shown on the right. In this case, the general broadening is in line with the velocity fields. However, the wake has a larger width when looking at the velocity fields, especially close to the center of the wake at $z = 0.4\,\mathrm{m}$.

The detected wake area using the energized mass method was calculated for each point in the wake. The obtained area curve with respect to the position from the skater is shown in Figure 5.7. The solid curve represents the average of the available runs, with the shaded area indicating the standard deviation of the measurements. The reference value in this case was obtained applying the momentum balance method on the PIV data, following the methodology of Terra et al. [2] and Spoelstra et al.[4]. It is indicated as a horizontal red line. The calculated linear trend is shown as a dashed line, and the value of its extrapolation at the location of the

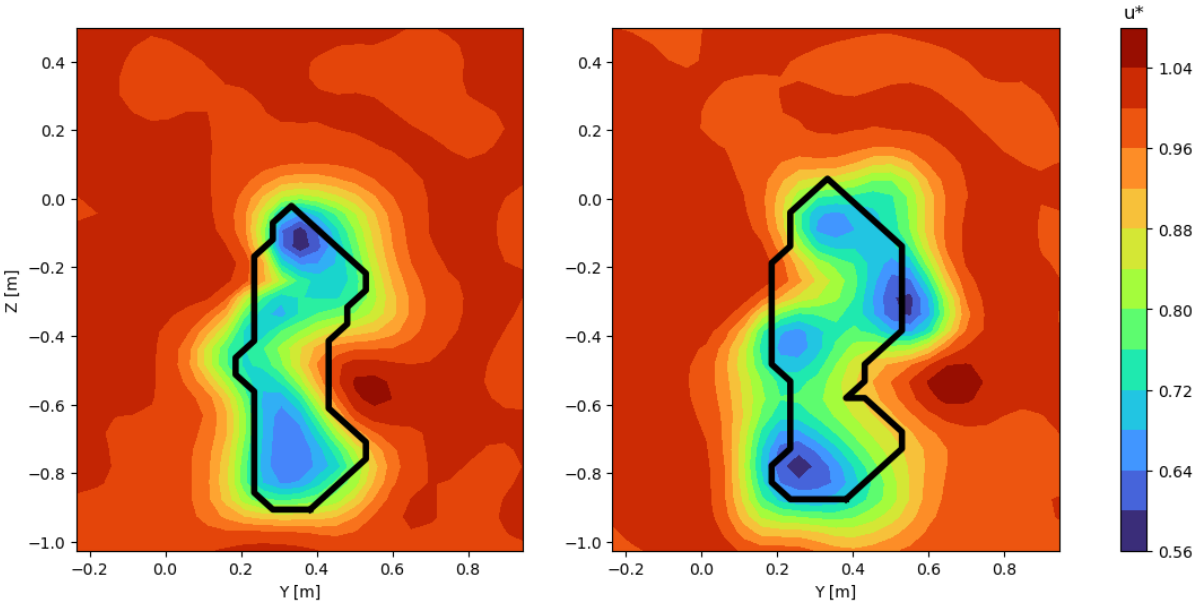

Figure 5.6: Instantaneous streamwise velocity fields and energized mass wake area for locations $x = 0.75\,\mathrm{m}$ and $x = 1.7\,\mathrm{m}$ behind the low drag position skater.

cyclist is shown as a single dot.

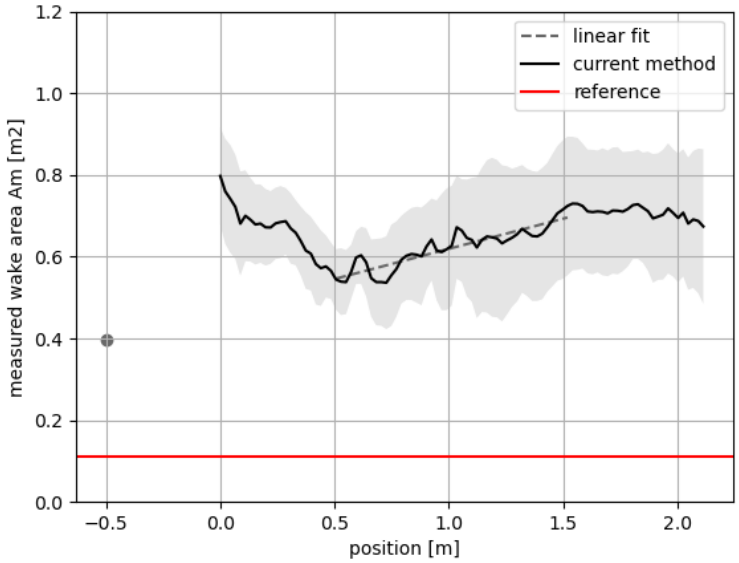

Figure 5.7: Measured wake area change with distance to the back of the low drag position skater (black solid line) and uncertainty of the values (shaded gray). The linear fit (gray dashed line) is extrapolated to the location of the skater (gray dot). Reference $c_D A$ value shown in red.

Figure 5.7 shows that for the first 0.5 m, the wake area decreases in time. This is non-physical, since the wake of a bluff body is expected to expand in time (e.g. [115] and in particular for the case of the skater it is shown in Figure 5.3a), so these frames are ignored for the calculation of the drag area. Doing this, the average results in a $c_D A = 0.39\,\mathrm{m}^2$, while the momentum balance method outputs a drag area of $c_D A = 0.11\,\mathrm{m}^2$. Drag area values of around $c_D A = 0.15\,\mathrm{m}^2$ were reported for a static mannequin at similar velocities. The higher drag was probably caused by the sidepush position of the mannequin [112]. A similar value was found using a power balance method on skaters over a 400 meter lap [116], and drag areas closer to $c_D A = 0.2\,\mathrm{m}^2$ were

observed for male skaters in a wind tunnel [114].

High drag position

This subsection is focused on the application of the energized mass method to the high drag position skater data. Two intermediate steps of the process to obtain the drag area are shown in Figure 5.8, for two different locations in the wake of the skater, $x = 0.5\,\mathrm{m}$ in Figure 5.8 (a) and $x = 1.5\,\mathrm{m}$ in Figure 5.8 (b).

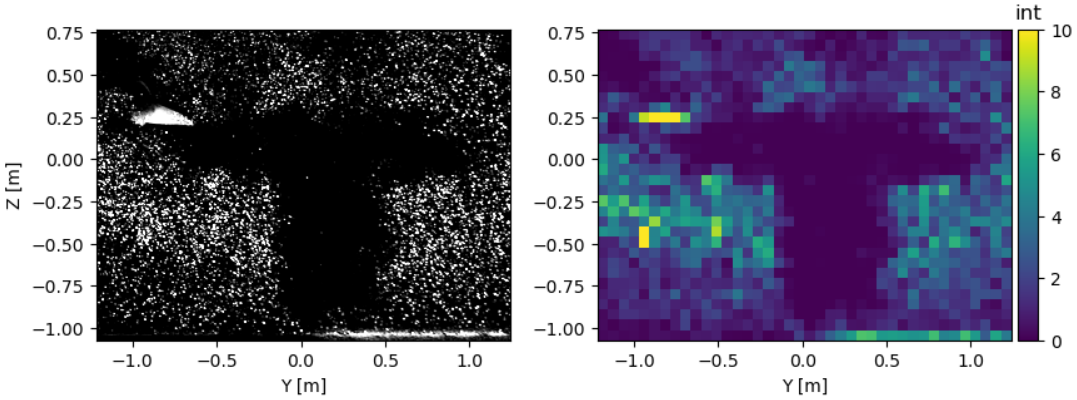

(a) Distance of $x = 0.5\,\mathrm{m}$.

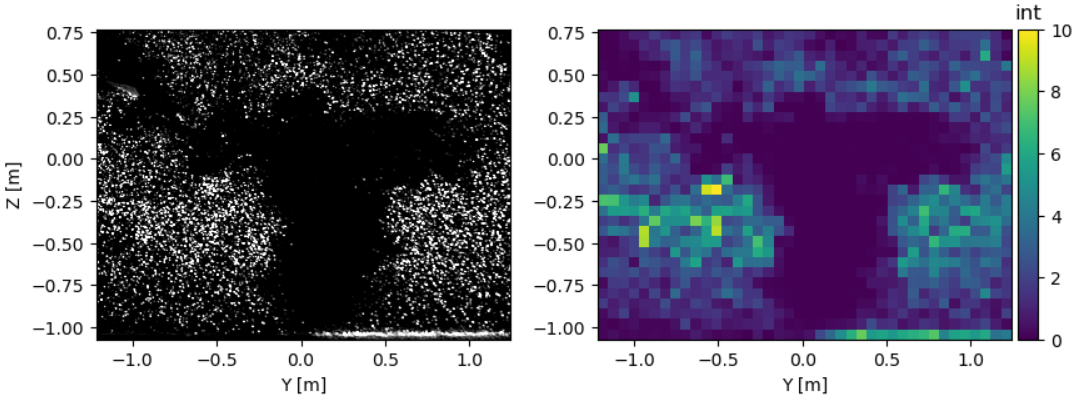

(b) Distance of $x = 1.5\,\mathrm{m}$.

Figure 5.8: Preprocessed image (left) and image after dividing it into intensity average windows, at a distance of (a) $x = 0.5\,\mathrm{m}$ and (b) $x = 1.5\,\mathrm{m}$ from the back of the high drag position skater.

The images on the left in Figure 5.8 are the preprocessed images. As explained in chapter 4, the preprocessing steps were performed in Davis and included background subtraction and the application of the sliding minimum filter, amongst others. Thanks to good seeding and low background intensity, the wake can be clearly distinguished at both distances as a region without particles. In the image at $x = 0.5\,\mathrm{m}$ (top), it is also possible to distinguish a high intensity area on the top left corner. This was caused by reflections of the laser on the suit of the skater.

The images on the right in Figure 5.8 show the result of dividing the images on the left into 20 x 20 pixel windows and averaging the intensity inside each window. For both locations, the wake is clearly visible against the higher intensity background windows. These images also show that the seeding was adequate for the application of the energized mass method, as there is a clear difference in intensity between the wake region and the outside parts. In addition, there is only one small area in the top right corner where the seeding is less dense.

The last processing steps are depicted in Figure 5.9. The left images show the result of the DBSCAN clustering algorithm, applied to all windows in which the intensity is higher than the

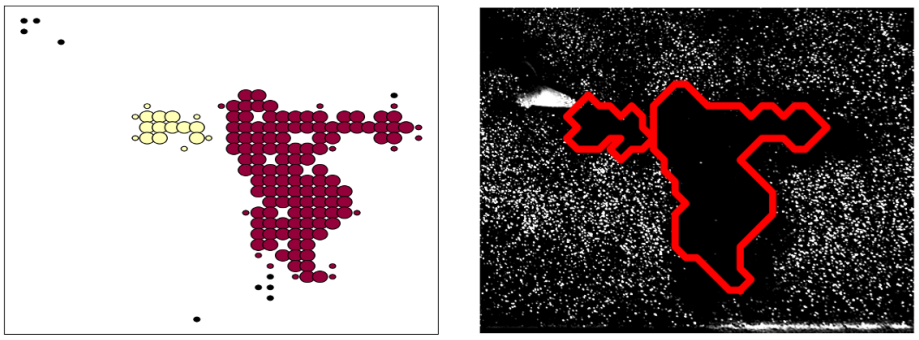

(a) $x = 0.5\,\mathrm{m}$.

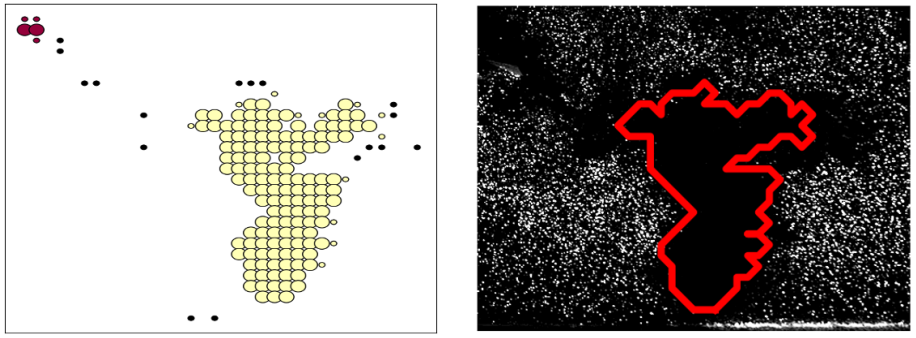

(b) $x = 1.5\,\mathrm{m}$.

Figure 5.9: Clustering results (left), and energized mass wake (right) for locations of $x = 0.5\,\mathrm{m}$ and $x = 1.5\,\mathrm{m}$ behind the high drag position skater. All dots that have the same color belong to the same cluster, while smaller black dots represent noise.

threshold explained in chapter 4. For the frame taken at $x = 0.5\,\mathrm{m}$ (top), the wake of the left arm appears to be detected as a separate cluster from the rest of the wake. However, as explained in chapter 3 part of the clustering process is comparing with the results of the previous frame to check for cases like this. Thanks to this step, the wake of the left arm is successfully identified as part of the wake on the picture in the right of Figure 5.9 (a).

For the distance of $x = 0.5\,\mathrm{m}$ (bottom), it can be seen that aside from the black dots representing noise than in Figure 5.5, there is another identified clusters in the top left corner. This is the result of uneven seeding in the raw images: the smaller cluster corresponds to the region in the top left corner that was observed to have lower seeding in Figure 5.8. Only the points belonging to the largest cluster, which is shown in yellow, are considered to be part of the wake.

The wake is depicted in the images on the right in Figure 5.9 as a red line superimposed to the preprocessed images. Comparing the wakes at both distances, the energized mass method is capable of detecting the widening of the wake at the bottom which was observed in subsection 5.1.1. In addition, the wake of the arms increases in height, but the edges become less uniform.

Figure 5.10 shows the resulting wake area contour superimposed to the instantaneous velocity field that corresponds to it. The images have been cropped in order to show the wake more clearly. The image shows that the wake are is overestimated. The main differences between the images at the two locations is that at a higher distance from the skater, the wake has expanded horizontally and has a larger area. It is also clear that at a larger distance, the algorithm has more difficulties in identifying the arms properly, and the shape of the wake looks less defined.

For the experimental case of the skater in high drag position there is an added difficulty in the wake area identification. As explained in chapter 3, one of the steps in the method is to cluster

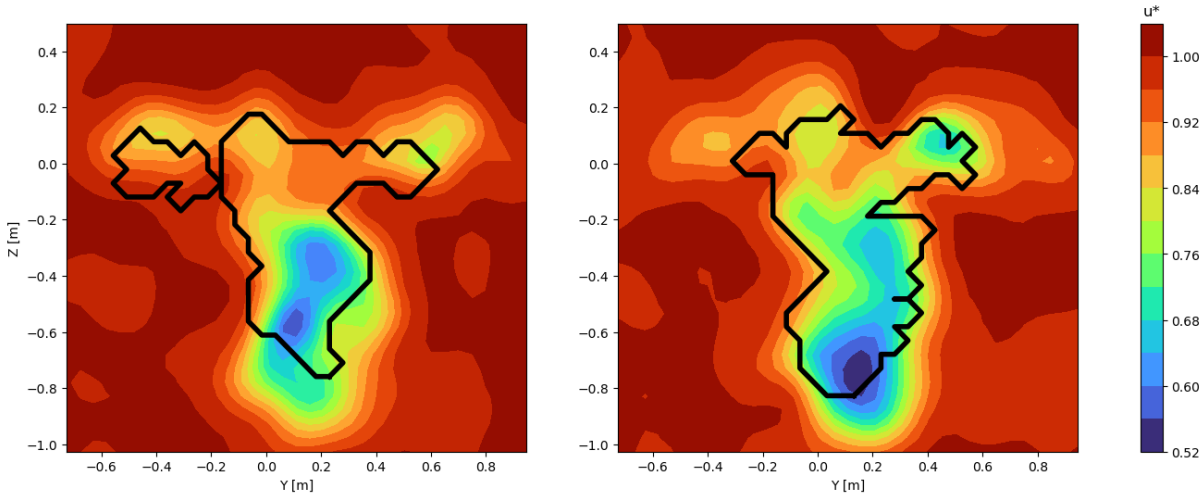

Figure 5.10: Instantaneous streamwise velocity fields and energized mass wake area for locations $x = 0.5\,\mathrm{m}$ and $x = 1.5\,\mathrm{m}$ behind the high drag position skater.

all the windows identified as wake, and select only the largest cluster. Because of this, the wake is always a single group of points.

However, if the body is not compact, the actual flow regions with a high enough velocity deficit to be considered wake might be isolated, forming different smaller clusters. This is precisely the case of the skater, as shown in Figure 5.11. The wake area detected with the energized mass method is shown as a contour indicated by the red line, while Figure 5.11 (b) shows the area resulting from applying a threshold of $0.37U$ on the wake velocities obtained with PIV. The threshold is selected based on the reasoning presented in chapter 4, which stems from the fact that if it is assumed that the wake usually has a Gaussian velocity distribution with highest velocity of U, the top-hat distribution with equivalent area would have a velocity value of $0.37U$.

The wake area shown in Figure 5.11 (b) is indicated by the yellow regions. The two arms and body can still be identified, but clearly they are bubbles of lower velocity fluid and not a single compact shape. The measured area represented by the red line in Figure 5.11 (a) measures $0.91\,\mathrm{m}^2$, while the area obtained using a velocity deficit threshold as shown in Figure 5.11 (b) is of $0.62\,\mathrm{m}^2$. In this case, the clustering approach is not an appropriate solution, as it will include regions that should not be classified as wake, and therefore the obtained drag area is significantly higher than the expected result.

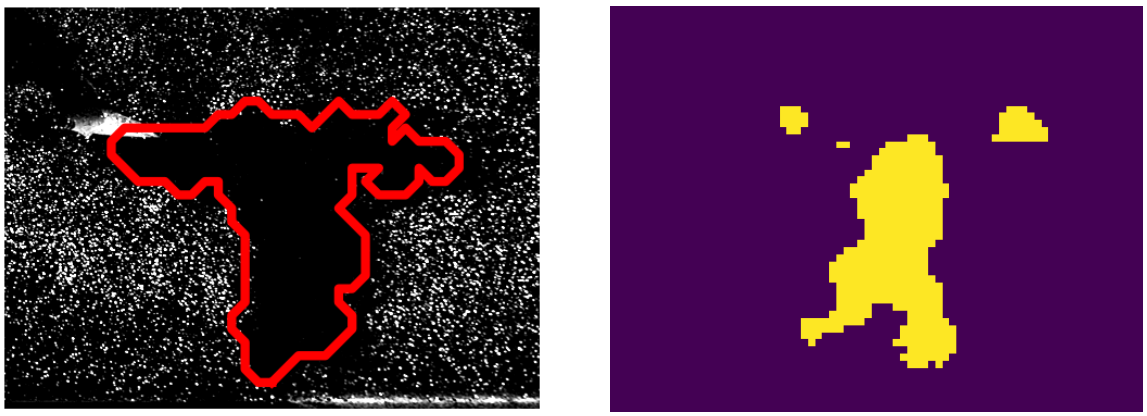

(a) Intensity method detected area.

(b) Velocity threshold ($0.37U$) detected area.

Figure 5.11: Plots showing the detected area by the method presented in this work (left) and by applying a threshold of 37% of the velocity deficit (right).

The measured area of the wake is plotted against position in Figure 5.12. The solid line represents

the average of the used runs, while the shaded area represents the uncertainty of the results. The plot shows that the spread increases with the distance from the skater, which can be explained as a consequence of the velocity deficit reducing, and the boundaries of the wake becoming less clear. Overall, the area increases in size with position, as expected, going from $0.8\,\mathrm{m}^2$ to $1.2\,\mathrm{m}^2$ in the span of $0.2\,\mathrm{m}$. However, the values are significantly higher than the expected ones. The momentum balance method was used to determine a reference value of $c_D A$ =$0.16\,\mathrm{m}^2$ for the high drag position skater. This method yields a value of $c_D A$ =$0.66\,\mathrm{m}^2$. Since the high drag position is not a common position in ice skating, it is not possible to obtain other values of drag area from literature.

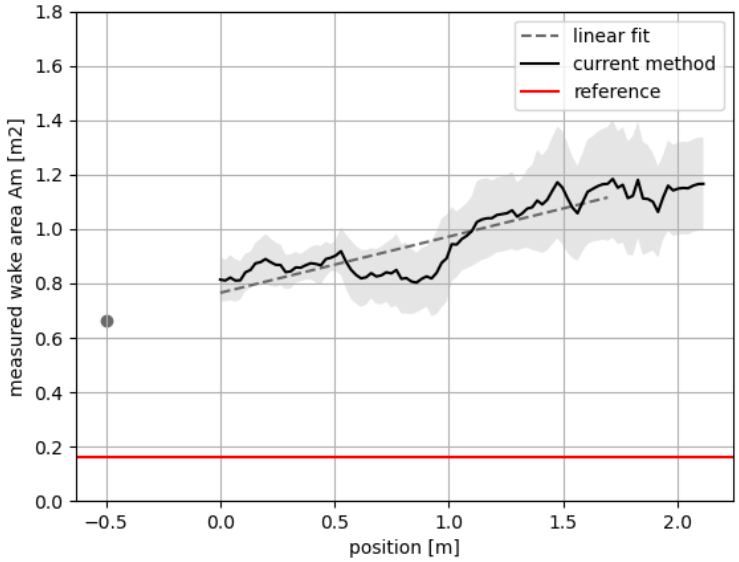

Figure 5.12: Measured wake area change with distance to the back of the high drag position skater (black solid line) and uncertainty of the values (shaded gray). The linear fit (gray dashed line) is extrapolated to the location of the skater (gray dot). Reference $c_D A$ value shown in red..

5.2 Cyclist

The results of the energized mass method applied to a cyclist are presented in this section. The process was applied onto already existing images from the campaign performed by Spoelstra et al. [4] [20]. The images were taken using a stereo-PIV set up with the intention of applying a momentum balance method to find the drag area. In this section, first the wake topology will be discussed, in order to give some background on the wake of the cyclist, followed by a discussion of the energized mass method results.

5.2.1 Wake topology

Since aerodynamic drag is the the major factor contributing to resistance in cycling, the wake and drag area of cyclists have been the topic of considerable research. In this section, the velocity fields, vorticity fields and time evolution of the wake of a cyclist will be analysed.

In this discussion, the dimensionless time t^* will be used to indicate the distance in the wake from the cyclist. It is defined as follows [4]:

$$t^* = \frac{t \cdot U}{c} \tag{5.1}$$

Where t is the time, U is the velocity of the cyclist, which has a value of $U = 8.3\,\mathrm{m\,s^{-1}}$, and c is the torso chord length, which is c =60 cm. For reference, a value of $t^* = 3$ would correspond to a distance of $x = 1.8\,\mathrm{m}$ in the wake.

Similarly to the case of the skater, two different positions will be studied in the case of the cyclist. The upright position, where the skater has his hands in the break hoods, is expected to have a higher drag area than the time trial position, where the skater rests his arms on aero-bars, achieving a lower positioning of the upper body.

Velocity fields

The instantaneous streamwise velocity field for a cyclist in upright position is shown in Figure 5.13 (left), while the time trial position is shown in Figure 5.13 (right). The figure shows contours of u_x, which is the streamwise velocity component non-dimensionalised as explained in chapter 4. In addition, the black vectors indicate the in-plane velocity field. In all cases, the velocities presented are ensemble averaged.

The flow field in the wake of the cyclist in upright position has a width of approximately 1 m at all points, except for the lowest part of the wake, which would be located behind the wheels. The location of the lowest streamwise velocities is behind the legs of the cyclist. The maximum velocity deficit, which reaches 45%, is found in two regions, one behind each leg. The in-plane velocity vectors show downwash throughout the back of the cyclist, and inwash caused by both hip vortices.

In the time trial position, shown in the right, the shape of the wake is wider in the lower half, reaching almost 1 m width, while the wake of the upper body has a width of approximately 0.5 m. While the width of the lower half of the wake for the upright and time trial positions is similar, the flow structures present some differences. The value of the maximum velocity deficit is the same, and in both cases it is located behind the legs. However, in the time trial position there is one single larger region of high velocity deficit, instead of two smaller ones, and it is slightly displaced to the left half of the wake. This might be explained by the difference in crank angle in both cases.

Even though the torso of the cyclist was positioned in a higher angle with respect to the horizontal in the upright position, the wakes of both cases have a similar height of 1.5 m. This

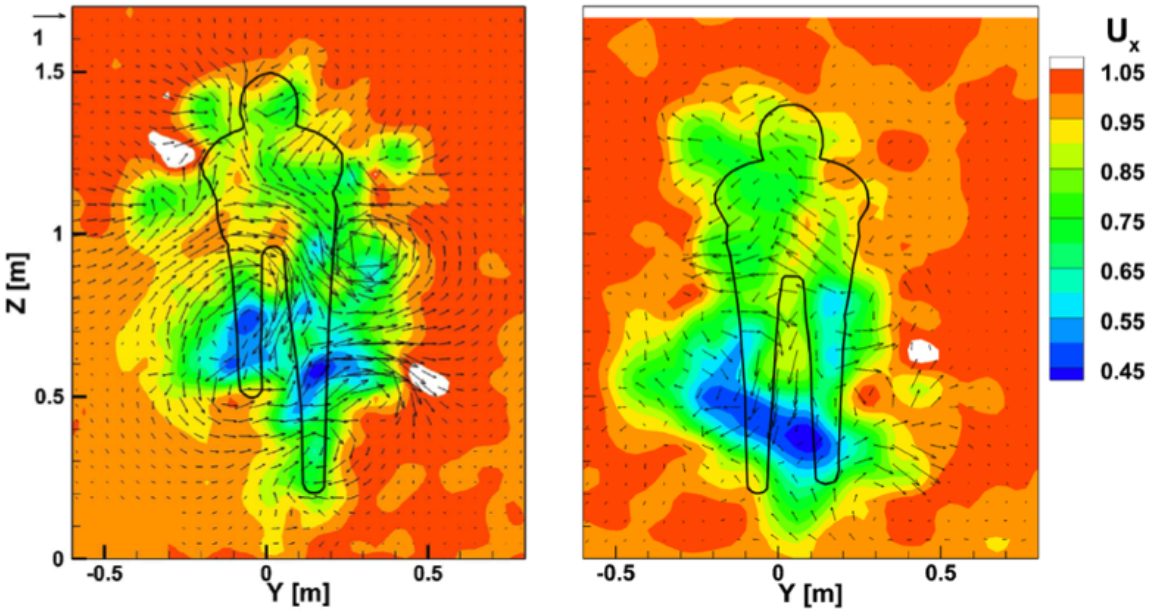

Figure 5.13: Instantaneous velocity field of the wake of a cyclist in upright position (left) and time-trial position (right), at a distance of $t^* = 3$, from [4].

might appear surprising, but similar results have been reported by [117]. A possible explanation has to do with the development of the head vortices and their interaction with the flow on the back of the cyclist, which is explained in the following subsection.

The position of the legs, and thus the crank angle ϕ, is essential to discuss the lower half of the wake. The crank angle has a strong effect on the wake structures, and on the drag of the cyclist. In fact, it has been shown that the drag coefficient can experience a variation of 20% depending on it, with the highest drag occurring at highly asymmetrical positions ($\phi = 75°$ and $\phi = 255°$). The lowest drag was found for symmetrical positions ($\phi = 0°$, $\phi = 180°$), and crank angles within 15 degree of them [118].

The crank angle for the upright position is $\phi = 65°$ [4], which means the right leg was extended (but not fully), and the left leg was raised. This is illustrated by the cyclist silhouette in Figure 5.13. This asymmetry in the leg position is clearly reflected on the flow field. Firstly, the wake is wider behind the raised leg, which is in line with the results of Crouch et al. [118]. The high velocity deficit region is also slightly higher behind this leg. Some vortices can already be detected from the in-plane velocity field vectors. In Figure 5.13, the vortex at the upper hip of the extended leg is clearly distinguishable on at $y = 0.3\,\mathrm{m}$, while the vortex caused by the lower hip of the raised leg can be observed at $y = -0.1\,\mathrm{m}$.

The position of the crank in this particular frame in the time trial position is of $\phi = 320°$ [4], which makes the position almost symmetrical. Figure 5.13 shows that the wake is not symmetrical, even though the position of the legs is. For a crank angle of $\phi = 360°$ (where the legs would be exactly at the same height), it would be expected that the flow would separate symmetrically in the lower back, leading to a wake that was symmetrical and wider behind the hips. However, since in Figure 5.13 the left leg is slightly more extended than the right one, the location where the flow separates is not the same for both legs. Since the cyclist was pedalling during the measurements, the wake might also be influenced by unsteadiness of the legs.

Vorticity

The ensemble averaged vorticity field for a cyclist in upright position is shown in Figure 5.14 (left), while the vorticity for the time-trial position is shown in Figure 5.14 (right). The locations where the vortices are shed are indicated in the image as well.

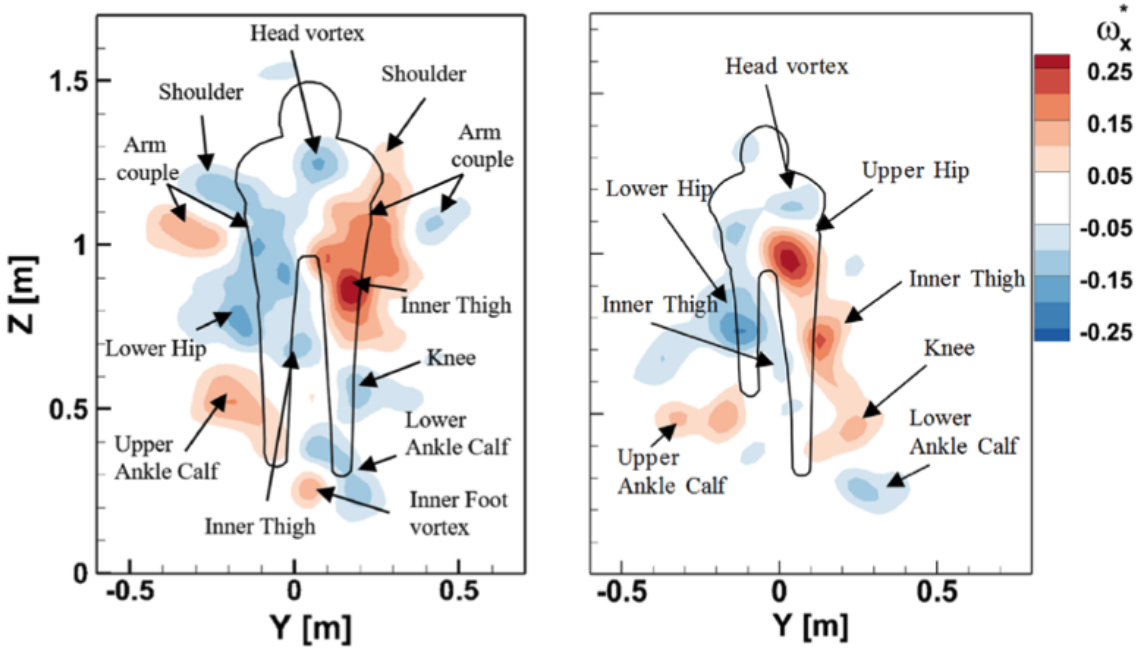

Figure 5.14: Ensemble averaged non-dimensional vorticity field of the wake of a cyclist in upright position (left) and time-trial position (right), at a distance of $t^* = 1.5$, from [4].

In general, the vorticity in the wake of a cyclist is dominated by the hip and thighs quadruple of vortices. They have been observed to be the most intense vortices, and also the longest lasting ones [118]. However, their behavior depends on the position of the legs and the crank angle. On the left image, the upright positioned cyclist has a crank angle of $\phi = 30°$ [4], meaning that the right leg is slightly more extended than the left leg. For the time trial position, the crank angle is $\phi = 110°$ [4] so the right leg is stretched and the left leg is raised. The effect of the leg position on the vorticity field behind the legs is obvious, but can also impact the flow field in other regions [118] [4].

The upright vorticity plot shows an almost symmetric vorticity field. The symmetric flow regime in the wake of a cyclist is the low-drag regime, where the main vortices are shed from both hips at the same height and the inner thighs. Even though the vortices from both sides would be expected to have similar magnitudes [118], the right half vortex is more intense. In addition, Figure 5.14 shows only one vortex on the upper right leg, when both hip and thigh vortices would be expected. This can be explained because the vorticity field is taken at $t^* = 1.5$ (which corresponds roughly to $x = 1\,\text{m}$ behind the rear wheel of the bicycle), and the hip and thigh vortices have probably merged into a single more intense vortex. The cause of the hip vortices is probably the pressure difference between the frontal part of the torso and the back. The hip and thigh vortices are responsible for the downwash observed in the in-plane velocity field in Figure 5.13, and they also generate some inwash.

The upright position also includes some new vortices that are not found in the time trial position wake. These are vortices shed by the shoulders and arms. In the case of the shoulder vortices, they have the same sign but lower magnitude than the hip vortices. This suggests that the mechanism that generates them is the same, 3D separation [4] [117]. Each arm generates a vortex couple, which is not observed in the time trial position vorticity field because the arms

are not extended. Finally, the helmet vortices have a lower intensity in the upright position, compared to the time trial position.

The time trial position vorticity field, shown in Figure 5.14 (right), is clearly not symmetric due to the crank angle. In such an asymmetrical position, the vortices are shed from different locations in each leg. In the extended leg (which in Figure 5.14 is the right leg), the vortices are shed from the upper hip. Here, the flow separates early, creating an area of high intensity of vorticity. On the raised leg (which in this case is the left leg), the flow remains attached for longer at the hip, and only separates near its base. As a consequence, the vortex shed from this location is not only lower in intensity, it is also at a lower position in the wake. In addition, another vortex pair with same sign as the hip vortices is formed at the inner thighs. This has been observed in literature as well [103] [119] [118].

In addition to the main vortices, there are several others that are identifiable. The extended leg sheds vortices, which can be distinguished as originating from the knee, the calf and the ankle, based on their location. The other leg sheds a less intense vortex, which is slightly higher in the wake. The head in time trial position sheds a vortex higher magnitude than in upright position. The intensity of this vortex might be the reason that the height of both wakes is the same, even though the head is positioned lower in time trial position.

Wake development

The time development of the wake is depicted in Figure 5.15, which shows six different snapshots of the ensemble averaged velocity fields at the wake of the cyclist, all at different distances from the wake. As shown in Figure 5.13, in the near wake the maximum velocity deficit is close to $U_x = 0.45$, and the wake is wider behind the legs of the cyclist. Over time, the maximum velocity deficit is reduced while the wake area increases due to entrainment. The wake also increases in size and looses definition, broadening at the lower half, behind the cyclist's legs. This is due to the downwash flow in this area created by the vortices at the hips and thighs, shown in Figure 5.14, and which is also visible through the streamlines plotted in Figure 5.15. The presence of the floor forces the flow to go sideways. In addition, the wake behind the legs is complicated by the unsteadiness of the pedalling motion of the cyclist. In the far wake, the wake eventually is wide enough to expand outside of the measurement domain, which causes issues for momentum balance approaches to calculate the drag. However, the energized mass method is concerned only with the near wake.

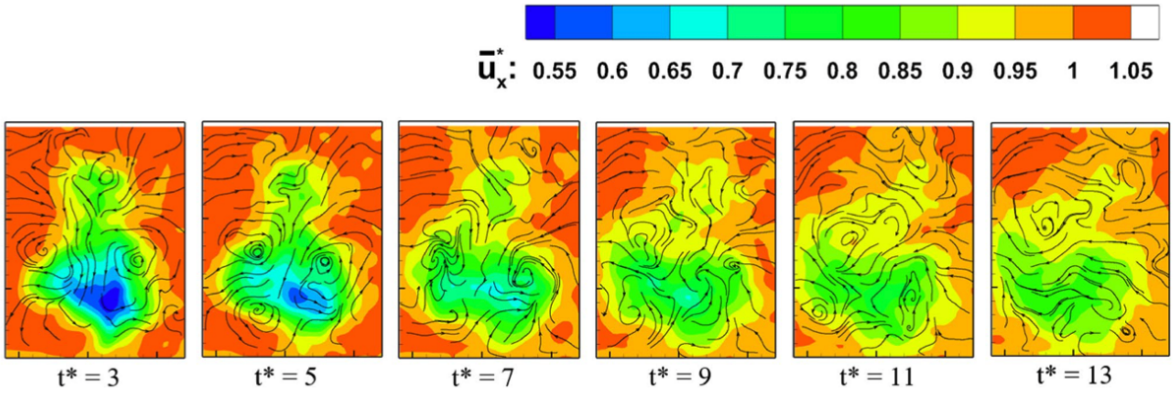

Figure 5.15: Ensemble averaged velocity fields of the wake of a cyclist in time trial position at different locations in the wake, from [4].

5.2.2 Energized mass method

The results of applying the energized mass method to the cyclist data are presented in this section. First, the time trial position is examined, followed by the upright position. For each case, some intermediate steps will be presented and discussed, and the drag calculated in each case is determined.

Time trial (low drag) position

The energized mass method was applied on the time trial cyclist data. Figure 5.16 and Figure 5.17 show snapshots of some of the processing steps for a single run at two different positions in the wake, at a distance of $x = 0.5\,\mathrm{m}$ and $x = 1.4\,\mathrm{m}$ behind the cyclist.

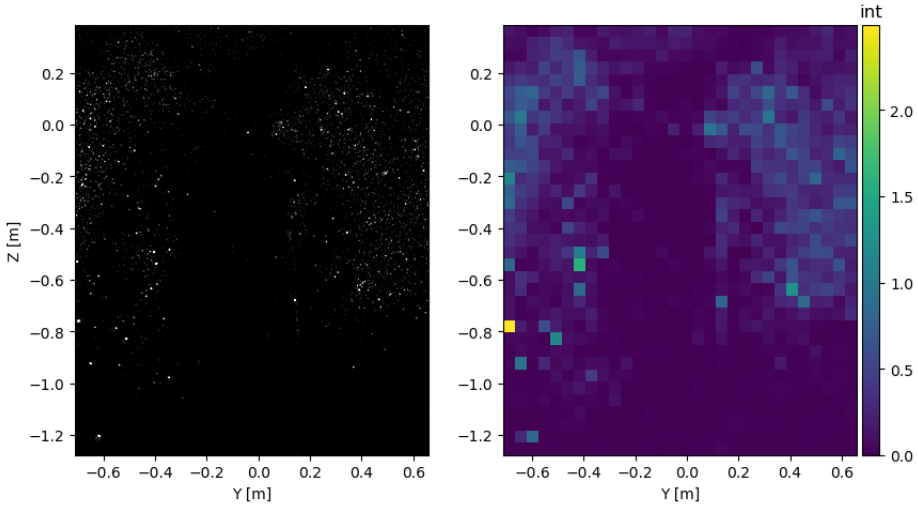

(a) Distance of $x = 0.5\,\mathrm{m}$.

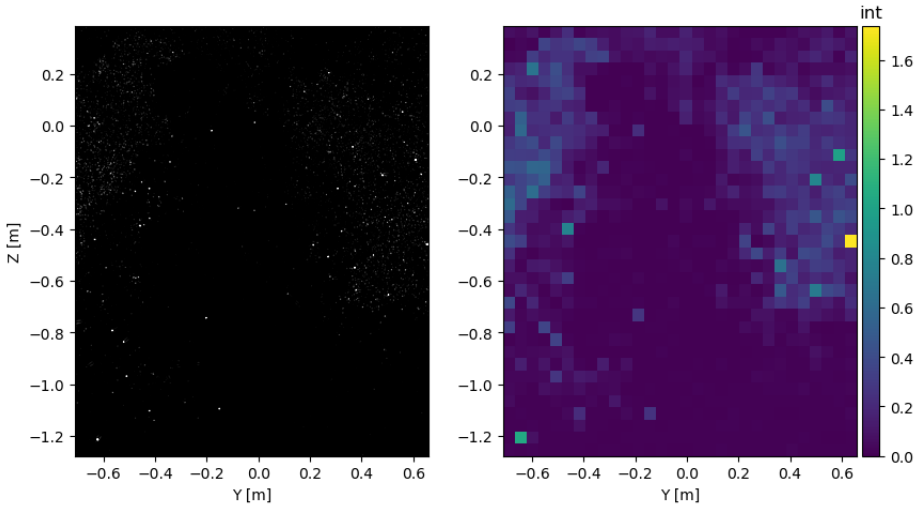

(b) Distance of $x = 1.4\,\mathrm{m}$.

Figure 5.16: Preprocessed image (left) and image after dividing it into intensity average windows, at a distance of (a) $x = 0.5\,\mathrm{m}$ and (b) $x = 1.4\,\mathrm{m}$ from the back of the cyclist in time trial position.

The left images in Figure 5.16 show the images after preprocessing had been applied to them. Compared to the equivalent images in the two skater cases (shown in Figure 5.4 and Figure 5.8), it is clear that the seeding is less dense in this case, which makes the wake less easily identifiable. The amount of particles present is less and the ones that appear in the image have lower values of intensity. The wake appears as a darker area near the centre, but the region near the floor could be confused with the wake due to the lack of particles there.

This effect can also be seen in the images on the right in Figure 5.16, which show the result of dividing the left images into windows, and assigning to each window the value of the average intensity of all the pixels included in it. While the wake area can also be identified as darker regions in the centre of the frame, the intensity is much more uniform than in the case of the skater. The maximum values of intensity found are significantly lower for the cyclist images. To the naked eye, the wake area becomes more noticeable when looking at images showing the intensity windows.

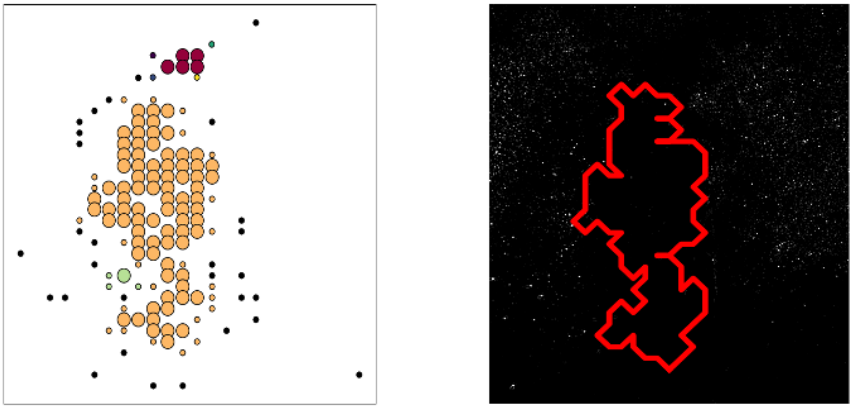

(a) Distance of $x = 0.5\,\mathrm{m}$.

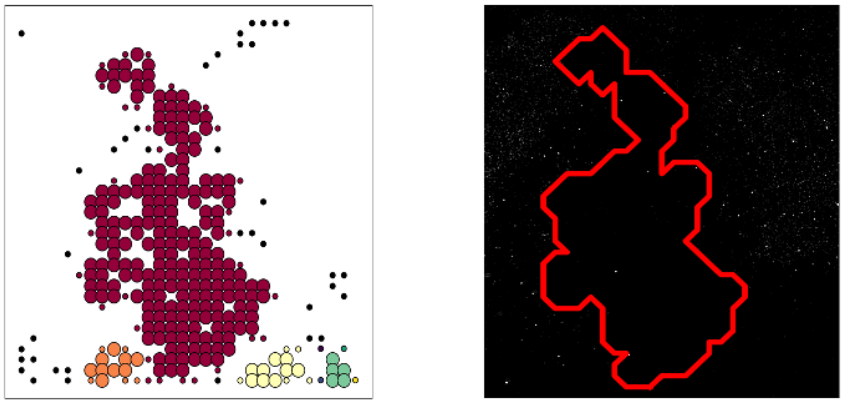

(b) Distance of $x = 1.4\,\mathrm{m}$.

Figure 5.17: Clustering results (left), and energized mass wake (right) for locations of $x = 0.5\,\mathrm{m}$ and $x = 1.4\,\mathrm{m}$ behind the cyclist in time trial position. All dots that have the same color belong to the same cluster, while smaller black dots represent noise.

Figure 5.17 shows snapshots of the remaining steps. In these images the evolution of the wake in time is more obvious. The left images show the output of the clustering algorithm. Because of the low contrast in intensity between wake and non-wake regions, there is more noise and the wakes are less compact than in the case of the skater in section 5.1. In addition, the image at distance of 1.4 m shows the consequence of scarcer seeding at the near the floor, which was clear in the preprocessed images shown in Figure 5.27. The clustering method is able to identify this as noise and not tag it as part of the wake. However, in other frames where there are less particles in this area, the lower intensity region might be big and close enough to the real wake to be considered part of it. In these cases, the wake area is over-estimated, which causes the drag to be over-estimated as well.

The images on the right in Figure 5.17 show the final result of the energized mass method. The measured wake area is depicted as a red contour, superimposed to the sliding minimum images for reference. Examining both final images to the expected behavior of the wake, can give some insight on the limitations of the energized mass method. Firstly, the wake broadens in the lower

region, as was observed using the PIV velocity fields. The wake is also expected to move down farther away from the body. However, the wake in Figure 5.17 (b) is taller than in Figure 5.17 (a). Examining the clustering image, it seems possible that a small region with uneven seeding was located right above the wake of the head of the cyclist, and due to the close distance to the real wake, the clustering algorithm was not able to identify it as noise. Finally, the edges of the wake are less smooth than the ones observed in PIV velocity fields.

This can also be observed in Figure 5.18, which shows the same wake contour, this time superimposed to the corresponding instantaneous PIV velocity fields. Here, the differences in shape, and most importantly size are easy to see. The general shape is similar in both frames. For the frame closer to the cyclist (left, $x = 0.5\,\mathrm{m}$), the vertical length of the wake matches the velocity contours well. However, it includes a region of lower velocity deficit at the top, while near the floor a region of very low velocity is not included. The wake is also wider in the top region, which is not observed in the velocity fields. Regarding the frame farther from the cyclist (right, $x = 1.4\,\mathrm{m}$), it is clear that the energized mass method erroneously includes an area at the top of the wake. In addition, even though the general widening of the wake is supported by the velocity fields, the wake is wider than would be expected.

The discrepancies regarding small regions that are not detected properly can be explained by the fact that the energized mass wake is not detected from a single pair of images, as is the case with the velocity field. Since 9 images are used for the sliding minimum, the exact shape of the wake cannot be expected to be reproduced. However, Figure 5.18 shows that the energized mass method generally includes areas with a lower velocity deficit than desired.

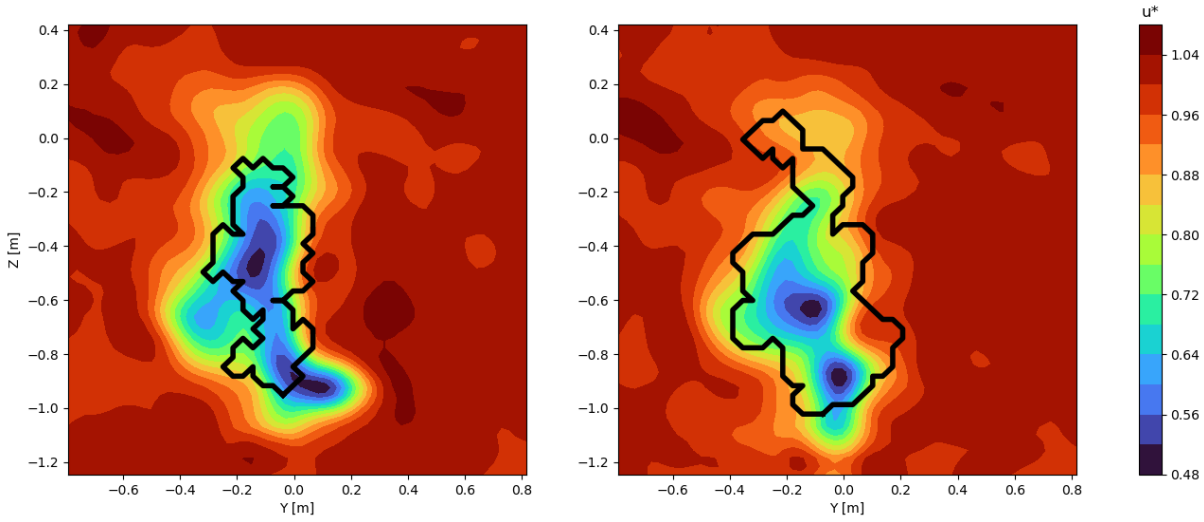

Figure 5.18: Instantaneous streamwise velocity fields and energized mass wake area for locations $x = 0.5\,\mathrm{m}$ and $x = 1.4\,\mathrm{m}$ behind the cyclist in time trial position.

The area that is measured with the energized mass method is plotted against distance from the cyclist in Figure 5.19. The solid black line indicates teh average development of the wake area against the position at which it was measured. The shaded area represents the uncertainity of the measurement, and the dashed line is the linear fit of the curve. The reference value, which is taken from Spoelstra et al. [4], is shown as a solid red line.

The obtained drag area is $c_D A = 0.55\,\mathrm{m}^2$, which is significantly higher than values reported in literature. For the same data, Spoelstra et al. [4] obtained a value of $c_D A = 0.25\,\mathrm{m}^2$ with the momentum balance method, which relies on the PIV velocity field shown in subsection 5.2.1. Other research supports the results obtained with the Ring of Fire. In wind tunnel tests where the drag of real human on a bicycle was measured, results of $c_D A = 0.21\,\mathrm{m}^2$ [106], $c_D A = 0.21\,\mathrm{m}^2$ - $0.25\,\mathrm{m}^2$ for different cyclists [120], $c_D A = 0.24\,\mathrm{m}^2$ [121], $c_D A = 0.29\,\mathrm{m}^2$ [9], $c_D A = 0.31\,\mathrm{m}^2$ to $0.38\,\mathrm{m}^2$ for different velocities [122], were obtained. For mannequins in a wind tunnel,

$c_D A = 0.24\,\mathrm{m}^2$ [119], $c_D A = 0.25\,\mathrm{m}^2$ [123]. The overestimation of the drag area is on the same order magnitude as observed with the low drag position skater, which might indicate that the assumptions that are intrinsic to the method are not acceptable. The uneven seeding observed in Figure 5.16 might also explain this.

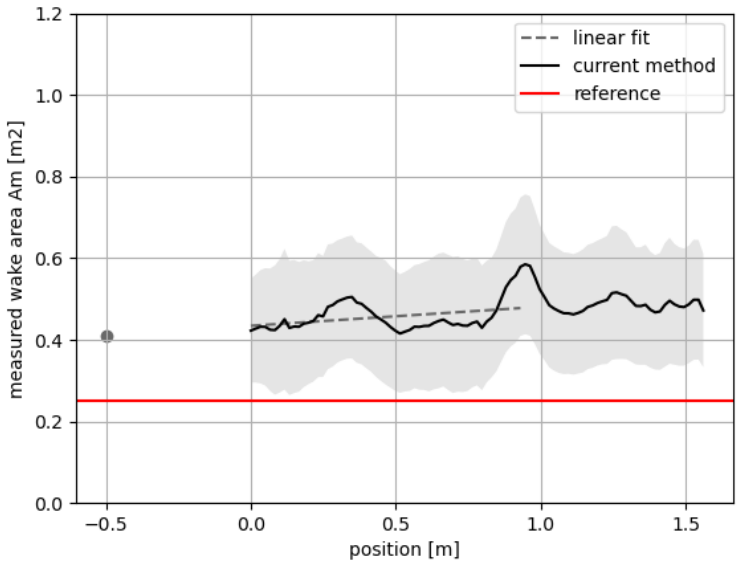

Figure 5.19: Measured wake area change with distance to the back of the cyclist in time trial position (black solid line) and uncertainty of the values (shaded gray). The linear fit (gray dashed line) is extrapolated to the location of the skater (gray dot). Reference $c_D A$ value shown in red.

Upright (high drag) position

The images taken of the same cyclist in upright position were also processed with the energized mass method, in order to further understand its limitations. The results are explained in this section.

Snapshots of the first processing steps are shown in Figure 5.20 for distances of $x = 0.5\,\mathrm{m}$ and $x = 1.4\,\mathrm{m}$ from the rear wheel of the cyclist. At this point in the process, it is very difficult to distinguish any major differences between these images and the ones shown in Figure 5.16, where the cyclist was in time trial position. The images on the left show the frames once they have been preprocessed, in the format in which they are the input to the python processing script. Similarly to the case of the time trial cyclist, the particles present in this images are not abundant, and their intensity is relatively low compared to the skater preprocessed images, explained in section 5.1.

The right column in Figure 5.20 shows the images once they have been divided into windows where the intensity is averaged. In these images it is possible to see an overall higher intensity in the top frame, which is taken at a closer distance from the cyclist. In Figure 5.20 (b), the wake has expanded further, so the central region of lower intensity is larger. In general, these images show low values of intensity on the windows that are clearly not part of the wake. This is dealt with by adjusting the value of the intensity threshold, but the images still remain more susceptible to wrongful identification of noise as part of the wake, or to less well defined edges in the wake.

Figure 5.21 shows some of the last steps in the energized mass process. The left images show the clustering of the points previously tagged as wake. Comparing the clusters at both locations, it is evident that the wake farther from the body is wider, as expected from analyzing the wake

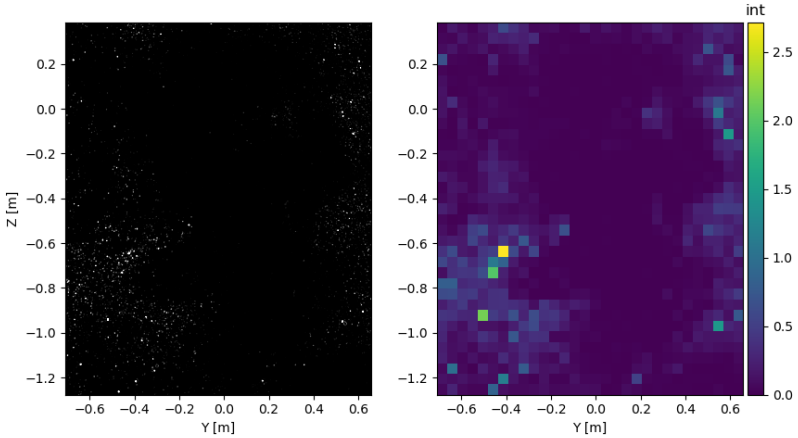

(a) Distance of $x = 0.5\,\mathrm{m}$.

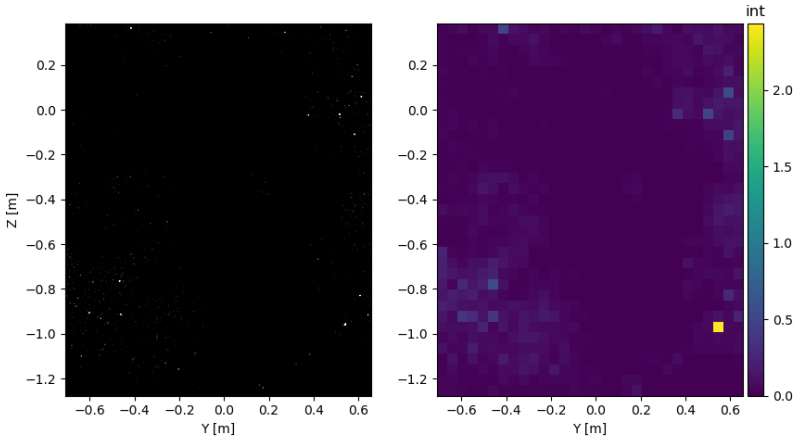

(b) Distance of $x = 1.4\,\mathrm{m}$.

Figure 5.20: Preprocessed image (left) and image after dividing it into intensity average windows, at a distance of (a) $x = 0.5\,\mathrm{m}$ and (b) $x = 1.4\,\mathrm{m}$ from the back of cyclist in upright position.

topology in subsection 5.2.1. There is also a slight increase in the height of the wake. In addition, more noise is present at a distance of $x = 1.4\,\mathrm{m}$. The noise can be seen as smaller black dots, or as any cluster that is not the largest one (shown in red). The usefulness of the clustering step is reflected in Figure 5.21. In both frames, there is an area without particles that can be detected with the naked eye on the bottom right corner. Looking at the distribution of the particles, it can be deduced that this corner is not part of the wake, and the cause of its lack of particles is probably uneven seeding. The clustering algorithm makes it possible to separate this area from the rest of the wake. In both cases the clustering results show wakes which are not completely solid. The holes in the wakes are filled, as they usually caused by reflections or single particles that were not removed with the sliding minimum filter.

The resulting detected wake area is shown on the right images in Figure 5.21. In this case, superimposing the wake to the preprocessed images does not bring a lot of clarification on whether the wake was detected properly, since it is difficult to distinguish from the particle distribution. As expected, the edges of the wake seem to be more affected by noise and are less defined, even for the frame taken at $x = 0.5\,\mathrm{m}$ (top images). However, the increase in area of

the wake is evident.

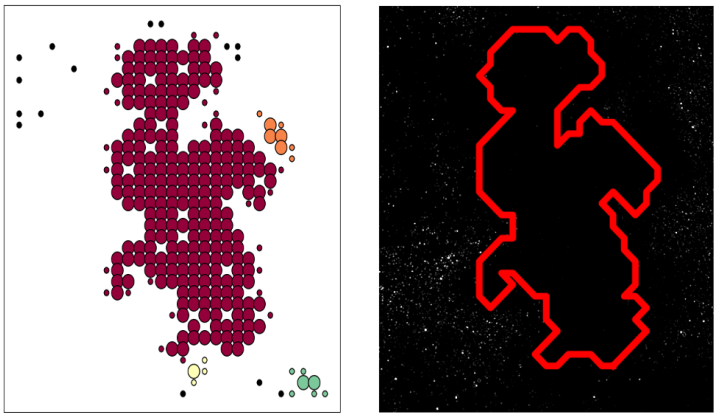

(a) Distance of $x = 0.5\,\mathrm{m}$.

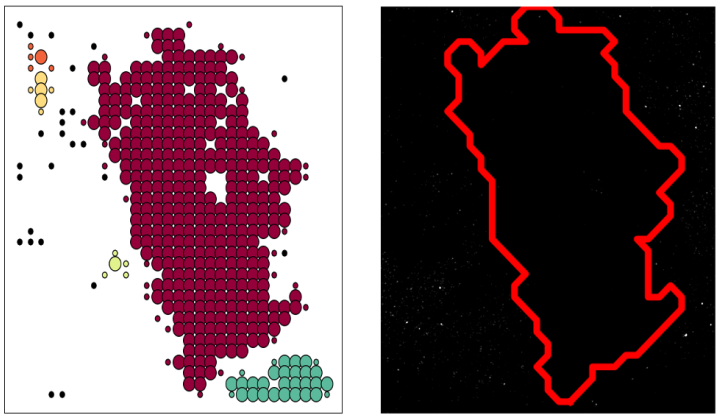

(b) Distance of $x = 1.4\,\mathrm{m}$.

Figure 5.21: Clustering results (left), and energized mass wake (right) for locations of $x = 0.5\,\mathrm{m}$ and $x = 1.4\,\mathrm{m}$ behind the cyclist in upright position. All dots that have the same color belong to the same cluster, while smaller black dots represent noise.

Figure 5.22 shows the streamwise velocity fields of the wake of the upright cyclist at the same positions of $x = 0.5\,\mathrm{m}$ and $x = 1.4\,\mathrm{m}$. The wake detected by the energized mass method appears superimposed to the velocity contours, depicted by a solid black line. The overall shape and size of the wake matches the regions of lower velocities in the wake. However, for the frame at $x = 0.5\,\mathrm{m}$, there are some areas of high velocity deficit which are not included in the detected wake. The energized mass wake and velocity contours are not expected to match exactly, as the velocity contours are instantaneous and the energized mass wake uses information from nine consecutive frames in the case of the upright positioned cyclist.

Figure 5.23 shows the development of the energized mass wake area with respect to the distance from the real wheel of the bicycle as a solid black line. In the same image, the standard deviation is shown as a gray shaded area. In addition, a gray dashed line indicates the linear fit starting from the first frame until the frame with the highest detected wake area. This linear fit is extrapolated to the location of highest cross-sectional area of the cyclist, which is estimated to be 0.5 m in front of the rearmost part of the bicycle. The solid red line indicates the reference $C_D A$, which was obtained by Spoelstra et al. [4] using the same data and applying the Ring of Fire concept, which is based on momentum balance.

The drag area obtained with the energized mass is significantly higher than the reference value, as has been observed in all the other cases presented in this chapter. In particular, the energized mass method yields a value of $C_D A = 0.46\,\mathrm{m}^2$, while Spoelstra et al. reported a drag area of

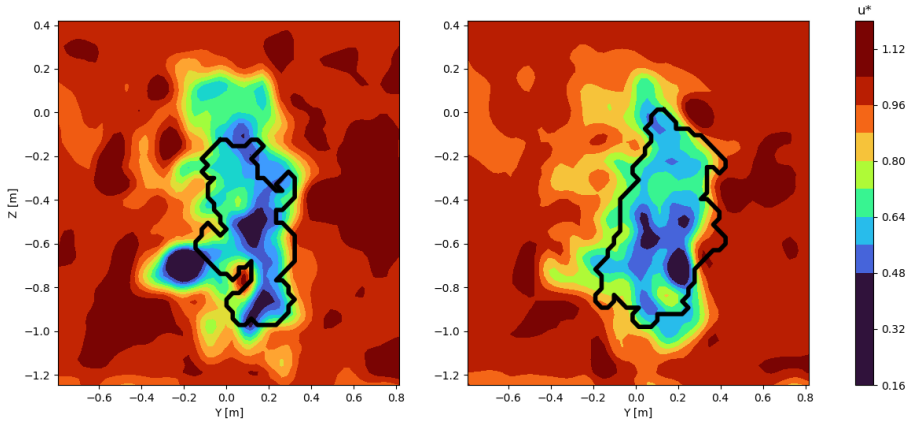

Figure 5.22: Instantaneous streamwise velocity fields and energized mass wake area for locations $x = 0.5\,\mathrm{m}$ and $x = 1.4\,\mathrm{m}$ behind the cyclist in upright position.

$C_D A = 0.34\,\mathrm{m}^2$ [4]. Other examples in literature suggest that the results of Spoelstra might be more accurate: for wind tunnel experiments of cyclist in similar positions, results of $C_D A = 0.46\,\mathrm{m}^2$ [102] $C_D A = 0.31\,\mathrm{m}^2$ [107] $C_D A = 0.27\,\mathrm{m}^2$ [106] and $C_D A = 0.34\,\mathrm{m}^2$ to $C_D A = 0.42\,\mathrm{m}^2$ (for different cyclist speeds) were reported.

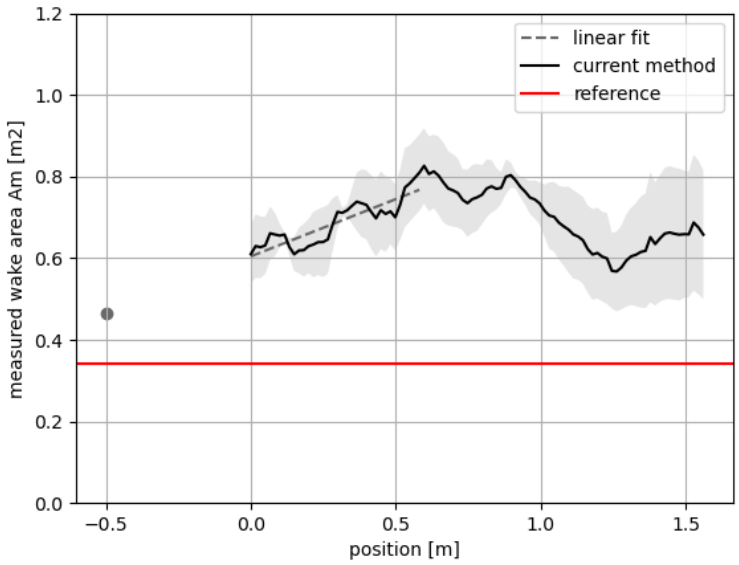

Figure 5.23: Measured wake area change with distance to the back of the cyclist in upright position (black solid line) and uncertainty of the values (shaded gray). The linear fit (gray dashed line) is extrapolated to the location of the skater (gray dot). Reference $c_D A$ value shown in red.

5.3 Sphere

This section is focused on the wake and drag of a sphere. The experimental campaign that produced the images of the sphere was carried out in 2016 by Terra et al. [3]. The objective of the work was to demonstrate the Ring of Fire method to calculate the drag of an object moving with constant velocity. Tomo-PIV was selected as the setup, which is described in more detail in chapter 4. In this section, first the wake topology of the sphere will be discussed using the results of Terra et al. [3]. Afterwards, the results of the application of the energized mass method on the images of the sphere will be presented.

5.3.1 Wake topology

Since the sphere is a fundamental shape, its wake has been studied extensively. The data of the sphere was collected by Terra et al. [3] during a campaign dedicated to assessing the feasibility of the Ring of Fire method to measure the drag of an object. The sphere moved at a velocity of $U = 1.33\,\mathrm{m\,s^{-1}}$ and had a diameter of $D = 10\,\mathrm{cm}$.

Velocity field

The flow structures in the wake of a sphere depend strongly on the Reynolds number of the flow. In this case, the Reynolds number was $\mathrm{Re} = 10^4$, which falls into the subcritical range [124].

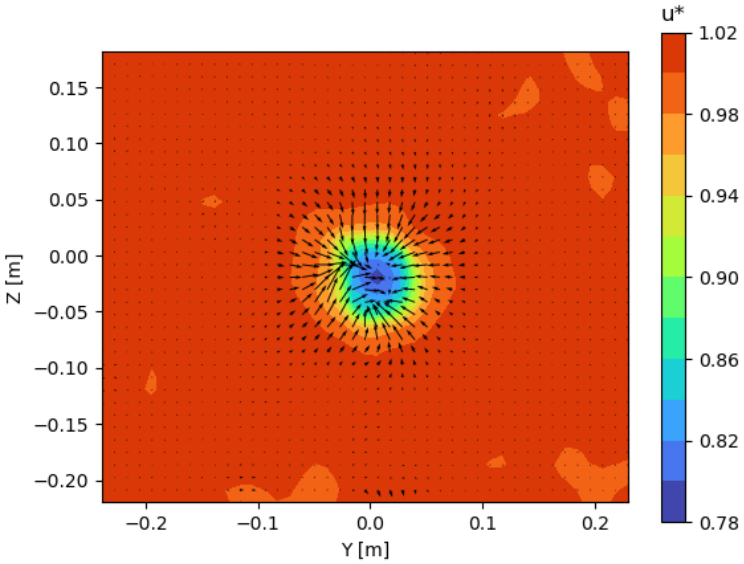

Figure 5.24: Ensemble averaged velocity fields of the wake of a sphere at $x = 0.05\,\mathrm{m}$.

The ensemble averaged streamwise velocity field of the wake of the sphere is presented in Figure 5.24. The black vectors indicate the in-plane ensemble averaged velocity field. The distance from the sphere in this case is of $x = 0.05\,\mathrm{m}$, which corresponds to half a diameter. The wake of the sphere can be clearly distinguished as a circular area of lower velocity. The maximum velocity deficit is located at the centre of the wake, and it has a value of $0.8U$. Considering that the sphere has a diameter of $D = 10\,\mathrm{cm}$ and was centred in the image, the wake has roughly the same dimensions as the sphere. As expected, the wake is axisymmetrical.

At subcritical Renoylds numbers in a sphere, the boundary layer remains laminar and separates before it can transition into turbulent. The separation point is approximately constant for $10^4 <$

$\mathrm{Re} < 3 \cdot 10^5$. The location of the separation point is usually indicated by the angle between this point and the most upstream point of the sphere. This separation angle has been observed to have values ranging between 80° and 90° for Reynolds numbers close to 10^4 [124] [125] [126]. After separation the shear layer remains laminar for a short distance, roughly one diameter from the back of the sphere [127] [128] [129]. The region of recirculation ends with a stagnation point. Transition is caused by the growth of instabilities in the laminar shear layer. Further downstream, the wake is fully turbulent and is characterized by the shedding of vortex pairs. As indicated by the in-plane velocity field in Figure 5.24, the wake of the sphere features also axisymmetrical inwash caused by the lower pressure area behind the object.

Vorticity

The ensemble average vorticity field in the wake of the sphere, at a distance of $x = 0.5\,\mathrm{m}$ it (half a diameter), is shown in Figure 5.25. The in-plane velocity field is also shown as a gray vector field.

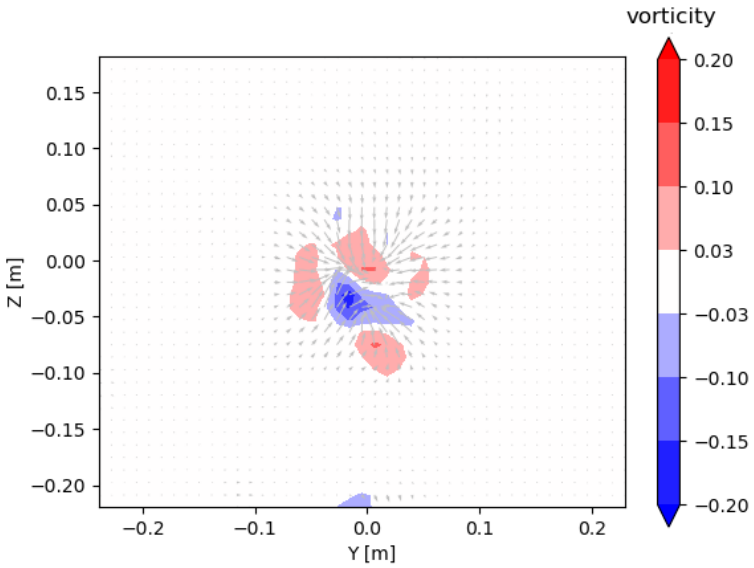

Figure 5.25: Ensemble averaged non-dimensional vorticity of the wake of a sphere at $x = 0.05\,\mathrm{m}$.

At this distance from the sphere in the wake, a separated laminar shear layer is expected to be found. Vortex pairs are expected to start appearing after transition, farther than $x/D = 1$. The vector field shown in Figure 5.25 does not indicate the presence of wake structures with rotation. Therefore, it is possible that the vorticity presented here is mainly due to shear.

Wake development

The time development of the wake of the sphere is depicted in Figure 5.26. The wake is plotted at three different distances from the back of the sphere: $x = 0.05\,\mathrm{m}$, $x = 0.1\,\mathrm{m}$ and $x = 0.25\,\mathrm{m}$. The in-plane velocity fields appear as vector fields in each image, and all velocity fields are ensemble averaged. The field of view in the image has been cropped so that the wake could be distinguished better.

As expected when the wake is close to the sphere it can be distinguished more clearly and the velocity deficits are more pronounced. For $x = 0.05\,\mathrm{m}$ the wake is roughly the same size as the sphere, with a diameter of 10 cm. One diameter into the wake, the velocity deficit recovery is noticeable, and the minimum velocity is around $u^* = 0.9$, compared to the value of $u^* = 0.8$

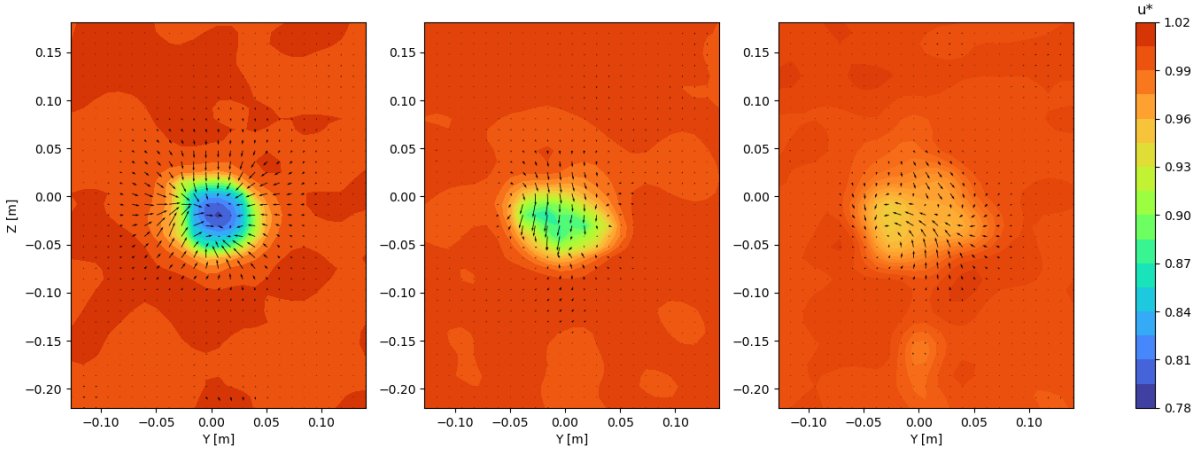

Figure 5.26: Ensemble averaged velocity field with in-plane velocity vectors for the wake of a sphere, at distance of $x = 0.05\,\mathrm{m}$ (left), $x = 0.1\,\mathrm{m}$ (middle) and $x = 0.25\,\mathrm{m}$ (right).

observed at a distance of half a diameter. The shape of the wake is slightly less round, and it is less easy to distinguish. At a distance of $x = 0.25\,\mathrm{m}$, two and a half diameters away from the back of the sphere, the velocity has almost fully recovered. The vector field that shows a clear counter-clockwise vortex on the lower right half of the wake. At a distance of more than two diameters from the wake, this is in line with the vortical structures observed in literature [127] [126]. The size of the wake has also increased at this point. Even though the higher wake velocities make it difficult to distinguish the wake, its diameter at this point is close to 0.15 cm.

5.3.2 Energized mass method

This section is focused on the energized mass method and its application to the case of the sphere. Since the sphere is a fundamental shape, it might give additional information about the method.

The first steps of the processing are shown in Figure 5.27. The preprocessed raw images are shown in the left, and the intensity in each window is shown in the right. The top image corresponds to a distance from the rearmost of the sphere of $x = 10\,\mathrm{cm}$, which is one diameter, and the bottom image shows the wake at a distance of $x = 15\,\mathrm{cm}$.

In this case, the seeding conditions make it possible to distinguish the wake after the sliding minimum has been applied. The intensity of the particles image is higher than in the case of the cyclist (in section 5.2), and the number of particles is also higher. This is reflected also on the images on the right in Figure 5.27, which show the same images after they have been divided into average intensity windows, of size 30 x 30 pixels. In both distances, there are areas in the bottom right corner of low seeding density that might pose a problem.

Some of the following processing steps are shown in Figure 5.28, for the same distances of $x = 0.1\,\mathrm{m}$ and $x = 0.15\,\mathrm{m}$. The images on the left show the result of applying clustering to all points identified as wake after thresholding, and the images on the right show the final wake result superimposed to the preprocessed images. As expected, the low seeding density areas are tagged as wake in the thresholding process and appear as points in the cluster images. However, since they are far away enough from the main wake, the algorithm is able to identify them as noise and exclude them from the wake. Some noise is also present around the main wake.

The final wakes shown in Figure 5.28 (right) demonstrate that the method is able to detect the contours of the darker areas properly. From the first frame to the second, over a distance

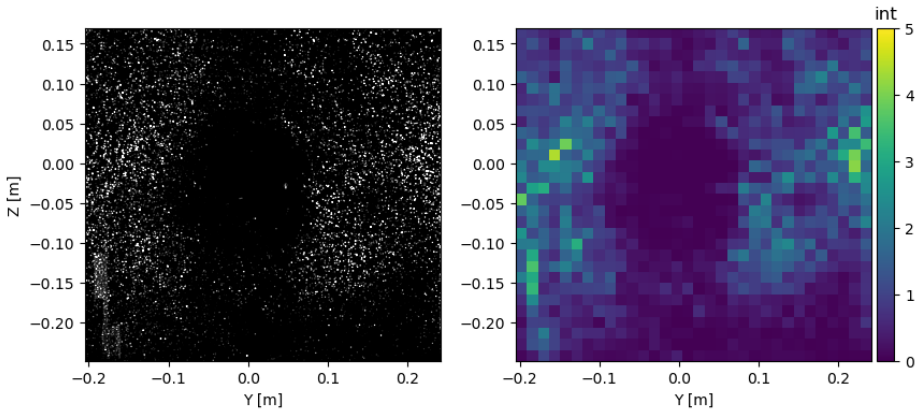

(a) Distance of $x = 0.1\,\mathrm{m}$.

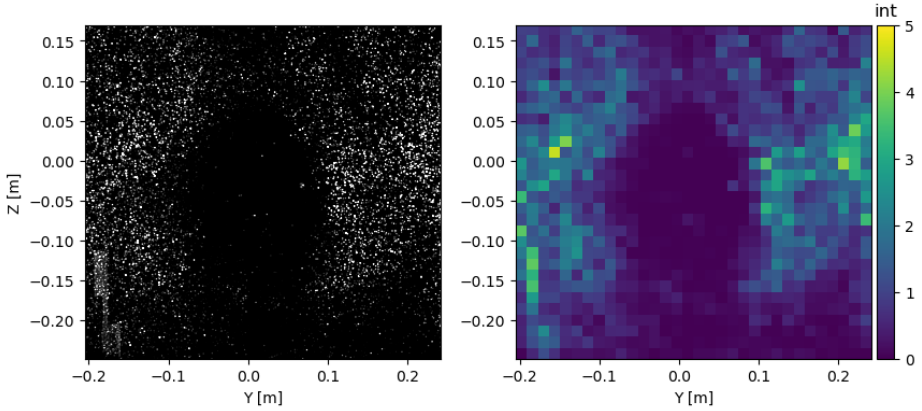

(b) Distance of $x = 0.15\,\mathrm{m}$.

Figure 5.27: Preprocessed image (left) and image after dividing it into intensity average windows, at a distance of (a) $x = 0.1\,\mathrm{m}$ and (b) $x = 0.15\,\mathrm{m}$ from the back of the sphere.

of $x = 0.09\,\mathrm{m}$ (almost one diameter) the wake seems to have expanded mostly vertically. The horizontal diameter does not show significant change.

The velocity contours at the same distances of $x = 0.1\,\mathrm{m}$ and $x = 0.19\,\mathrm{m}$ are shown in Figure 5.29, with the energized mass wake contour superimposed to them, represented by a solid black line. Comparing the two frames, it is noticeable that the energized mass method is capable of detecting the slight elongation of the wake in vertical direction that happens at a larger distance from the sphere. The energized mass wake detected at $x = 0.1\,\mathrm{m}$ is smaller and more round in shape, which makes sense considering that the instantaneous velocity fields show a smaller wake with higher velocity deficit peaks.

Figure 5.29 also shows that the energized mass wake is overestimating the area of the wake. For both frames, the entire regions of low velocity are included in the energized mass wake, but also some surrounding regions of velocity very close to the freestream velocity are added to the detected wake. This leads to an overestimation of the drag area in general, because the entire curve representing the growth of the detected wake area will be shifted upwards. The overestimation of the wake area could indicate that the selected filter length for the sliding minimum filter, N, that is explained in chapter 4 might be too large.

The growth of the energized mass wake area with respect to the distance from the rearmost point of the sphere is plotted in Figure 5.30 as a solid black line. The uncertainty is depicted as a shaded gray area and the reference results are shown with a solid red line. They are taken from the work of Terra et al. on the same data which is presented here [2].

The drag obtained with the method is of $c_D A = 0.027\,\mathrm{m}^2$, which is significantly higher than the drag reported by Terra et al. of $c_D A = 0.006\,\mathrm{m}^2$. Results for the sphere in literature are

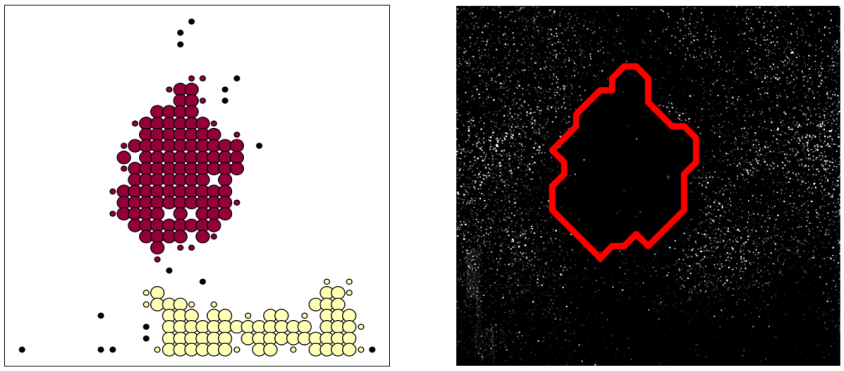

(a) Distance of $x = 0.1\,\mathrm{m}$.

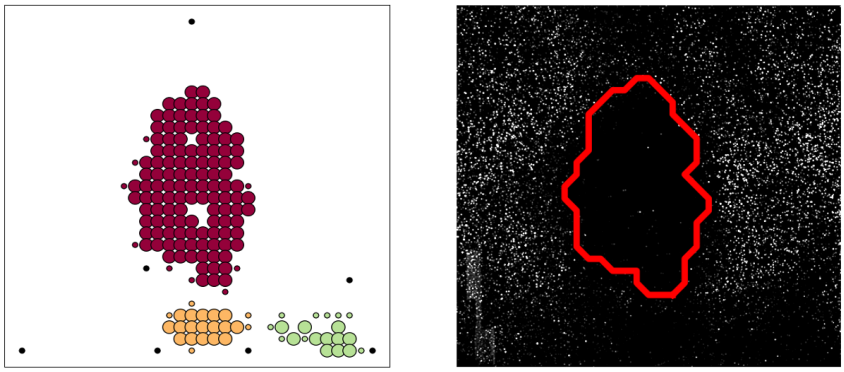

(b) Distance of $x = 0.15\,\mathrm{m}$.

Figure 5.28: Clustering results (left), and energized mass wake (right) for locations of $x = 0.1\,\mathrm{m}$ and $x = 0.15\,\mathrm{m}$ behind the sphere. All dots that have the same color belong to the same cluster, while smaller black dots represent noise.

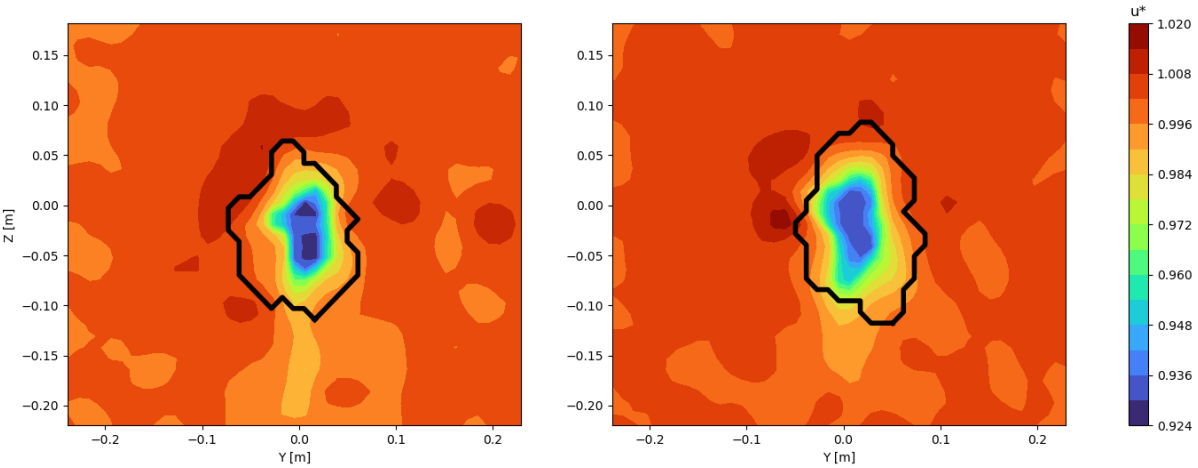

Figure 5.29: Instantaneous streamwise velocity fields and energized mass wake area for locations $x = 0.1\,\mathrm{m}$ and $x = 0.15\,\mathrm{m}$ behind the sphere.

usually indicated in terms of the drag coefficient, since the area of the sphere is easy to obtain. For reference, the c_D obtained with the energized mass method is of $c_D = 1.72$, while Terra et al. obtained $c_D = 0.365$ [2]. The drag coefficient of the sphere varies greatly depending on the Reynolds number, so only results obtained with similar flow conditions will be discussed. In general, other research points to values closer to the reference drag coefficient than the one

obtained with the energized mass method. At the same Reynolds number, LES simulations yielded $c_D = 0.39$ [125] [126], with DES simulations resulting on values closer to $c_D = 0.44$ [125]. In experiments at similar Reynolds numbers, $c_D = 0.39$ [130], $c_D = 0.51$ [124] [131] and $c_D = 0.45$ [132] were measured. The results obtained with the energized mass suggest a drag coefficient more than twice as high as all other results found in literature. Overestimation of the drag has been shown to be an issue for this method, but it is especially critical in this case.

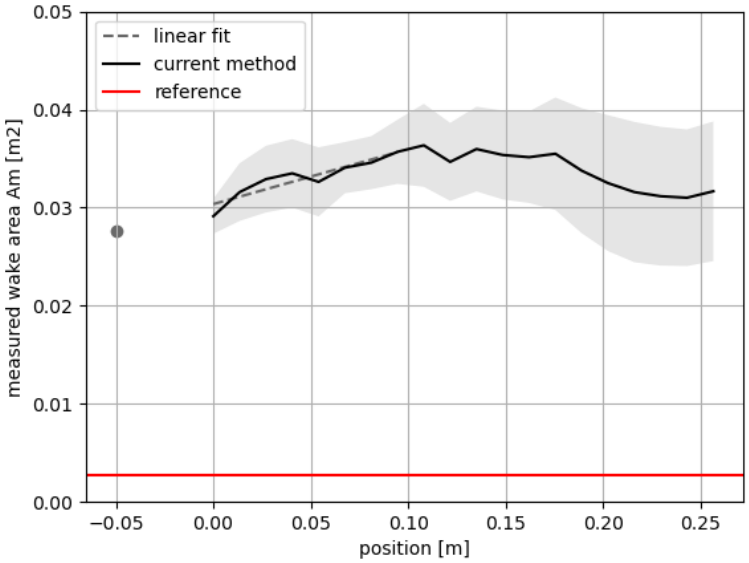

Figure 5.30: Measured wake area change with distance to the back of the sphere (black solid line) and uncertainty of the values (shaded gray). The linear fit (gray dashed line) is extrapolated to the location of the skater (gray dot). Reference $c_D A$ value shown in red.

5.4 Discussion

In this section, the results presented above will be summarized, together with the most important findings. In addition, this section inclused some discussion about the limitations of the energized mass method and possible explanations for them.

Table 5.1 provides a summary of the results that were obtained using the energized mass method for each of the cases presented in the previous sections of this chapter. They are also compared to the reference results, which in the case of the cyclist are obtained form the work of Spoelstra et al. [4] and in the case of the sphere are taken from the results of Terra et al. [2].

Table 5.1: Summary of the drag area results obtained with the energized mass method and comparison with the reference values.

Experimental case	energized mass $c_D A$ [m^2]	reference $c_D A$ [m^2]
Skater (low drag position)	0.39	0.11
Skater (high drag position)	0.66	0.16
Cyclist (time trial position)	0.55	0.25
Cyclist (upright position)	0.46	0.34
Sphere	0.027	0.006

The comparison shows that the energized mass method results have significant errors for every case. The highest error is found in the case of the sphere, where the energized mass method overestimates the drag area by more than three times the reference value. This is a worrying realization because the sphere is the most basic case out of the five that were analyzed. The drag area which is closer to the reference value corresponds to the cyclist in upright position. However, the difference is still high, with an error larger than 30%.

The method in general is capable of determining which objects have a higher drag coefficient, even if the exact value is not correct. For example, the drag area of the low drag position skater was measured to be lower than that of the high drag position skater, and overall the cyclists yielded higher drag values than the skaters. However, a lower value was obtained for the cyclist in time trial position with respect to the cyclist in upright position, when all reviewed literature suggests the contrary.

In order to understand why the results are inaccurate, it is useful to examine the limitations of the method. Firstly, the energized mass method is highly dependant on uniform seeding. Any regions which have lower seeding than others might be confused as part of the wake, especially if these regions happen to occur close to the wake itself. Clustering with DBSCAN has been shown to be a promising solution to discard noise, but a more sophisticated algorithm would likely provide better filtering. It would be especially useful to refine the temporal history part of the clustering, which (as explained in chapter 3) consists on comparing the clustering results at each frame with the previous frame and investigating any major discrepancies. This solution is implemented after the clustering and making it more robust could improve the accuracy of the wake detection. Finally, reflections and background light also have an impact on the result. If they are close to the wake area, they might affect the detected wake area or create holes in it.

All of this makes the energized mass more sensitive to seeding conditions than PIV measurements. As a consequence, in order to achieve the same statistical significance in an experimental campaign, more runs would have to be performed if the energized mass method is going to be used. All the data used in this report was obtained with the idea of applying PIV on it, so the number of used runs was lower than planned. For example, 10 runs were recorded for the skater in high drag position, but only 5 could be used for this method.

The energized mass method relies on the assumption that the fluid in the wake moves at the same speed as the body itself as long as the distance to the body is short. For this reason,

it is expected that the results on streamlined bodies will not be reliable and it should only be applied on bluff bodies. The results highlight another limitation on the type of bodies that can be analysed: in subsection 5.1.2 it was observed that the method does not work well for bodies that are not compact. The clustering algorithm always assumes that there is one single cluster caused by the wake. However, in the case of the high drag skater both arms were stretched out to the sides of the body, and the wake would best be represented by several smaller clusters. The area in between these smaller wake regions is also considered to be wake, which partially explains the overestimation of the drag. This alone cannot explain the discrepancies presented in Table 5.1, since all other bodies, and especially the sphere, are compact and should not be affected by this.

There are some other factors that might explain why the obtained values are much higher than the reference ones. Firstly, the detected wake might be larger than the actual wake. This is not a straightforward issue to solve because there is no clear quantitative definition for the wake, which is usually described as a region where the flow experiences loss of velocity behind an object [40]. Without a tangible definition, it is impossible to validate the wake detection method presented in this work. In addition, there are several steps which are taken in order to identify the wake area which require the selection of a threshold. As shown in chapter 3, the results are sensitive to the choice of threshold.

A possible solution for the threshold selection sensitivity could be to change this step slightly. Instead of using the average intensity of the pixels in a window, the standard deviation in their intensity counts could be used. It is expected that windows inside the wake will have homogeneous, low intensity values, as the wake area in the filtered images is a solid dark region. The windows outside the wake usually contain low intensity pixels, which belong to the background, and high intensity pixels which correspond to the particles that have remained in the image. The high difference in intensity values should cause the windows outside the wake to have significantly higher standard deviation values for the intensity. This could lead to a more robust choice of threshold.

Finally, in all cases the method to extrapolate the wake area at the location of the body was chosen to be a linear regression. It is possible that other types of fits yield better results. For axisymmetric wakes, the flow half width varies proportionally to $x^{\frac{1}{3}}$ when the wake is self-similar [115]. A cubic fit would have a larger slope and therefore the resulting drag area would be smaller. This could be applied to any further work done on this topic.

In conclusion, the energized mass method is a promising first step towards obtaining the drag of a transiting object with the use of a single camera placed behind the object. While the results presented here show a significant overestimation of the drag, the main reasons that cause this are understood. They are related to the implementation and not the method itself, so it is possible that they can fixed in the future with further work.

Chapter 6

Conclusions and recommendations

This chapter is focused on the conclusions that have been reached after the development and testing of the novel energized mass method for on-site drag evaluation. The main conclusions are detailed in section 6.1, while some recommendations for further research in this topic are explained in section 6.2.

6.1 Conclusions

The aim of this work was to develop and test an alternative experimental method to measure the drag of a transiting object. This new method is based on the concept of the energized mass and its only input is raw images similar to those used in PIV. For this purpose only one camera is needed, and no velocity fields need to be computed.

The motivation behind this objective is to be able to measure the drag of transiting objects on-site. The drag coefficient is one of the main aerodynamic characteristics of any object. In particular, for sports such as cycling or speed skater it is a key parameter that can highly influence the outcome of a competitive event. Usually it is measured with simulations or wind tunnel experiments, which are limited to models of the athletes. On-site measurements provide a unique opportunity to investigate the flow field in realistic conditions.

The energized mass method only uses information about the wake growth of said object. The most challenging step is to identify the wake properly. This is done using a sliding minimum filter on the raw images, which acts similarly to a velocity threshold. Several steps are added later. These include dividing each image into windows where the intensity values of the pixels are averaged, and applying a threshold to determine whether each window is part of the wake or the freestream. In order to reduce noise, the DBSCAN clustering algorithm [96] is used to group the wake windows into clusters. The wake is then defined as the largest cluster, and any holes in it are filled in.

The method was tested in three different objects (a sphere, a cyclist and a skater), yielding five experimental cases in total. The sphere and the cyclist data were taken from the experimental campaigns carried out by Terra et al. [2] and Spoelstra et al. [4]. The skater data was obtained in the skating ring of Thialf in February 2021. Two different positions were tested for the cyclist (upright and time trial), as well as two different positions for the skater (high drag and low drag).

In all cases, the images were captured with a PIV set up so that the velocity fields could be obtained and the drag area could be calculated via the Ring of Fire method. The objects moved at a constant velocity through the laser sheet, and the tracer particles used in all cases were Helium Filled Soap Bubbles. The cyclist and skater experimental campaign were done with a stereo-PIV set up, while the sphere was captured with tomo-PIV set up.

The results show that while it is possible to identify the wake, the obtained drag area is not very accurate. The obtained drag area results were compared to literature, results reported by Terra et al. [2] and Spoelstra et al. [4] and the drag calculated with the momentum balance method. In all cases, the energized mass method significantly over estimated the drag area. The most

extreme example of this was the sphere, where the energized mass drag area was more than three times higher the average reported value in literature. However, the energized mass method was able to identify correctly the higher drag objects, even if the differences were measured to be larger than expected. Even if the drag value cannot be obtained reliably, the energized mass method may still be used to compare two objects and understand which has a more desirable aerodynamic performance.

Regarding the wake identification, the method presented here started with the preprocessing to reduce the background intensity and apply the sliding minimum filter. It assigns to each pixel the minimum value of intensity it has had in the selected range of images. In this way, it eliminates from the resulting images any particles that have had enough displacement. The wake could be identified as the darker area left after the faster moving particles were removed. Several steps were added later in order to reduce the noise, including the division of the image into average intensity windows, applying an intensity threshold and the removal of windows that are not part of the wake using the DBSCAN clustering algorithms.

The wake areas obtained with this method were compared to the wake velocity fields that resulted from PIV, showing that the wake was identified satisfactorily. In most cases, however, the identified wake seemed to be larger than the fluid regions with velocity deficit larger than 37%. An important lesson learnt was that the wake of the object needs to be compact. In the case of the high drag skater, which is presented in section 5.1, the wake based on velocity field consisted of different small regions corresponding to the body and the two stretched out arms. Because of the clustering approach, the current method is not able to identify more than one wake region. Therefore, the wake of the arms was grouped together with the wake of the body into a larger identified wake. This increases the output drag area of the skater, which is not desirable.

6.2 Recommendations

There are some possible changes that could help improve the results in future research. They will be explained here, together with recommendations for the next steps in developing and enhancing the energized mass method.

The methodology itself could be revisited and some changes could be tested. Firstly, the backpropagation of the measured wake area could be improved. Instead of using a linear fit, assuming an expansion proportional to $x^{\frac{1}{3}}$ might yield better results based on the known development of axisymmetric wakes [115].

In addition, the method for the wake identification could be slightly modified. The first step after the pre-processing is to divide the image into windows where the intensity of the pixels in each window is averaged. An intensity threshold is then applied to classify each window as wake or freestream flow. This is done because on the preprocessed images it is not possible to determine if a pixel with low intensity is part of the wake or is in between particle images on the freestream region. While the division into windows is necessary, looking at the standard deviation in intensity instead of the average value might work better. In windows inside the wake, the standard deviation should be low because most of the pixels will have similarly low intensity values and it is more homogeneous. In contrast, in freestream windows the standard deviation is expected to be higher due to the greater difference in intensity counts between particle images and background pixels.

In the future it is recommended to apply this method to bluff, compact bodies only. All derivations shown in chapter 3 assume that the object is bluff, and in section 5.1 it was concluded that an important limitation to the method is that it cannot be used to identify the

wake of a non-compact object. The reason for this was the choice of clustering algorithm, which was not able to identify the stretched out arms as part of the same cluster as the body. Regarding this, it might be interesting to try to use a different clustering algorithms and compare the results. It would be particularly helpful to choose one that might be able to take into consideration the clustering results of previous frames, since in this work it was a feature added after clustering.

Further experimental campaigns would help understand how the robustness of the method. In particular, a fundamental shape such as the flat plate could be enlightening, since its was has been studied extensively and it would be possible to find literature to compare and validate the results. Additional measurements would also bring the opportunity to test a set up with a single camera placed parallel to the laser sheet. This would prove definitely that the main objective of the work is satisfied. Finally, it would be interesting to examine how much the quality of the results can be improved when the campaign is designed with special care to reduce any background light. Background light reduction is also important for tomo- and stereo-PIV, so some measures were already taken in the campaigns presented here. However, the energized method has been observed to be more sensitive to background light than PIV, so more drastic measures could be tested.

Bibliography

[1] J. N. Galler and D. E. Rival. "Inverse Ttechnique for Lagrangian, Non-Stokesian Tracer article Correction". en. In: *13th International Symposium on Particle Image Velocimetry - ISPIV 2019*. Munich, Germany, July 2019.

[2] W. Terra et al. "Drag resolution of a PIV wake rake for transiting models". en. In: *Experiments in Fluids* 59.7 (2018), p. 120. ISSN: 0723-4864, 1432-1114. DOI: 10.1007/s00348-018-2570-8.

[3] W. Terra, A. Sciacchitano, and F. Scarano. "Aerodynamic drag of a transiting sphere by large-scale tomographic-PIV". en. In: *Experiments in Fluids* 58.7 (2017), p. 83. ISSN: 0723-4864, 1432-1114. DOI: 10.1007/s00348-017-2331-0.

[4] A. Spoelstra et al. "On-site cycling drag analysis with the Ring of Fire". en. In: *Experiments in Fluids* 60.6 (2019), p. 90. ISSN: 0723-4864, 1432-1114. DOI: 10.1007/s00348-019-2737-y.

[5] D. E. Rival and B. W. van Oudheusden. "Load-Estimation Techniques for Unsteady Incompressible Flows". en. In: *Experiments in Fluids* 58.3 (2017), p. 20. ISSN: 0723-4864, 1432-1114. DOI: 10.1007/s00348-017-2304-3.

[6] B. W. van Oudheusden, F. Scarano, and E. W. F. Casimiri. "Non-Intrusive Load Characterization of an Airfoil using PIV". en. In: *Experiments in Fluids* 40.6 (2006), pp. 988–992. ISSN: 0723-4864, 1432-1114. DOI: 10.1007/s00348-006-0149-2.

[7] L. David, T. Jardin, and A. Farcy. "On the Non-Intrusive Evaluation of Fluid Forces with the Momentum Equation Approach". en. In: *Measurement Science and Technology* 20.9 (2009), p. 095401. ISSN: 0957-0233, 1361-6501. DOI: 10.1088/0957-0233/20/9/095401.

[8] D. F. Kurtulus, F. Scarano, and L. David. "Unsteady Aerodynamic Forces Estimation on a Square Cylinder by TR-PIV". en. In: *Experiments in Fluids* 42.2 (2007), pp. 185–196. ISSN: 0723-4864, 1432-1114. DOI: 10.1007/s00348-006-0228-4.

[9] J. C. Martin et al. "Validation of a Mathematical Model for Road Cycling Power". In: *Journal of Applied Biomechanics* 14.3 (1998), pp. 276–291. ISSN: 1065-8483, 1543-2688. DOI: 10.1123/jab.14.3.276.

[10] The Tokio Organising Committee of the Olympic and Paralympic Games. *Cycling Track: Results Book*. Aug. 2021.

[11] ISU. *ISU World Speed Skating Championships - Result Men 500m*. Feb. 2021. URL: https://live.isuresults.eu/events/2021_NED_0005/schedule.

[12] ISU. *ISU World Speed Skating Championships - Result Men 10000m*. Feb. 2021. URL: https://live.isuresults.eu/events/2021_NED_0005/schedule.

[13] Union Cycliste Internationale. *UCI Cycling Regulations: Part 1 General Organisation of Cycling as a Sport*. Mar. 2022. URL: https://www.uci.org.

[14] L. W. Brownlie and C. R. Kyle. "Evidence that Skin Suits Affect Long Track Speed Skating Performance". en. In: *Procedia Engineering* 34 (2012), pp. 26–31. ISSN: 18777058. DOI: 10.1016/j.proeng.2012.04.006.

[15] G. H. Kuper and E. Sterken. "Do Skin Suits Increase Average Skating Speed?" en. In: (2008), p. 40.

[16] L. Brownlie et al. “Streamlining the time trial apparel of cyclists: The Nike swift spin project”. en. In: *Sports Technology* 2.1-2 (Jan. 2009), pp. 53–60. ISSN: 1934-6182, 1934-6190. DOI: 10.1080/19346182.2009.9648499.

[17] F. Alam et al. “Aerodynamics of Ribbed Bicycle Racing Helmets”. en. In: *Procedia Engineering* 72 (2014), pp. 691–696. ISSN: 18777058. DOI: 10.1016/j.proeng.2014.06.117.

[18] R. A. Lukes, S. B. Chin, and S. J. Haake. “The Understanding and Development of Cycling Aerodynamics”. en. In: *Sports Engineering* 8.2 (2005), pp. 59–74. ISSN: 1369-7072, 1460-2687. DOI: 10.1007/BF02844004.

[19] F. Alam et al. “An experimental study of thermal comfort and aerodynamic efficiency of recreational and racing bicycle helmets”. en. In: *Procedia Engineering* 2.2 (June 2010), pp. 2413–2418. ISSN: 18777058. DOI: 10.1016/j.proeng.2010.04.008.

[20] A. Spoelstra et al. “Uncertainty assessment of the Ring of Fire concept for on-site aerodynamic drag evaluation”. In: *Measurement Science and Technology* 32 (2021), p. 044004. DOI: 1361-6501/21/044004+14$33.00.

[21] R. J. Adrian. “Particle-Imaging Techniques for Experimental Fluid Mechanics”. en. In: *Annual Review of Fluid Mechanics* 23 (1991), pp. 261 –304. DOI: 0066-4189/91/0115-0261$02.00.

[22] C. E. Willert and M. Gharib. “Digital Particle Image Velocimetry”. en. In: *Experiments in Fluids* 10 (1991), pp. 181 –193. DOI: https://doi.org/10.1007/BF00190388.

[23] M. Raffel et al. *Particle Image Velocimetry: A Practical Guide*. en. 3rd ed. 2018. Cham: Springer International Publishing : Imprint: Springer, 2018. ISBN: 978-3-319-68852-7. DOI: 10.1007/978-3-319-68852-7.

[24] C. Tropea, A. L. Yarin, and J. F. Foss, eds. *Springer handbook of experimental fluid mechanics*. en. Berlin: Springer, 2007. ISBN: 978-3-540-25141-5.

[25] J. Westerweel. “Fundamentals of Digital Particle Image Velocimetry”. en. In: *Measurement Science and Technology* 8.12 (1997), pp. 1379–1392. ISSN: 0957-0233, 1361-6501. DOI: 10.1088/0957-0233/8/12/002.

[26] A. Melling. “Tracer Particles and Seeding for Particle Image Velocimetry”. en. In: *Measurement Science and Technology* 8.12 (1997), pp. 1406–1416. ISSN: 0957-0233, 1361-6501. DOI: 10.1088/0957-0233/8/12/005.

[27] D. E. Faleiros et al. “Generation and Control of Helium-Filled Soap Bubbles for PIV”. en. In: *Experiments in Fluids* 60.3 (2019), p. 40. ISSN: 0723-4864, 1432-1114. DOI: 10.1007/s00348-019-2687-4.

[28] G. C. A. Caridi et al. “HFSB-Seeding for Large-Scale Tomographic PIV in Wind Tunnels”. en. In: *Experiments in Fluids* 57.12 (2016), p. 190. ISSN: 0723-4864, 1432-1114. DOI: 10.1007/s00348-016-2277-7.

[29] J. Bosbach, M. Kühn, and C. Wagner. “Large Scale Particle Image Velocimetry with Helium Filled Soap Bubbles”. en. In: *Experiments in Fluids* 46.3 (2009), pp. 539–547. ISSN: 0723-4864, 1432-1114. DOI: 10.1007/s00348-008-0579-0.

[30] F. Scarano et al. “On the Use of Helium-Filled Soap Bubbles for Large-Scale Tomographic PIV in Wind Tunnel Experiments”. en. In: *Experiments in Fluids* 56.2 (2015), p. 42. ISSN: 0723-4864, 1432-1114. DOI: 10.1007/s00348-015-1909-7.

[31] C. Jux et al. “Robotic Volumetric PIV of a Full-Scale Cyclist”. en. In: *Experiments in Fluids* 59.4 (2018), p. 74. ISSN: 0723-4864, 1432-1114. DOI: 10.1007/s00348-018-2524-1.

[32] I. Grant. “Particle Image Velocimetry: A Review”. en. In: *Proceedings of the Institution of Mechanical Engineers, Part C: Journal of Mechanical Engineering Science* 211.1 (1997), pp. 55–76. ISSN: 0954-4062, 2041-2983. DOI: 10.1243/0954406971521665.

[33] A. K. Prasad and R. J. Adrian. "Stereoscopic Particle Image Velocimetry Applied to Liquid Flows". en. In: *Experiments in Fluids* 15.1 (1993), pp. 49–60. ISSN: 0723-4864, 1432-1114. DOI: 10.1007/BF00195595.

[34] G. E. Elsinga et al. "Tomographic Particle Image Velocimetry". en. In: *Experiments in Fluids* 41.6 (2006), pp. 933–947. ISSN: 0723-4864, 1432-1114. DOI: 10.1007/s00348-006-0212-z.

[35] F. Scarano. "Tomographic PIV: Principles and Practice". en. In: *Measurement Science and Technology* 24.1 (2013), p. 012001. ISSN: 0957-0233, 1361-6501. DOI: 10.1088/0957-0233/24/1/012001.

[36] "Photogrammetric Techniques in Multi-Camera Tomographic PIV". en. In: *8TH International Symposium on Particle Image Velocimetry*. Ed. by H. G. Maas and P. Westfeld. Vol. 106. Notes on Numerical Fluid Mechanics and Multidisciplinary Design. Melbourne, Australia, 2009. DOI: 10.1007/978-3-642-01106-1.

[37] C. Ortiz-Dueñas, J. Kim, and E. K. Longmire. "Investigation of Liquid–Liquid Drop Coalescence using Tomographic PIV". en. In: *Experiments in Fluids* 49.1 (2010), pp. 111–129. ISSN: 0723-4864, 1432-1114. DOI: 10.1007/s00348-009-0810-7.

[38] R. Hain, C. J. Kähler, and D. Michaelis. "Tomographic and Time Resolved PIV Measurements on a Finite Cylinder Mounted on a Flat Plate". en. In: *Experiments in Fluids* 45.4 (2008), pp. 715–724. ISSN: 0723-4864, 1432-1114. DOI: 10.1007/s00348-008-0553-x.

[39] G. E. Elsinga and I. Marusic. "Evolution and Lifetimes of Flow Topology in a Turbulent Boundary Layer". en. In: *Physics of Fluids* 22.1 (2010), p. 015102. ISSN: 1070-6631, 1089-7666. DOI: 10.1063/1.3291070.

[40] J. D. Anderson Jr. *Fundamentals of Aerodynamics*. en. 5th ed. McGraw-Hill series in aeronautical and aerospace engineering. New York, NY: McGraw Hill Education, 2011. ISBN: 978-0-07-339810-5.

[41] A. Mohebbian and D. E. Rival. "Assessment of the Derivative-Moment Transformation Method for Unsteady-Load Estimation". en. In: *Experiments in Fluids* 53.2 (2012), pp. 319–330. ISSN: 0723-4864, 1432-1114. DOI: 10.1007/s00348-012-1290-8.

[42] B W van Oudheusden. "PIV-based Pressure Measurement". en. In: *Measurement Science and Technology* 24.3 (2013), p. 032001. ISSN: 0957-0233, 1361-6501. DOI: 10.1088/0957-0233/24/3/032001.

[43] R. Gurka et al. "Computation of Pressure Distribution Using PIV Velocity Data". en. In: *3rd International Symposium on Particle Image Velocimetry*. 1999, p. 7.

[44] N. Fujisawa, S. Tanahashi, and K. Srinivas. "Evaluation of Pressure Feld and Fluid Forces on a Circular Cylinder with and without Rotational Oscillation using Velocity Data from PIV Measurement". en. In: *Measurement Science and Technology* 16 (2005), pp. 989 –996. DOI: doi:10.1088/0957-0233/16/4/011.

[45] A Sciacchitano. "Uncertainty quantification in particle image velocimetry". en. In: *Measurement Science and Technology* 30.9 (2019), p. 092001. ISSN: 0957-0233, 1361-6501. DOI: 10.1088/1361-6501/ab1db8.

[46] S. Bhattacharya, J. J. Charonko, and P. P. Vlachos. "Stereo-Particle Image Velocimetry Uncertainty Quantification". en. In: *Measurement Science and Technology* 28.1 (2017), p. 015301. ISSN: 0957-0233, 1361-6501. DOI: 10.1088/1361-6501/28/1/015301.

[47] A. Sciacchitano, B. Wieneke, and F. Scarano. "PIV uncertainty quantification by image matching". en. In: *Measurement Science and Technology* 24.4 (2013), p. 045302. ISSN: 0957-0233, 1361-6501. DOI: 10.1088/0957-0233/24/4/045302.

[48] H. Lamb. *Hydrodynamics*. Cambridge Univ. Press, 1895.

[49] K. Wendel. *Hydrodynamic Masses and Hydrodynamic Moments of Inertia*. Tech. rep. Washington D. C., USA: NAVY DTMB, July 1956.

[50] C. E. Brennen. *A Review of Added Mass and Fluid Inertial Forces*. Tech. rep. CR 82.010. Naval Civil Engineering Laboratory, 1982.

[51] E. H. Kennard. *Irrotational Flow of Frictionless Fluids, Mostly of Invariable Density*. Tech. rep. Fort Belvoir, VA: Defense Technical Information Center, 1967. DOI: 10.21236/AD0653463.

[52] K. T. Patton. "An Experimental Determination of Hydrodynamic Masses and Mechanical Impedances". en. PhD thesis. University of Rhode Island, 1965.

[53] G. K. Batchelor. *An Introduction to Fluid Dynamics*. en. 1. Cambridge mathematical ed., 14. print. Cambridge mathematical library. OCLC: 838184093. Cambridge: Cambridge Univ. Press, 1967. ISBN: 978-0-521-66396-0.

[54] T. L. Daniel. "Unsteady Aspects of Aquatic Locomotion". en. In: *American Zoologist* 24.1 (1984), pp. 121–134.

[55] Y. T. Yu. "Virtual Masses and Moments of Inertia of Disks and Cylinders in Various Liquids". en. In: *Journal of Applied Physics* 13.1 (1942), pp. 66–69. ISSN: 0021-8979, 1089-7550. DOI: 10.1063/1.1714805.

[56] Y. T. Yu. "Virtual Masses of Rectangular Plates and Parallelepipeds in Water". en. In: *Journal of Applied Physics* 16.11 (1945), pp. 724–729. ISSN: 0021-8979, 1089-7550. DOI: 10.1063/1.1707527.

[57] E. J. Grift et al. "Drag Force on an Accelerating Submerged Plate". en. In: *Journal of Fluid Mechanics* 866 (2019), pp. 369–398. ISSN: 0022-1120, 1469-7645. DOI: 10.1017/jfm.2019.102.

[58] J. N. Fernando, G. D. Weymouth, and D. E. Rival. "On the Limits of Added-Mass Theory in Separated Flows and with Varying Initial Conditions". en. In: *Journal of Fluids and Structures* 93 (2020), p. 102835. ISSN: 08899746. DOI: 10.1016/j.jfluidstructs.2019.102835.

[59] C. Darwin. "Note on Hydrodynamics". en. In: *Mathematical Proceedings of the Cambridge Philosophical Society* 49.2 (1953), pp. 342–354. ISSN: 0305-0041, 1469-8064. DOI: 10.1017/S0305004100028449.

[60] I. Eames, S. E. Belcher, and J. C. R. Hunt. "Drift, partial drift and Darwin's proposition". en. In: *Journal of Fluid Mechanics* 275 (1994), pp. 201–223. ISSN: 0022-1120, 1469-7645. DOI: 10.1017/S0022112094002338.

[61] M. J. Lighthill. "Drift". en. In: *Journal of Fluid Mechanics* 1.01 (1956), p. 31. ISSN: 0022-1120, 1469-7645. DOI: 10.1017/S0022112056000032.

[62] C. S. Yih. "New Derivations of Darwin's Theorem". en. In: *Journal of Fluid Mechanics* 152 (1985), pp. 163–172. ISSN: 0022-1120, 1469-7645. DOI: 10.1017/S0022112085000623.

[63] T. B. Benjamin. "Note on Added Mass and Drift". en. In: *Journal of Fluid Mechanics* 169 (1986), pp. 251 –256. ISSN: 0022-1120, 1469-7645. DOI: 10.1017/S0022112086000617.

[64] J. W. M. Bush and I. Eames. "Fluid Displacement by High Reynolds Number Bubble Motion in a Thin Gap". en. In: *International Journal of Multiphase Flow* 24.3 (1998), pp. 411–430. ISSN: 03019322. DOI: 10.1016/S0301-9322(97)00068-2.

[65] J. O. Dabiri. "On the Estimation of Swimming and Flying Forces from Wake Measurements". en. In: *Journal of Experimental Biology* 208.18 (2005), pp. 3519–3532. ISSN: 0022-0949, 1477-9145. DOI: 10.1242/jeb.01813.

[66] P. G. Saffman. *Vortex Dynamics*. Cambridge monographs on mechanics and applied mathematics. Cambridge University Press, 1995. ISBN: 0-521-47739-5.

[67] W. R. Graham, C. W. Pitt Ford, and H. Babinsky. “An Impulse-Based Approach to Estimating Forces in Unsteady Flow”. en. In: *Journal of Fluid Mechanics* 815 (2017), pp. 60–76. ISSN: 0022-1120, 1469-7645. DOI: 10.1017/jfm.2017.45.

[68] Y. S. Baik et al. “Unsteady force generation and vortex dynamics of pitching and plunging aerofoils”. en. In: *Journal of Fluid Mechanics* 709 (2012), pp. 37–68. ISSN: 0022-1120, 1469-7645. DOI: 10.1017/jfm.2012.318.

[69] S. J. Corkery, H. Babinsky, and W. R. Graham. “Quantification of Added-Mass Effects using Particle Image Velocimetry Data for a Translating and Rotating Flat Plate”. en. In: *Journal of Fluid Mechanics* 870 (2019), pp. 492–518. ISSN: 0022-1120, 1469-7645. DOI: 10.1017/jfm.2019.231.

[70] A. Leonard and A. Roshko. “Aspects of Flow-Induced Vibration”. en. In: *Journal of Fluids and Structures* 15.3-4 (2001), pp. 415–425. ISSN: 08899746. DOI: 10.1006/jfls.2000.0360.

[71] J. D. Eldredge. “A Reconciliation of Viscous and Inviscid Approaches to Computing Locomotion of Deforming Bodies”. en. In: *Experimental Mechanics* 50.9 (2010), pp. 1349–1353. ISSN: 0014-4851, 1741-2765. DOI: 10.1007/s11340-009-9275-0.

[72] J. C. Wu. “Theory for Aerodynamic Force and Moment in Viscous Flows”. en. In: *AIAA Journal* 19.4 (1981), pp. 432–441. ISSN: 0001-1452, 1533-385X. DOI: 10.2514/3.50966.

[73] C. J. McPhaden and D. E. Rival. “Unsteady Force Estimation using a Lagrangian Drift-Volume Approach”. en. In: *Experiments in Fluids* 59.4 (2018), p. 64. ISSN: 0723-4864, 1432-1114. DOI: 10.1007/s00348-018-2515-2.

[74] J. N. Galler, G. D. Weymouth, and D. E. Rival. “On the Concept of Energized Mass: A Robust Framework for Low-Order Force Modeling in Flow Past Accelerating Bodies”. en. In: *Physics of Fluids* 33.5 (2021), p. 057103. ISSN: 1070-6631, 1089-7666. DOI: 10.1063/5.0040061.

[75] J. N. Galler, D. E. Rival, and G. D. Weymouth. “Application of the Energized-Mass Concept to Describe Gust-Body Interactions”. en. In: *AIAA Scitech 2020 Forum*. Orlando, FL: American Institute of Aeronautics and Astronautics, 2020. ISBN: 978-1-62410-595-1. DOI: 10.2514/6.2020-1055.

[76] F. M. White. *Viscous Fluid Flow*. 3rd ed. McGraw-Hill series in mechanical engineering. New York, NY: McGraw Hill Education, 2006. ISBN: 0-07-240231-8.

[77] D. Bastine et al. “Towards a Simplified DynamicWake Model Using POD Analysis”. en. In: *Energies* 8.2 (2015), pp. 895–920. ISSN: 1996-1073. DOI: 10.3390/en8020895.

[78] A. Jiménez, A. Crespo, and E. Migoya. “Application of a LES Technique to Characterize the Wake Deflection of a Wind Turbine in Yaw”. en. In: *Wind Energy* 13.6 (2009), pp. 559–572. ISSN: 10954244. DOI: 10.1002/we.380.

[79] G. España et al. “Spatial Study of the Wake Meandering using Modelled Wind Turbines in a Wind Tunnel: Spatial Study of the Wake Meandering”. en. In: *Wind Energy* 14.7 (2011), pp. 923–937. ISSN: 10954244. DOI: 10.1002/we.515.

[80] M. Holzner et al. “Generalized Detection of a Turbulent Front Generated by an Oscillating Grid”. en. In: *Experiments in Fluids* 41.5 (2006), pp. 711–719. ISSN: 0723-4864, 1432-1114. DOI: 10.1007/s00348-006-0193-y.

[81] D. K. Bisset, J. C. R. Hunt, and M. M. Rogers. “The Turbulent/Non-Turbulent Interface Bounding a Far Wake”. en. In: *Journal of Fluid Mechanics* 451 (2002), pp. 383–410. ISSN: 0022-1120, 1469-7645. DOI: 10.1017/S0022112001006759.

[82] J. Mathew and A. J. Basu. “Some Characteristics of Entrainment at a Cylindrical Turbulence Boundary”. en. In: *Physics of Fluids* 14.7 (2002), p. 2065. ISSN: 10706631. DOI: 10.1063/1.1480831.

[83] R. R. Prasad and K. R. Sreenivasan. “Scalar interfaces in digital images of turbulent flows”. en. In: *Experiments in Fluids* 7.4 (1989), pp. 259–264. ISSN: 0723-4864, 1432-1114. DOI: 10.1007/BF00198005.

[84] J. Westerweel et al. “Mechanics of the Turbulent-Nonturbulent Interface of a Jet”. en. In: *Physical Review Letters* 95.17 (2005), p. 174501. ISSN: 0031-9007, 1079-7114. DOI: 10.1103/PhysRevLett.95.174501.

[85] J. Westerweel et al. “The Turbulent/Non-Turbulent Interface at the Outer Boundary of a Self-Similar Turbulent Jet”. en. In: *Experiments in Fluids* 33.6 (2002), pp. 873–878. ISSN: 0723-4864, 1432-1114. DOI: 10.1007/s00348-002-0489-5.

[86] Dao Lam and D. C. Wunsch. “Clustering”. en. In: *Academic Press Library in Signal Processing*. Vol. 1. Elsevier, 2014, pp. 1115–1149. ISBN: 978-0-12-396502-8. DOI: 10.1016/B978-0-12-396502-8.00020-6.

[87] C. H. Chen. “A hybrid intelligent model of analyzing clinical breast cancer data using clustering techniques with feature selection”. en. In: *Applied Soft Computing* 20 (July 2014), pp. 4–14. ISSN: 15684946. DOI: 10.1016/j.asoc.2013.10.024.

[88] A. Wartelle et al. “Clustering of a Health Dataset Using Diagnosis Co-Occurrences”. en. In: *Applied Sciences* 11.5 (Mar. 2021), p. 2373. ISSN: 2076-3417. DOI: 10.3390/app11052373.

[89] A. Saxena et al. “A review of clustering techniques and developments”. en. In: *Neurocomputing* 267 (Dec. 2017), pp. 664–681. ISSN: 09252312. DOI: 10.1016/j.neucom.2017.06.053.

[90] O. Maimon and L. Rokach, eds. *Data Mining and Knowledge Discovery Handbook*. en. Boston, MA: Springer US, 2010. ISBN: 978-0-387-09822-7 978-0-387-09823-4. DOI: 10.1007/978-0-387-09823-4.

[91] G. Karypis and V. Kumar. “CHAMELEON: A Hierarchical Clustering Algorithm Using Dynamic Modeling”. en. In: (1999), p. 22.

[92] S. Guha, R. Rastogi, and K. Shim. “CURE: An Efficient Clustering Algorithm for Large Databases”. en. In: *Information Systems* 26.1 (2001), pp. 35–58. ISSN: 0306-4379. DOI: https://doi.org/10.1016/S0306-4379(01)00008-4..

[93] T. Zhang, R. Ramakrishnan, and M. Livny. “BIRCH: An Efficient Data Cluserting Method for Very Large Databases”. In: *ACM SIGMOD Record* 25.2 (1996), pp. 103–114. DOI: https://doi.org/10.1145/235968.233324.

[94] F. Nielsen. *Introduction to HPC with MPI for Data Science*. en. Undergraduate Topics in Computer Science. Cham: Springer International Publishing, 2016. ISBN: 978-3-319-21902-8 978-3-319-21903-5. DOI: 10.1007/978-3-319-21903-5. URL: http://link.springer.com/10.1007/978-3-319-21903-5 (visited on 05/09/2022).

[95] C. Piech and A. Ng. *K Means*. 2012. URL: https://stanford.edu/~cpiech/cs221/handouts/kmeans.html.

[96] M. Ester, H. P. Kriegel, and X. Xu. “A Density-Based Algorithmfor Discovering Clusters in LargeSpatial Databaseswith Noise”. en. In: *KDD-96 Proceedings* (1996), p. 6.

[97] E. Schubert et al. “DBSCAN Revisited, Revisited: Why and How You Should (Still) Use DBSCAN”. en. In: *ACM Transactions on Database Systems* 42.3 (2017), pp. 1–21. ISSN: 0362-5915, 1557-4644. DOI: 10.1145/3068335.

[98] E. W. Quon, P. Doubrawa, and M. Debnath. “Comparison of Rotor Wake Identification and Characterization Methods for the Analysis of Wake Dynamics and Evolution”. en. In: *Journal of Physics: Conference Series* 1452 (2020), p. 012070. ISSN: 1742-6588, 1742-6596. DOI: 10.1088/1742-6596/1452/1/012070.

[99] C. B. da Silva and R. R. Taveira. "The Thickness of the Turbulent/Non-Tturbulent Interface is Equal to the Radius of the Large Vorticity Structures near the Edge of the Shear Layer". en. In: *Physics of Fluids* 22.12 (2010), p. 121702. ISSN: 1070-6631, 1089-7666. DOI: 10.1063/1.3527548.

[100] C. B. da Silva and J. C. F. Pereira. "Invariants of the Velocity-Gradient, Rate-of-Strain, and Rate-of-Rotation Tensors Across the Turbulent/Non-Turbulent Interface in Jets". en. In: *Physics of Fluids* 20.5 (2008), p. 055101. ISSN: 1070-6631, 1089-7666. DOI: 10.1063/1.2912513.

[101] A. Sciacchitano, P. Bluyssen, and A. Spoelstra. *Airflow Measurements in the Thialf ice rink*. en. Tech. rep. TU Delft, Mar. 2021, p. 29.

[102] N. Barry et al. "Aerodynamic Performance and Riding Posture in Road Cycling and Triathlon". en. In: 229.1 (2015), pp. 28–38. ISSN: 1754-3371, 1754-338X. DOI: 10.1177/1754337114549876.

[103] T. N. Crouch et al. "Riding Against the Wind: a Review of Competition Cycling Aerodynamics". In: *Sports Engineering* 20 (2017), pp. 81 –110. DOI: 10.1007/s12283-017-0234-1.

[104] G. Gibertini and D. Grassi. "Cycling Aerodynamics". In: *Sport Aerodynamics*. Ed. by G. Maier et al. Vol. 506. Series Title: CISM International Centre for Mechanical Sciences. Vienna: Springer Vienna, 2008, pp. 23–47. ISBN: 978-3-211-89296-1 978-3-211-89297-8. DOI: 10.1007/978-3-211-89297-8_3.

[105] F. Grappe et al. "Aerodynamic Drag in Field Cycling with Special Reference to the Obree's Position". en. In: *Ergonomics* 40.12 (1997), pp. 1299–1311. ISSN: 0014-0139, 1366-5847. DOI: 10.1080/001401397187388.

[106] T. Defraeye et al. "Aerodynamic study of different cyclist positions: CFD analysis and full-scale wind-tunnel tests". en. In: *Journal of Biomechanics* 43.7 (May 2010), pp. 1262–1268. ISSN: 00219290. DOI: 10.1016/j.jbiomech.2010.01.025.

[107] A. E. Jeukendrup and J. Martin. "Improving Cycling Performance: How Should We Spend Our Time and Money". en. In: *Sports Medicine* 31.7 (2001), pp. 559–569. ISSN: 0112-1642. DOI: 10.2165/00007256-200131070-00009.

[108] R. J. Adrian and J. Westerweel. *Particle Image Velocimetry*. Cambridge Aerospace Series. Cambridge University Press, Mar. 2011. ISBN: 978-0-521-44008-0.

[109] J. Westerweel and F. Scarano. "Universal outlier detection for PIV data". en. In: *Experiments in Fluids* 39.6 (2005), pp. 1096–1100. ISSN: 0723-4864, 1432-1114. DOI: 10.1007/s00348-005-0016-6.

[110] K. P. Lynch and F. Scarano. "An efficient and accurate approach to MTE-MART for time-resolved tomographic PIV". en. In: *Experiments in Fluids* 56.3 (Mar. 2015), p. 66. ISSN: 0723-4864, 1432-1114. DOI: 10.1007/s00348-015-1934-6.

[111] P. Debraux et al. "Aerodynamic Drag in Cycling: Methods of Assessment". en. In: *Sports Biomechanics* 10.3 (2011), pp. 197–218. ISSN: 1476-3141, 1752-6116. DOI: 10.1080/14763141.2011.592209.

[112] A. D'Auteuil, G. L. Larose, and S. J. Zan. "The Effect of Motion on Wind Tunnel Drag Measurement for Athletes". en. In: *Procedia Engineering* 34 (2012), pp. 62–67. ISSN: 18777058. DOI: 10.1016/j.proeng.2012.04.012.

[113] A. D'Auteuil, G. L. Larose, and S. J. Zan. "Relevance of Similitude Parameters for Drag Reduction in Sport Aerodynamics". en. In: *Procedia Engineering* 2.2 (2010), pp. 2393–2398. ISSN: 18777058. DOI: 10.1016/j.proeng.2010.04.005.

[114] G. J. van Ingen Schenau. "The Influence of Air Friction in Speed Skating". en. In: *Journal of Biomechanics* 15 (1982), pp. 449–458. DOI: 0021-9290/82/060449-10$03.00/0.

[115] S. B. Pope. *Turbulent Flows*. 14th edition. UK: Cambridge University Press, 2016. ISBN: 978-0-521-59886-6.

[116] P. E. Di Prampero et al. "Energy Cost of Speed Skating and Efficiency of Work Against Air Resistance". en. In: *Journal of Applied Physiology* 40.4 (1976), pp. 584–591. ISSN: 8750-7587, 1522-1601. DOI: 10.1152/jappl.1976.40.4.584.

[117] L. de Martino Norante. "Advances and assessment of the Ring of Fire concept for on-site cycling aerodynamics". en. PhD thesis. TU Delft, 2018. URL: http://resolver.tudelft.nl/uuid:2b8874e9-5100-4e76-bae0-c3d1ad74798d.

[118] T. N. Crouch et al. "Flow Topology in the Wake of a Cyclist and its Effect on Aerodynamic Drag". en. In: *Journal of Fluid Mechanics* 748 (2014), pp. 5–35. ISSN: 0022-1120, 1469-7645. DOI: 10.1017/jfm.2013.678.

[119] T. N. Crouch et al. "Dynamic Leg-Motion and its Effect on the Aerodynamic Performance of Cyclists". en. In: *Journal of Fluids and Structures* 65 (2016), pp. 121–137. ISSN: 08899746. DOI: 10.1016/j.jfluidstructs.2016.05.007.

[120] N. Barry et al. "Aerodynamic drag interactions between cyclists in a team pursuit". en. In: *Sports Engineering* 18.2 (June 2015), pp. 93–103. ISSN: 1369-7072, 1460-2687. DOI: 10.1007/s12283-015-0172-8.

[121] S. Padilla et al. "Scientific approach to the 1-h cycling world record: a case study". en. In: *Journal of Applied Physiology* 89.4 (Oct. 2000), pp. 1522–1527. ISSN: 8750-7587, 1522-1601. DOI: 10.1152/jappl.2000.89.4.1522.

[122] H. Chowdhury and F. Alam. "Bicycle aerodynamics: an experimental evaluation methodology". en. In: *Sports Engineering* 15.2 (June 2012), pp. 73–80. ISSN: 1369-7072, 1460-2687. DOI: 10.1007/s12283-012-0090-y.

[123] B. Blocken, Y. Toparlar, and T. Andrianne. "Aerodynamic benefit for a cyclist by a following motorcycle". en. In: *Journal of Wind Engineering and Industrial Aerodynamics* 155 (Aug. 2016), pp. 1–10. ISSN: 01676105. DOI: 10.1016/j.jweia.2016.04.008.

[124] E. Achenbach. "Experiments on the Flow Past Spheres at very High Reynolds Numbers". en. In: *Journal of Fluid Mechanics* 54.3 (1972), pp. 565–575. ISSN: 0022-1120, 1469-7645. DOI: 10.1017/S0022112072000874.

[125] G. S. Constantinescu and K. D. Squires. "LES and DES Investigations of Turbulent Flow over a Sphere at Re = 10,000". en. In: *Flow, Turbulence and Combustion (formerly Applied Scientific Research)* 70.1-4 (2003), pp. 267–298. ISSN: 1386-6184. DOI: 10.1023/B:APPL.0000004937.34078.71.

[126] G. Yun, D. Kim, and H. Choi. "Vortical Structures Behind a Sphere at Subcritical Reynolds Numbers". en. In: *Physics of Fluids* 18.1 (2006), p. 015102. ISSN: 1070-6631, 1089-7666. DOI: 10.1063/1.2166454.

[127] Y. I. Jang and S. J. Lee. "Visualization of turbulent flow around a sphere at subcritical reynolds numbers". en. In: *Journal of Visualization* 10.4 (Dec. 2007), pp. 359–366. ISSN: 1343-8875, 1875-8975. DOI: 10.1007/BF03181894.

[128] I. Rodríguez et al. "Flow dynamics in the turbulent wake of a sphere at sub-critical Reynolds numbers". en. In: *Computers & Fluids* 80 (July 2013), pp. 233–243. ISSN: 00457930. DOI: 10.1016/j.compfluid.2012.03.009.

[129] A. Leder and D. Geropp. "Unsteady Flow Structure in the Wake of the Sphere". en. In: ed. by J. M. Bessem et al. Koningshof, Veldhoven, Netherlands, 1993, pp. 119–126. DOI: 10.1117/12.150495.

[130] D. L. Bacon and E. G. Reid. *The Resistance of Spheres in Wind Tunnels and in Air*. Tech. rep. 185. Washington D. C., USA: National Advisory Comitee for Aeronautics, 1924.

[131] N. Moradian, D. S.-K. Ting, and S. Cheng. “The Effects of Freestream Turbulence on the Drag Coefficient of a Sphere”. en. In: *Experimental Thermal and Fluid Science* 33.3 (2009), pp. 460–471. ISSN: 08941777. DOI: 10.1016/j.expthermflusci.2008.11.001.

[132] T. Maxworthy. “Experiments on the Flow Around a Sphere at High Reynolds Numbers”. en. In: *Journal of Applied Mechanics* 36.3 (1969), pp. 598–607. ISSN: 0021-8936, 1528-9036. DOI: 10.1115/1.3564723.

Chapter A

Test matrix for speed skater experiments

Run	Position	P. soap [bar]	P. He [bar]	P. air [bar]	Temp [°C]	Humidity [%]	Comments
076	Low	3.80	3.7	3.40	10	54	
077	High	3.80	3.9	3.70	11	53	
078	Low	3.80	3.0	3.40	10	54	
079	High	3.80	3.0	3.40	10	54	
080	Low	3.77	3.6	3.60	10	55	Laser sheet issue
081	High	3.79	3.7	3.60	10	55	Laser sheet issue
082	Low	3.76	3.8	3.65	10	55	Laser sheet issue
083	High	3.75	3.7	3.63	10	55	Laser sheet issue
084	Low	3.75	3.7	3.63	10	55	Laser sheet issue
085	High	3.75	3.7	3.38	10	55	
086	Low	3.75	3.8	3.65	10	55	
087	High	3.75	3.8	3.65	10	55	
088	Low	3.60	3.7	2.95	10	55	
089	High	3.75	3.8	3.65	10	56	
090	Low	3.75	3.8	3.65	10	56	
091	Low	3.75	3.8	3.65	10	56	
092	High	3.75	3.8	3.65	10	56	
093	Low	3.75	3.8	3.65	10	56	
094	High	3.75	3.8	3.65	10	56	
095	High	3.75	3.8	3.65	10	56	